MSc. Thesis

Aerodynamic Analysis and Optimisation of Wingtip-Mounted Pusher Propellers

An investigation into the propulsive gains and optimal geometry of small-scale propellers

S. Nootebos

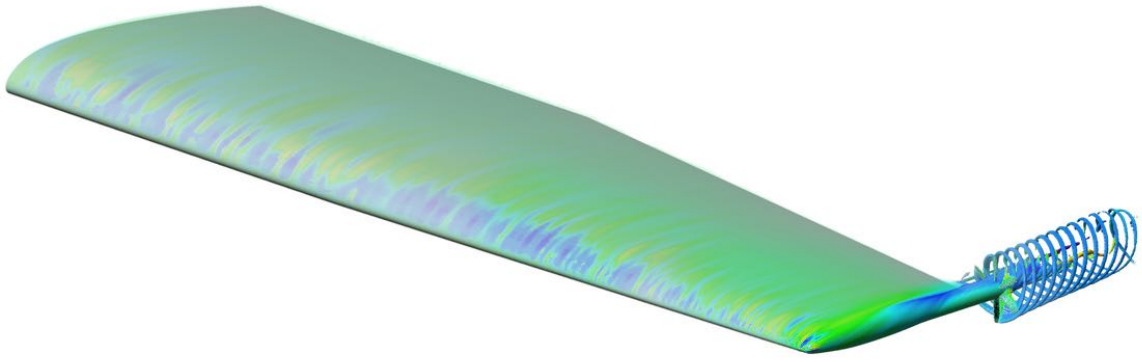

Delft University of Technology | Flight Performance and Propulsion

TU Delft

Aerodynamic analysis and optimisation of wingtip-mounted pusher propellers

An investigation into the propulsive gains and optimal geometry of small-scale propellers

by

S. Nootebos

to obtain the degree of Master of Science
at the Delft University of Technology,
to be defended publicly on Thursday July 26th, 2018 at 2:00 PM.

Student number:	4023293	
Project duration:	February 1st, 2017 – July 26th, 2018	
Thesis committee:	ir. T.C.A. Stokkermans,	TU Delft, supervisor
	Prof. dr. ir. L.L.M. Veldhuis,	TU Delft, supervisor
	Dr. ir. M. Pini,	TU Delft
	Dr. ir. J. Sodja,	TU Delft

An electronic version of this thesis is available at `http://repository.tudelft.nl/`.

TU Delft

Acknowledgements

This thesis work represents the final milestone in completing the MSc. in Aerospace Engineering. It has been a challenging process and without the support of others this would have been impossible. First and foremost I would like to thank my daily supervisor Tom for his great help, insight and lots of patience. Secondly, I would like to thank Leo Veldhuis for the few, but critical and insightful meetings we've had.

Next to my supervisors I owe a big thanks to the guys in room 1.05 for the laughs, help and motivation, it was great to have some fun during work. Last but not least, I'd like to thank my friends and family for their support over the past years. You all kept me motivated and certainly helped me reach this milestone.

S. Nootebos
Delft, July 2018

Abstract

Ever since the late seventies great engineering effort has gone into increasing the fuel efficiency and reduction of the noise profile of aircraft. A concept that has been explored is the wingtip-mounted (pusher) propeller. In all wings energy is lost due to the lift-induced vortex at the wingtip. Wingtip-mounted pusher propellers can recover some of this energy if rotating opposite to the wingtip vortex rotation. The required propeller shaft power and wing induced drag could be reduced. Nevertheless, no aircraft utilise this setup because of aeroelastic problems and one-engine-out requirements. Nowadays this can be resolved by scaling down the propeller and using (distributed) electric propulsion. Recent developments in personal air transport and multi-rotor aircraft have sparked interest in wingtip-mounted propellers. The goal of this research is to obtain quantified insight into the propulsive efficiency gains and optimal geometry of a pusher propeller placed in a wingtip flow field.

In the first part of this research a CFD simulation of the wingtip flow field was implemented and validated with available experimental data. A simple Spalart-Allmaras turbulence model proved to be most suitable and accurate. The flow field of the Tecnam P2006T aircraft was modelled to provide a realistic wingtip flow field to which the propeller would be subjected.

In the second part of this research a lower-order tool called *PROPR* was built and proved to be a fast propeller aerodynamic analysis tool. Validation with experimental data showed a deviation of less than 15% in obtained thrust- and torque coefficients found. *PROPR* was integrated in an optimisation routine for fast optimisation of propeller geometry and operating conditions for non-uniform inflow. Total thrust, torque and their distributions obtained from *PROPR* and an implemented CFD model showed identical trends and were overestimated approximately 5% by *PROPR*.

In the final research part the Tecnam wing with installed propeller was investigated. A wingtip-mounted pusher propeller enables more than 12% increase in propulsive efficiency over the entire propeller thrust regime evaluated. Propeller optimisation was done for a thrust range of $50 < T_{des} < 350$ N, wing induced drag was 240 N. Relative reductions in power requirement were constant for the thrust regime. Absolute power decrease did not decrease with increasing design thrust. No airfoil optimisation was performed to enable fast and stable optimization. From optimisation of a fictitious propeller with constant airfoil geometry it was concluded that the airfoil geometries are a limiting factor in fully capturing the benefits of the wingtip flow field. In optimised (installed) propeller geometry blade loadings shift towards the blade root. A smaller chord length and lower RPM are preferred given the used baseline propeller geometry.

A CFD simulation in which the propeller was represented as an actuator disk was constructed. The upstream effect of an installed propeller was negligible. Thus, the incoming flow field was independent of propeller thrust within the considered thrust range. With this the implemented methodology was proven to be valid. Also, the overall power reduction of the combined setup is thus equal to the power reduction of the propeller. Comparison with transient CFD simulations of the wing with installed propeller showed great correspondence with results from *PROPR*.

In further research it is recommended to include optimisation of (root section) airfoil geometries in the propeller design. Evaluation of propellers at higher thrust levels would provide insight in power reduction at these higher thrust levels. Finally, investigation of the propeller at additional downstream locations, incidence angles and azimuthal positions would further validate the benefits of wingtip-mounted propellers suggested in this research.

Contents

Nomenclature

Symbol	Parameter	Unit
α	Wing angle of attack	deg
α_0	Angle of attack at $c_l = 0$	deg
β	Local blade pitch angle	deg
$\beta_{0.7R}$	Blade pitch angle at 0.7R	deg
η	Blade efficiency	-
η_x	Axial regularization constant used in actuator disk	-
η_θ	Azimuthal regularization constant used in actuator disk	-
Γ	Blade circulation	$m^2 s^-1$
λ	Wing taper ratio	-
Ω	Propeller rotational velocity	rad/s
ρ	Air density	km/m^3
ρ_∞	Freestream air density	km/m^3
θ	Propeller rotation angle	deg
μ	Viscosity	-
AR	Wing aspect ratio	-
b	Wing span	m
c	Chord length	m
c_d	Two-dimensional drag coefficient	-
$c_{d,min}$	Two-dimensional minimum drag coefficient	-
C_D	Drag coefficient	-
C_{D_0}	Zero-lift drag coefficient	-
C_l	Two-dimensional lift coefficient	-
$C_{l,\alpha}$	Two-dimensional lift curve slope	1/rad
$C_{l,\alpha,stall}$	Two-dimensional lift curve slope beyond stall	1/rad
c_{l_0}	Two-dimensional lift coefficient at $c_{d,min}$	-
$C_{l,c}$	Two-dimensional lift coefficient with compressibility correction	-
$C_{l,lin}$	Two-dimensional inviscid lift coefficient	-
$C_{l,max}$	Two-dimensional maximum lift coefficient	-
$C_{l,min}$	Two-dimensional minimum lift coefficient	-
$C_{l,3D}$	Two-dimensional lift coefficient corrected for three-dimensional flow	-
C_L	Lift coefficient	-
C_P	Propeller power coefficient	-
C_p	Pressure coefficient	-
C_Q	Propeller torque coefficient	-
C_T	Propeller thrust coefficient	-
D_i	Induced drag	N
f	Exponent in XRotor drag determination - Reynolds scaling	-
J	Advance ratio	-

Symbol	Parameter	Unit
K_t	Thermal conductivity	-
M	Mach number	-
M_{crit}	Critical Mach number	-
N_{crit}	Critical amplification factor in e^N method by van Ingen	-
P	Pressure	Pa
P_∞	Freestream pressure	Pa
Q	Propeller torque	Nm
r	Local propeller radial position	m
R	Propeller radius	m
Re	Reynolds number	-
S	Effective temperature	K
T	Propeller thrust	N
T_{atm}	Freestream atmospheric temperature	K
T_{des}	Propeller design thrust	N
$T_{des,max}$	Maximum propeller design thrust	N
u	Velocity in x-direction	m/s
v	Velocity in y-direction	m/s
V_∞	Freestream velocity	m/s
V_{ax}	Axial velocity	m/s
V_{tan}	Tangential velocity	m/s
V_{tot}	Total velocity magnitude	m/s
w	Velocity in z-direction	m/s
Z	Number of propeller blades	-

1 Introduction

Historically aircraft have been using carbon-based fuels as their main energy source. First powering engines to spin propellers and decades later turbofans and turbojets became dominant. Next to this the propulsive sources are dominantly placed at the mid-wing, in front of the fuselage or in some cases at the tail. However, rising fuel cost and increasingly strict (noise) emission requirements have led to the search for alternatives in both energy sources and propulsion set-ups. Ever since the late seventies great engineering effort has gone into increasing the fuel efficiency and reduction of the noise profile of aircraft.

One of the concepts that has been explored is that of the wingtip-mounted propeller. In any wing with a finite span, energy is lost due to the lift-induced vortex that forms around and behind the wingtip. The general idea of a wingtip-mounted propeller is to recover some of this energy by exploiting the tangential flow field around the wingtip. This is done by placing a propeller at the wingtip in a pusher configuration; aft of the wing. Potential improvements are obtained in the form of increased propeller efficiency and lower induced drag of the wing.

Nevertheless propellers placed at the very end of the wing are nowhere to be found in today's general aviation aircraft. This is mostly because of aeroelastic problems and stringent one-engine-out requirements. These days such issues can be resolved by scaling down the propeller and using (distributed) electric propulsion. It is unclear what the effects of scaling down the propeller are and what propulsive gains can be achieved. Very limited numerical work to evaluate this concept has been done. A propeller optimized for this flow field has not been designed yet. Therefore, a lot is to be discovered in this field.

1.1. Previous research on wingtip-mounted propellers

The concept of wingtip mounted propellers is far from new, first introduced by the renowned engineer Charles Zimmerman. As early as the 1930s, Zimmermans' Vought V-173 1.1a utilised this concept, with counter-rotating propellers of nearly 5 meters in diameter at each wingtip [22]. The propellers rotated in opposite direction of the tip vortices, allowing for a small planform. With its large propellers at an odd location and the pancake-shaped body, the Vought remains a remarkable sight in aviation history. Capable of very short take-off and landing the V-173 prototype did far more than proof the concept Zimmerman proposed. The production version, the XF5U-1, promised similar performance in a larger package [27]. However, with the rise of the jet age the entire project was cancelled in 1947 due to lack of applicability and funding. The XF5U literally never took off.

Throughout the following years numerous calculations and wind-tunnel experiments were conducted to

(a) Vought's V-173; the 'flying pancake'. [22]

(b) NASA's X-57 Maxwell - a test bed for distributed electric propulsion and a large wing-tip propeller [48].

Figure 1.1: Existing and conceptual aircraft utilising wingtip-mounted propellers

further investigate the concept of wingtip-mounted propellers. Wind tunnel tests by Snyder [54] validated the ideas already shown by Zimmerman in the 1930s. Snyder concluded that a propeller rotating in opposite direction to that of the wingtip vortex core leads to an increase in wing lift and decrease in drag. Furthermore, Patterson [45] did important work at NASA's Langley Vortex Research Facility and showed that the strength of a tip vortex is reduced by forcing air into the vortex core. The latter is done by means of a propeller.

Fast forwarding to the late 80s, Patterson and Bartlett ([47], [44]) demonstrated the benefits of placing a propeller at the wingtip in a pusher configuration. They chose to investigate a pusher propeller because in this configuration no swirl over the wing is formed, which can be detrimental to the aerodynamic performance of the wing. A detailed description of Patterson's work will be presented in the upcoming section. The idea of his investigations were to validate the assumption that wingtip vortex could be used to provide favourable aerodynamic effects and enhance propeller performance. All this would lead to less power required. Patterson conducted multiple wind-tunnel tests with an untapered wing and SR-2 high-speed propeller immersed in the flow originating from the wingtip. The rotational direction of the propeller was opposite to that of the vortex core from the wing. He concluded that a 25% reduction in overall power required could be achieved, because of increased propeller thrust and reduction in lift-induced drag. Next to that an increased lift curve slope was found, most likely due to the injection of mass from the propeller into the vortex core. Note that this is in contrast to the statement by Brennan and Miranda [42]; who concluded that the reduction in required power is either due to increased propeller thrust (propeller aft of the wing) *or* due to a reduction in lift-induced drag (propeller in front of the wing). Whether or not this could also be due to a combination of this, as Patterson indicates, remains to be seen in this thesis work.

In later years more analytical and numerical work was done. Examples are the works of Loth and Loth [39], Miranda and Brennan [42] and Janus et al. [32]. Most notable is the work of Miranda and Brennan [42]. They described a numerical tool, PROPWING, in which various wingtip-mounted propeller configurations can be quickly explored. An analysis of the same wing and SR-2 propeller is described. Although simplified and generalised propeller aerodynamics were implemented in PROPWING, results were in line with those found by Patterson in his wind-tunnel tests. In the research done by Janus et al. [32] the computational results are again in accordance with previous experimental results, albeit showing a 10% lower drag reduction. This difference could be explained by the lack of wall interference in the simulation case, but present in the experimental wind tunnel tests.

Recently there has been renewed interest in the concept of wingtip-mounted propellers. For the first time in decades, NASA has reinstated its legendary X-Plane series. The newest X-Plane, the X-57 Maxwell, is aimed at demonstrating distributed electric propulsion using multiple propellers placed along the span of the wings (1.1b). The X-57 also uses a relatively large wingtip-mounted propeller driven by a high-efficiency electric

motor [58]. A number of large-scale projects in the field of personal air transport are ongoing at the time of writing. Nearly all of these proposed small-scale multi-rotor concepts utilise a form of wingtip-mounted propellers.

1.2. Suggested benefits of wingtip-mounted propellers

The possible benefits of installing a propeller in the wingtip vortex are multifold. The work done by Patterson ([47],[44]) serves as an excellent basis for this explanation. He executed extensive wind tunnel experiments at NASA's Langley High Speed Wind Tunnel, investigating the installed performance of a SR-2 high-speed propeller on an untapered wing with 13 inch chord length. Tests were conducted at $M = 0.7$, $Re = 3.82 \cdot 10^6$ and angles of attack of $-2° < \alpha < 4°$.

In figure 1.2a a velocity diagram of a wingtip-mounted pusher propeller is shown. The suggested drag reduction possible by installation of the propeller as found by Patterson is shown in figure 1.2b.

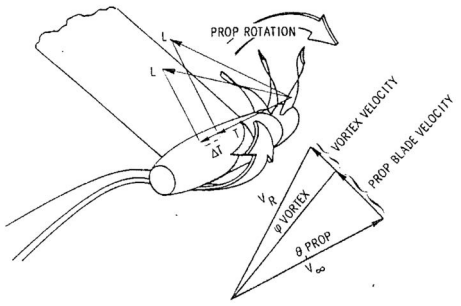

(a) Immersed propeller in the wingtip vortex from [44]

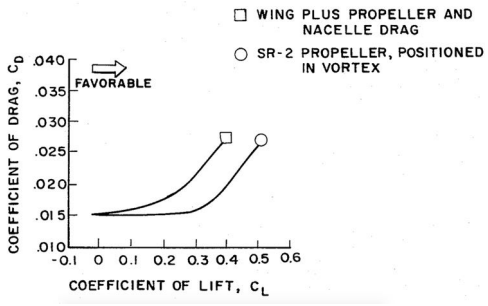

(b) Comparison of drag reduction due to nacelle configuration and propeller interaction from [46]

Figure 1.2: Wingtip-mounted propeller velocity diagram and suggested improvements in drag coefficients.

His research proved the possibility to recover energy from the wingtip vortices. At $C_L = 0$ no lift-induced tip vortex exists since no lift is generated. Patterson set the power required to maintain cruise condition but at the wing angle of attack $C_L = 0$ (and thus no beneficial tip vortex) as baseline. The angle of attack was gradually increased, thus introducing a tip-vortex, and the influence on the propeller performance was evaluated. As expected the required power was reduced by 13%, at $\alpha = 3°$. At a higher angle of attack a (stronger) wingtip vortex is formed. In turn, the effective propeller blade pitch β is increased because it is immersed in that vortex flow. Simply stated this means that the wingtip flow yields an effective increase in propeller efficiency and thus lowered power requirements. The experiment was replicated with an added outboard wing section. No reduction in power required with increasing lift coefficient was found, as is seen in figure 1.3a. This confirmed the assumption that indeed the wingtip vortex is the origin of this favourable effect. It was shown that only a propeller rotating in opposite direction of the wingtip vortex rotation can yield a reduction in power required. This is to be expected since rotating in the same direction would yield a decreased blade pitch angle, thus a higher RPM and power requirement.

It was also shown that induced drag reduction is possible because of the interaction between the propeller wake and the wingtip vortex flow. Because the vortex core flow is interrupted by the propeller the vortex dissipates and thus has a reduced effect on the wing downwash field. A weakened downwash field essentially means that the induced drag of the total installation is reduced. The nacelle incidence was set near-parallel to the cruise flight path. Thus the total frontal area of the nacelle and wing combination could be reduced. This lowered the wing drag by nearly 10 percent as shown in figure 1.3b

Combining all the above measures a possible drag reduction of nearly 30 percent was demonstrated at $C_L = 0.35$. Note that configurations utilizing electric engines do not necessarily need large hubs compared to

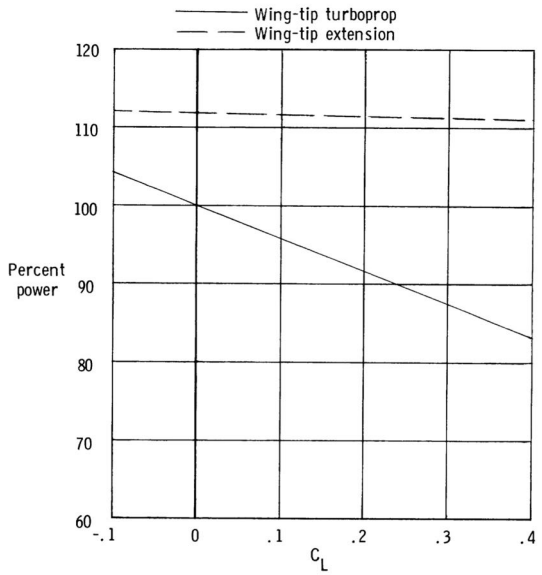

(a) The power requirement vs lift coefficient from [44]

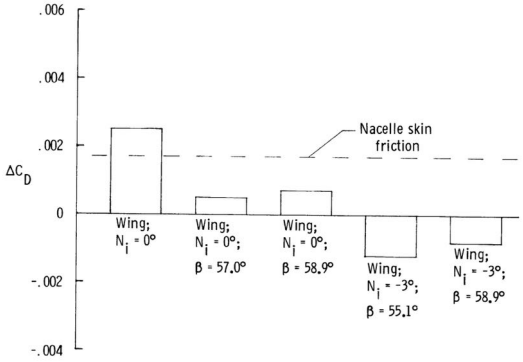

(b) Comparison of drag reduction due to nacelle configuration and propeller interaction from [44]

Figure 1.3: Power and drag reductions due to installation of wingtip-mounted propellers found by Patterson

the propeller diameter. Thus, drag reductions made possible by efficient nacelle placement and configurations might be smaller.

1.3. Problem statement and research goals

The goal of this research is to obtain quantified insight into the aerodynamic and propulsive efficiency gains of a pusher propeller when placed in a wing-tip flow field. As said the non-uniform inflow encountered by the propeller can be used to optimize the propeller performance and location, maximizing the propulsive gains by immersing the propeller in the wingtip vortex field. The effect of scaling down the propeller is however unknown. The question remains what the possible propulsive gains, upstream effects on the wing and implications for the propeller design are. When completed this project is of great value to the further development of (distributed) electrically powered aircraft.

Two main research questions are constructed with three sub-questions each:

1 ***What are the possible gains in propulsive efficiency by installing wingtip mounted pusher propellers?***

- 1.1 What are the characteristics of the flow field behind the wing-tip, in terms of in-plane and axial velocities?
- 1.2 What is the propulsive efficiency increase of the propeller when installing a wingtip-mounted pusher propeller?
- 1.3 What is the upstream effect of installing a wingtip-mounted pusher propeller?

2 ***What is the implication of this non-uniform inflow field for the propeller optimum design?***

- 2.1 What are the optimal blade geometry, blade pitch and advance ratio when designing the propeller for the given non-uniform inflow field?
- 2.2 To what degree can a lower-order tool be used to determine propeller performance subjected to non-uniform inflow fields?

2.3 What is the influence of propeller design parameters such as design thrust, radius and airfoil design in this context?

1.4. Research approach

This research consists of three subjects that have to be understood, modelled and investigated; the isolated wing and resulting wing-tip flow field, an isolated propeller and finally the combined setup and interaction of the wing and installed wingtip-mounted propeller. Therefore this research is divided as such. In figure 1.4 the steps to be taken are visualized.

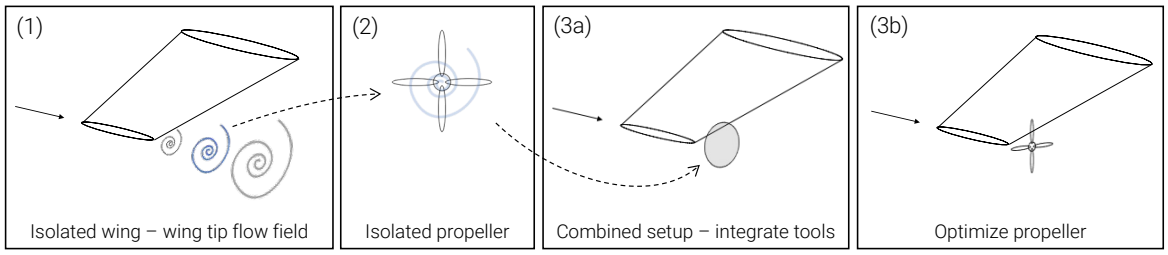

Figure 1.4: A schematic overview of the main parts of this research.

The goal of the first part is to quantify the near-field flow properties aft of a wingtip. For this, a simulation model will be set up. When the flow field behind the wingtip is known and understood, this can be used as 'input' to simulating the propeller that will be immersed in this flow field. Since it is essential that this flow field is simulated accurately and realistically, wind-tunnel studies will be used to validate this simulation.

The second part is focussed on a (isolated) propeller. The goal is to develop an aerodynamic analysis and optimisation tool for propellers with said non-uniform inflow. Within Delft University of Technology previous work on non-uniform inflow (pusher) propeller was done by van Arnhem [5]. However, the focus of his work was not on the design and optimisation wingtip-mounted propellers. It does provide a great basis for this thesis work. Again, a validation case will be used to provide insight in the capabilities and accuracy of the built tool. The wingtip flow field obtained in the first part will be used as input for the propeller. In doing so, initial insight in the performance of a propeller placed in non-uniform flow fields is gained.

In the final part of this research the individual parts (wing and propeller) are integrated. The goal is to combine the different modelling and simulation tools. This will be done using a higher-order computational fluid dynamics (CFD) tool, representing the propeller as an actuator disk (part 3a). Furthermore, optimization of the propeller blade geometry will be done in this stage (3b). A final validation case is foreseen by means of a RANS CFD simulation with fully resolved propeller. Combined this allows for extensive insight in the performance gains and interaction effects of the installed propeller.

1.5. Structure of this report

As explained in the previous section this research is split into three main parts. Thus the remainder of this report adheres to that structure and consists of three main parts. In each part relevant background information and literature is presented first. Then a description of the simulation tools set up and results obtained from the use of these tools follows.

In Part I the isolated wing and resulting flow field is first discussed in chapter 2. The CFD-simulation of an isolated wing is presented as validation study in chapter 3. Finally, a baseline wing to be used in the remainder of this research is simulated. This provides the flow field to be imposed on the propeller.

After the investigation of an isolated wing the isolated propeller will be discussed in Part II. Again a basis is formed by discussing the working principle of propellers and selection of suitable modelling tools in the

first chapter of this part: chapter 5. The aerodynamic analysis and optimisation tool for propellers with non-uniform inflow fields is presented in chapter 6. This tool will be validated using experimental data. Finally an isolated propeller CFD simulation is presented in chapter 7.

With both the isolated propeller and wing investigated and the necessary modelling tools built, the combined setup is explored in Part III. An extensive optimisation study of the propeller is presented in chapter 8. This will provide insight in the possible performance gains and optimal geometries of propellers with non-uniform inflow. An actuator disk implementation in this CFD-simulation is discussed in chapter 9, essentially coupling the lower-order and higher-order analysis tools. The upstream effects of installing the propeller will be quantified using this simulation setup. Finally a full CFD analysis of the combined setup and resolved propeller is presented in chapter 10. This is done to once more validate the propeller tool and provide accurate insight in the upstream effects and unsteady loading phenomena of the installed propeller. This report is concluded in chapter 11, providing answers to the stated research questions recommendations for further research.

I

Investigation and modelling of the wingtip flow field

The first part of this research is focussed on understanding the fundamentals and simulation of flow fields originating from a wingtip. With a proper analysis tool set up, the inflow conditions experienced by a propeller placed in the wingtip flow field can be accurately simulated. The main goals of this research part are:

- ☐ Discuss the fundamental principles of wingtip flow fields
- ☐ Select and implement a suitable simulation method for wingtip flow fields
- ☐ Validate the used simulation method with experimental data
- ☐ Describe and simulate a baseline wing, to which a wingtip mounted propeller can be added in a later part

2

Fundamentals of wingtip vortices and their simulation

Before investigating the possible benefits of wing-tip mounted propellers, it is important to understand the flow field originating from the wingtip. In this chapter the working principle of wingtip vortices, their formation process, dimensions and parameters that influence these vortex structures is presented. This will be discussed in sections 2.1 to 2.3. Next, an overview of suitable simulation methods, classifications and tools is presented in section 2.4. Finally a suitable methodology is selected in section 2.4.2.

2.1. Origins of wingtip vortices

When considering a finite wing a low-pressure region exists above the wing and a higher-pressure region exists below the wing; hence the wing is producing lift. Intuitively, some air will flow from the high-pressure region around the wingtips to the lower-pressure region above the wing. This flow around the wingtips forms the so-called wingtip vortex, trailing downstream of the wing. A clear illustration of this can be seen in figure 2.1a.

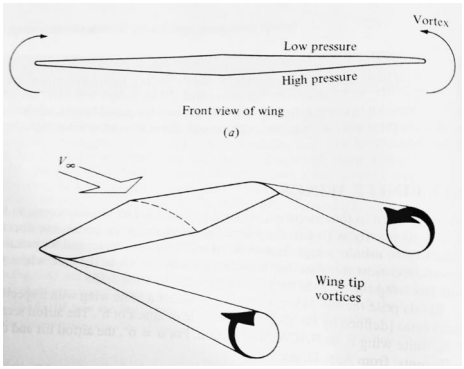

(a) Schematic representation of wingtip vortices [4]

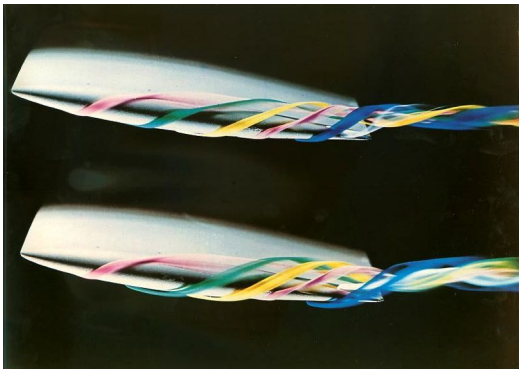

(b) Wingtip vortices visualized in coloured smoke [64].

Figure 2.1: Schematics of vortex formation and visualisation

These wingtip vortices drag the surrounding air downward inboard, causing the downwash aft of the wing. Outboard of the wing the opposite occurs. This downwash lowers the effective angle of attack of the wing and causes an increase in drag; induced drag. Because of this, finite wings have a lower lift coefficient and a higher drag coefficient compared to their infinite counterparts. As Janus [32] elegantly stated:

"Induced drag is not essential for the production of lift, but only an adverse consequence of that process."

The fact that wingtip vortices induce drag can be easily reasoned. According to Anderson [4]; the rotational kinetic energy in the vortices must come from somewhere; the propulsion system of the aircraft. Thus, more power must be generated to overcome the increase in drag due to the induced drag.

2.2. Describing the wingtip vortex

The aerodynamics of wing-tips (vortices) are highly complex and thus difficult to model accurately. Before describing the modelling techniques that can be used for wingtip vortices, it is important to define the physical phenomena and domain that is considered. In figure 2.2 a schematic view of the various regions that can be used to describe the vortex life originating from the wingtip is shown, as described in [23], [2] and [21]. In all these regions different flow phenomena and vortex life times are dominant. The main region of interest for this study is the very early wake and near field, extending a few chord lengths from the trailing edge of the wing. Note that this is only a fraction of the total vortex length; from the vortex origin at the wingtip it can take up to a few nautical miles for the vortex to dissipate.

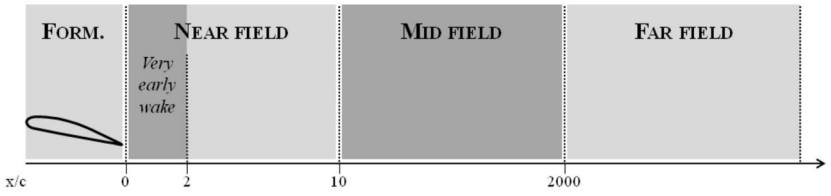

Figure 2.2: The various regions used to describe vortex life. [2]

Often wingtip vortices are described as if only a single vortex is formed behind the wingtip. This is not the case, as the wingtip vortex structure often consists of multiple, complex primary, secondary and even tertiary vortices. In research done by Guini [23] this is excellently described. From his observations after extensive wind tunnel experiments, he states the following:

- The primary vortex is created by the separating flow coming from the pressure surface of the wing. This vortex structure moves downstream along the wingtip. The origin of the primary vortex is either fixed somewhere along the chord, or oscillating in chord-wise direction when the wing is subjected to different pressure fields.
- A secondary vortex exists between the primary vortex and the wingtip. This vortex' dynamics determines the unsteadiness of the primary vortex to a large degree. The dynamics of the secondary vortex are in turn determined by the boundary layer separation unsteadiness of the wingtip.

Aft of the wing these two (or more) vortices revolve around each other and merge into a single, coherent vortex [17].

2.3. Factors influencing the wing-tip flow field

As explained, multiple vortices exist behind a wingtip. In research done by Chow et al. [13] it was indeed shown that flow of air from the pressure to the suction side of the wing starts as early as 30 percent of the chord length, starting the primary vortex. In the beautiful imagery made by Henri Werlé [64] this early crossing flow can be observed, see figure 2.1b. Although only for visualization purposes, it can be seen that the wing is under an angle of attack and the crossing of the flow occurs at approximately 20 percent of the chord.

The flow behind the wingtip is unsteady and has a large turbulence intensity. In contrast to the more aft mid-field the wake in the near field is also not axi-symmetric. Moreover, strong velocity gradients and axial perturbations are to be found in the vortex core [23]. The properties of the vortex structure in the near field are influenced by a number of things. In the so-called (very) early wake the geometry of the wing and wingtip are of great influence to the vortex structure and formation process. Next to this, also the free-stream flow is of influence. In the following, an overview of various geometrical and flow properties on the vortex formation and structure is shown.

- **Aspect ratio:** As found by Grow [25] decreasing the aspect ratio of the wing leads to increased vortex circulation and maximum swirl velocities.
- **Taper ratio:** Similar to the aspect ratio, increasing the taper ratio of the wing leads to the an increased vortex circulation and an increased maximum swirl velocities [25].
- **Angle of attack:** The angle of attack of the wing has a great influence on the vortex structure. Not only does it increase the circulation and swirl velocity of the vortex [25], also the level of turbulence within the vortex core increases [11]. Furthermore, it has been found that the core radius, axial velocities within the vortex and overall vortex strength are increasing with increasing angle of attack [10]. Finally, increasing angles of attack seem to heavily influence the strength of the secondary vortices, which are also associated with meandering of the vortex structure [23]. These findings have been confirmed by multiple studies, i.e. [3], [12], [9] and [33]
- **Reynolds number:** The influence of the Reynolds number on the vortex strength was investigated by Birch et al. [10]. In this experimental work it was found that the normalized vortex strength (expressed as $\frac{\Gamma}{cU}$) decreases with increasing Reynolds number. Furthermore, at lower Reynolds numbers ($1.63 \cdot 10^5$) it was observed that the flow structure around the vortex core became considerably less symmetric.
- **Tip and end-cap geometry:** A lesser investigated source of influence is the geometry of the wingtip. Not all researches have described the actual geometry of the tip; often the end plate shape is not discussed. The main influence of the tip geometry seems to be the development of the wingtip vortex and the following location of the peak vortex strength. Thompson [62] found that the vortex strength and structure is highly dependent on the shape of the wingtip. Furthermore Anderson [3] found that a flat end-cap caused multiple, strong, vortices in the near field. These vortices were less present in the experiment with round end caps in identical conditions. Chow et al. [13] mentioned that the aft location of the peak axial velocity of the wingtip vortex could be influenced by the geometry of the end cap. Guini [23] stated that a rounded tip does not force flow separation and a more axisymmetric vortex structure was observed. Secondary vortices were found to be weaker and thus the rolling up of the wake sheet was smoother for a rounded wingtip. In contrast, a square tip produced multiple strong vortices, resulting in highly unsteady vortex structures.

2.4. Suitable simulation of wing-tip vortices: RANS CFD

With a proper understanding of the working principle of wing-tip vortices and their behaviour, the next step is to investigate possible methods of simulating these complex flow fields. Because of the complexity in terms of pressure and velocity gradients, strong swirl and three-dimensional flow behaviour present in wingtip vortices a high-fidelity analysis method is required for accurate representation of said flow field. The use of CFD is preferred along with the proper turbulence model. The major CFD prediction methods are shown in figure 2.3, with the level of resolved scales shown.

In this figure the computational demands decrease from top to bottom; Direct Numerical Simulation (DNS) has the highest computational demands, Reynolds Averaged Navier-Stokes (RANS) the least. Both DNS and Large Eddy Simulation (LES) are prohibitively computationally expensive. Examples of wing-tip vortex

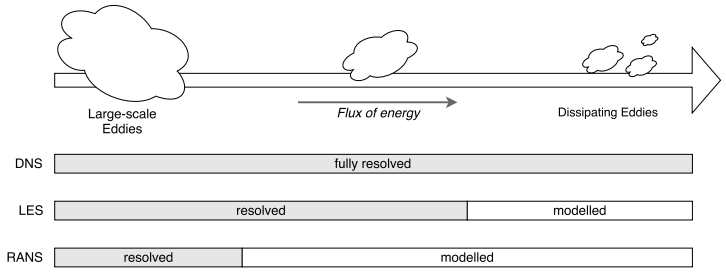

Figure 2.3: The major classification of CFD prediction methods [7]

related research is the work done by Lombard [38], O'Regan [49] and Uzun [63]. Because of the extreme computational demands DNS is only used in elementary research of simpler flows and validation of models.

2.4.1. Reynolds Averaged Navier-Stokes methods

In RANS the flow quantities are divided into a fluctuating and mean part, resulting in averaged Navier-Stokes equations. A set of equations is set up for the (steady) 'mean' flow, which by definition also includes the averaged turbulent quantities. This averaging over all turbulent scales means that RANS drastically lowers the computational demand because less grid points are needed. When the flow-field to be modelled is understood and a proper turbulence model is chosen, RANS has proved to be an excellent tool.

2.4.2. Suitable turbulence models

As stated previously, in RANS the Navier-Stokes equations are either time-averaged or ensemble-averaged. However, in the resulting set of equations there are more unknowns than equations; the closure problem. The so-called Reynolds stress tensor τ has to be approximated using turbulence models, solving the closure problem of RANS. A suitable turbulence model is essential to the accurate prediction of the flow field behind the wingtip.

Ideally, a turbulence model used to simulate the near field, wingtip vortices in particular, must be able to account for the strong streamline curvature, velocity gradients and solid body rotation that are present in tip vortices and the surrounding flow. Dacles-Mariani [15] states that both the original versions of Baldwin-Barth and Spalart-Allmaras (S-A) one-equation turbulence models are inadequate for the prediction of tip vortex flow. However, modifying the production terms to account for the stabilizing effect of the solid body rotation vastly improved both models. In comparison to experimental data, Dacles-Mariani [15] managed to simulate the viscous core size within two percent accuracy of the experiment, the core axial velocity within three percent and the static pressure coefficient within 11 percent. The experimental data of Chow [13] was used as validation case. Duraisamy [19] again showed that indeed the basic S-A turbulence model with the addition of a rotational correction in the production term makes it possible to obtain satisfactory accordance to experimental results.

In more recent work by Kim and Rhee [35] multiple turbulence models were compared to each-other and the experimental results of Chow [13]. They confirmed that tip vortices and the resulting wake could be modelled with a satisfactory accuracy using the S-A model with modified source terms. When computational resources are available the RSTM-based model provides the highest accuracy, as could be expected from a second-order closure model. They also showed that two-equation models (e.g. k-ϵ and k-ω) are unsuitable for the simulation of tip vortices, as they vastly under-predict the vortex strength and thus the resulting axial velocity. Although the S-A model dissipates too fast in the wake it shows a remarkable accordance to the experimental results, especially in the near field. Note that RANS-models are by definition unable to exactly represent the actual flow field. However, the goal is to obtain a representation of the flow field behind the

wingtip that is of sufficient accuracy to model a suitable propeller in that flow field.

In conclusion a suitable analysis method has been selected for the simulation of the wingtip flow field. In the remainder of this research the commercially available RANS-based CFD tool *ANSYS Fluent* is used. The S-A turbulence model is preferred because of the relatively low computational cost, applicability to transient propeller simulations and availability within ANSYS Fluent. In the following chapter the computational setup and simulation results will be presented.

3

Simulation and validation study of a wingtip flow field

With a proper understanding of the wingtip flow field and suitable simulation tools the next step is to simulate this non-uniform wingtip flow field. An accurate and realistic simulation of this flow field is essential as the results of this are used in determining the interaction effects with a wingtip-mounted propeller. In this chapter the CFD simulation of an isolated wing will be described. The goal of this simulation is to develop a valid simulation setup capable of accurately resolving the wingtip flow field. This validation study will provide a proper foundation for a more realistic use case to be used in later stages of this research.

The experimental setup of the validation case is described in section 3.1. The implementation of this test in a CFD simulation is described in section 3.2. Here the chosen domain and mesh properties, boundary conditions, solver settings and turbulence model are explained. The results obtained and comparison to the validation study are shown in sections 3.3 and 3.3.1. Grid (in)dependency, influence of freestream parameters and the use of a different turbulence model on the results are also explored. Finally, conclusive remarks ending this first part of the research are presented in section 4.5.

3.1. Description of validation study

To ensure that the used simulation setup is valid an extensive experimental study done by Chow et al.[13] is used as a validation case. In this study extensive flow properties of the near-field of the wingtip flow field are available. The same experiment is also used as validation study in the work done by Duraisamy [19], Dacles Mariani et al. [15], Uzun [63] and Churchfield and Blaisdell [14]. The experiments done by Chow [13] were conducted in the 32x48 inch low-speed wind tunnel of NASA's Fluid Mechanics Laboratory at NASA Ames Research Center. A rectangular half-wing model with a NACA0012 airfoil at an angle of attack of 10 degrees was tested. The wing had a chord length of 48 inch, a semi-span of 36 inch and a rounded tip which should produce rather axisymmetric wingtip vortices compared to squared wingtips [23] The aforementioned span includes the wingtip. Tests were conducted at a chord-based Reynolds number of $4.6 \cdot 10^6$ and a freestream velocity of $51.82 m/s$ ($170 ft/s$), thus at a Mach number of 0.15 considering a sea-level ISA temperature of $288 K$. Described in multiple researches that have investigated this experimental study (Churchfield and Blaisdell [14], Ahmad [1]) the freestream conditions referenced to by Chow are determined in a reference point just upstream of the wing. This reference point is at $x = -1.1344c$, $y = 0.3423c$, $z = 1.0492b$ relative to the trailing edge of the wing root. As this point is in the vicinity of the suction side of the wing, the measured velocity of

Table 3.1: Wing geometry properties

	Symbol	Value	Unit
Airfoil	-	NACA 0012	[-]
Angle of attack	α	10	degrees
Wing span	b	0.9144	m
Chord length	c	1.2192	m
Taper ratio	λ	1	[-]
Aspect ratio	AR	0.69	[-]
Wing tip shape	-	rounded	[-]

the flow is higher than that of the actual freestream velocity. The maximum freestream turbulence level was found to be 0.15%. In order to fix transition a strip of roughness elements was placed at approximately $0.04c$ from the leading edge. Refer to table 3.1 for all properties of the wing model, visualized in figure 3.2.

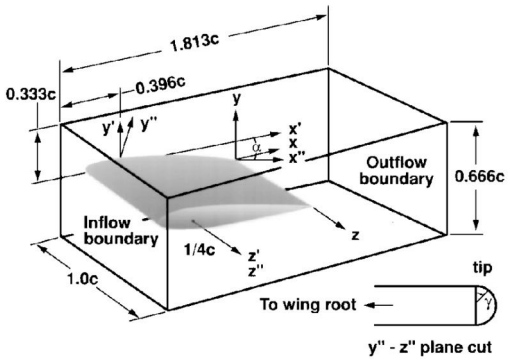

Figure 3.1: The test section used by Chow [13].

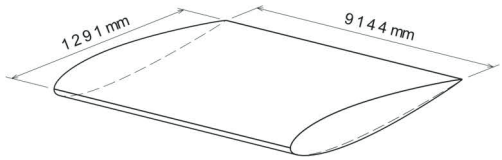

Figure 3.2: Wing geometry as used by Chow and this validation study, from [13].

In this study the wing model is large compared to the test section causing a significant blockage effect. The wind tunnel test section is shown in figure 3.1. Thus when modelling this experiment one should take into account the inviscid tunnel interference by modelling the wind tunnel walls. According to the author [13] severe viscous tunnel interference was avoided. The measurements that were done include turbulence intensity, velocity and pressure measurements at 12 cross planes, from $x/c \approx 0.125$ upstream of the wing to $x/c \approx 0.7$ behind the trailing edge of the wing. Furthermore the pressure coefficient at the wing surface and around the wingtip was measured. These extensive measurements give great insight in the near-field of the wing flow field. This allows for the validation of the flow field behind a wingtip simulated in a CFD model, described in the upcoming section.

3.2. CFD analysis setup

In this section the simulation of the validation study by Chow [13] is described. The computational setup and results obtained from this simulation are presented. Concluding, the comparison with the validation case will show the validity of this setup for the simulation of wingtip vortices.

3.2.1. Domain geometry

The computational domain is constructed to match the wind tunnel setup where possible. In order to avoid convergence problems, the inflow and outflow boundaries are placed at a farther distance than those in the experiment. This is also suggested in the work of Churchfield and Blaisdell [14] and Ahmad [1], to ensure that the solution found is free of boundary effects at the inflow and outflow boundaries. Inviscid tunnel

interference due to the large blocking is accounted for by positioning the wind-tunnel walls as was done in the experimental work.

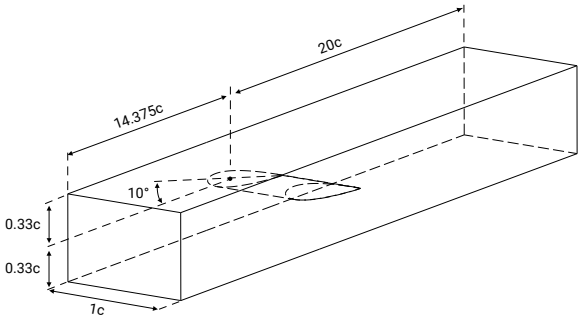

Figure 3.3: Schematic overview of computational domain used to simulate the isolated wing (not to scale)

In figure 3.3 a schematic overview of the computational domain used is shown. For clarity, the figure is not to scale. The inflow boundary is placed at approximately 14 chord lengths from the wing quarter chord point, the outflow boundary at a distance of 20 chords lengths. The wing is set to 10° angle of attack (around the quarter chord).

3.2.2. Mesh properties

The described domain in the previous sections was used to construct a suitable mesh. This was done in ANSYS Meshing [30]. In table 3.2 an overview of the mesh properties can be found. General volume refinements, wall refinements and growth rate determine the mesh sizing throughout the domain. In proximity of the wing volume refinements have been applied, as well as on the wing surface. The wing surface was meshed as a 'mapped mesh' to allow for better alignment with the flow and improve the quality of the boundary layer. Furthermore this drives the cell refinement in areas of large curvature, where refinement is desired. Number of divisions were specified in stream-wise and span-wise direction, with extra refinement at the wing leading- and trailing edge. The rounded wingtip complicates meshing, both the leading- and trailing edge tip are unstructured triangular meshes. To properly capture the boundary layer on the wing surface an inflation layer was specified. First layer thickness was specified to obtain a y^+-value of 1 or lower at the wing surface, to capture the viscous sub-layer with this turbulence model. The number of layers was set in order to capture the full boundary layer of the wing.

Table 3.2: Mesh properties of isolated wing CFD

Parameter	**Value/Method**
Mesh type	Unstructured
Element types	
Volumes	Tetrahedral
Walls	Triangular
Growth rate	1.2
Inflation layer (wing surface)	
Element type	Prismatic
First layer thickness	$7 \cdot 10^{-6}$ m
No. of layers	35
Growth rate	1.2
Advanced size function	Proximity and curvature
Relevance center	Fine

Mesh dependency study - properties

Different levels of refinements were investigated in a mesh dependency study to study the solution dependency on the mesh. Furthermore a trade-off could be made between the size and refinement of the mesh and resulting accuracy. Six different meshes have been made, of which an overview can be found in table 3.3. Starting from a baseline mesh (the 'medium' case) changes in volume- and surface sizes were made. A refinement of 25% and coarsening as low as 40% in terms of length parameters determining cell size was done with respect to the baseline 'medium' mesh. The inflation first layer thickness and growth rate were not changed, since inflation layers should be sized to obtain a maximum y^+-value of 1 when using this turbulence model if one wants to capture the viscous sub-layer. A comparable number of nodes was used in other studies investigating Chow's wind tunnel tests; the baseline mesh of Churchfield and Blaisdell [14] had $4.5 \cdot 10^6$ nodes. Note that the goal of this mesh dependency study was not to find the smallest mesh capable of accurately representing the problem at hand, but to prove the validity of this simulation setup. Therefore a more efficient and most likely smaller mesh could be constructed, for example by adaptive refinement in the vortex region. The results of the mesh dependency study are shown in section 3.3.1.

Table 3.3: Overview of meshes generated for mesh dependency study

Mesh	Refinement	Name	No. of nodes
6	0.4	Extra Coarse 3	588,247
5	0.5	Extra Coarse 2	953,222
4	0.6	Extra Coarse	1,408,446
3	0.75	Coarse	2,538,798
1	**1**	**Baseline**	**4,282,721**
2	1.25	Fine	8,567,204

3.2.3. Boundary and operating conditions

All the specified boundary conditions in ANSYS Fluent are described in the following. In table 3.4 the operating conditions and flow parameters required for boundary condition specification are shown. Variables shown in italic are described in the experimental work. The operating temperature $T_{s,\infty}$ is assumed to be the ISA standard temperature at sea level. All other required parameters can be determined using isentropic relations as described in appendix A. In table A.1 (appendix A) the resulting fluid properties used for air are discussed.

Table 3.4: Boundary and operating conditions specified in the domain - variables in italic are specified in the experiment.

	Symbol	Value	Unit
Mach number	M_∞	0.1532	[-]
Freestream velocity	V_∞	51.82	m/s
Freestream turbulence intensity	T_u	0.15	%
Chord-based Reynolds number	Re_c	$4.6 \cdot 10^6$	[-]
Static (operating) temperature	$T_{s,\infty}$	288.15	K
Total temperature	T_t	289.48	K
Freestream static pressure	$P_{s,\infty}$	107760	Pa
Freestream total pressure	$P_{t,\infty}$	109510	Pa
Eddy viscosity ratio	$\mu_{t,\infty}/\mu_\infty$	0.21044	[-]

- **Inlet** At the inlet of the domain a total pressure $P_{t,\infty}$ and temperature $T_{t,\infty}$ was specified to match the wind tunnel freestream conditions as described in section 3.1. It was assumed that the ISA standard

temperature at sea level is applicable, 288.15K. In ANSYS this boundary was set to be a pressure inlet boundary type.

The freestream turbulence level measured during the experiment was 0.15%. It is suggested by Rumsey and Spalart [52], [56] to base freestream levels set in the model on different considerations than the measured wind tunnel turbulence intensity. In their research they investigated the integrity of the turbulence quantities in the boundary layers present and ways to prevent rapid decay of the turbulence intensity. Their proposed way to do this is by specifying the turbulent viscosity ratio $\mu_{t,\infty}/\mu_\infty$. Based on the suggested ratios of kinematic viscosity $\tilde{\nu}_\infty/\nu_\infty$ a value of 0.21044 for $\mu_{t,\infty}/\mu_\infty$ is used. Note that this value is independent of the Reynolds number.

- **Wind tunnel walls** All wind tunnel walls are assumed to be inviscid walls as no (severe) viscous interference of the wind tunnel walls existed in this test. Furthermore, the exact geometry of the wind tunnel is unknown. As the boundary layer thickness and properties formed on the wind tunnel walls depend on the geometric features upstream of the test section, this would have to be assumed and possibly influence the final results. In ANSYS the boundary type required for the wind tunnel walls is 'symmetry'. This way the presence of the wind tunnel walls is simulated, modelling the inviscid tunnel interference.
- **Outlet** At the outlet of the domain the static pressure is set to equal the undisturbed (or freestream) static pressure. Note that the pressure profile over this domain is averaged, favourable to simulation convergence. In ANSYS this boundary is specified as a 'pressure outlet'. The total temperature T_t is also specified at this boundary. Because of the large blockage effect of the wing model in the 'wind tunnel', an average mass flow is specified at this exit boundary. This mass flow $\dot{m}_{outlet}$ is set equal to that over the inlet boundary, as conservation of mass should occur over the domain. A similar strategy was proposed by Churchfield and Blaisdell [14].
- **Wing** The surface of the wing model is set as a 'no-slip wall', thus assuming that the fluid velocity with respect to the wing surface is zero. The boundary layer is captured by an inflation layer as described in section 3.2.2.

3.2.4. Solver and setup

The entire simulation is performed in ANSYS Fluent 17.1. The flow is considered to be compressible and thus the equation of state is modelled as an ideal gas, along with the use of the energy equation. Dynamic viscosity is determined using Sutherland's law. In an attempt to reduce the number of iterations required to arrive at a converged solution, an initial solution is obtained using the built-in FMG initialization feature in ANSYS Fluent. By solving the Euler equations for inviscid flow using first order-discretization and on a limited number of coarse grids, a good initial solution can be found in a very limited time [29]. This can reduce the number of required simulation iterations greatly (up to a factor of five) and is thus computationally inexpensive.

In ANSYS Fluent a second-order discretization was used for all flow variables. As for time discretization, the pseudo-transient solution method was used to aid convergence of the simulation. When using this pseudo-transient option one has to specify a so-called fluid time scale. After the first few hundred iterations this timescale factor is increased, again to increase the convergence speed. During simulations the solver residuals, fluxes of velocity, mass, pressure over the inlet and outlet, lift- and drag coefficients are monitored. All simulations done converged within 2500 iterations.

Turbulence model

In order to accurately represent the flow field of the wing a suitable turbulence model is essential. In the previous chapter, section 2.4, various suitable turbulence models were investigated. The Spalart-Allmaras (S-A) turbulence model with modifications proposed by Dacles-Mariani [15] also accounts for the effect of mean

strain rate on turbulence production. Although the S-A model is a simple one-equation turbulence model, it showed to be very capable of accurately representing the wingtip vortex in the near field in other studies, as described in section 2.4.2.

3.3. Results

In this section the results of the simulation study will be presented. First the dependency of the solution on the mesh chosen is discussed. Next, a comparison of the simulation results and the experimental data is made. Finally the influence of the turbulence model and freestream turbulence properties are discussed. All this will provide insight in the validity of using this simulation setup to simulate the wingtip vortex. Results are presented in the form of contour plots at the various cross planes, pressure distributions at various span wise positions and samples through the cross planes at various span wise positions.

3.3.1. Mesh dependency study

As described in section 3.2.2 the baseline mesh was coarsened up to a factor of 0.4 and refined by 25% to investigate the solution dependency on the chosen mesh. In table 3.5 the results in terms of lift- and drag coefficient are shown. Furthermore, the velocities in the vortex core are listed for different meshes, the ideal mesh and the experiment.

Table 3.5: Overview of results obtained from the mesh dependency study. Experimental results, the ideal solution from GCI and resulting discretization and model errors are listed.

Mesh	**Refinement**	**Name**	**No. of nodes**	C_L [-]	C_D [-]	$\frac{u}{U_\infty}$	$\frac{\sqrt{v^2+w^2}}{U_\infty}$
6	0.4	Extra Coarse 3	588,247	0.6699	0.1903	-	-
5	0.5	Extra Coarse 2	953,222	0.6683	0.1899	-	-
4	0.6	Extra Coarse	1,408,446	0.6672	0.1888	1.0133	0.4456
3	0.75	Coarse	2,538,798	0.6675	0.1880	1.1014	0.6134
1	**1**	**Baseline**	**4,282,721**	**0.6606**	**0.1866**	**1.1763**	**0.7256**
2	1.25	Fine	8,567,204	0.6605	0.1876	1.2637	0.8217
-	-	Idealised mesh (ϕ)	Infinite	0.6827	0.1863	1.3544	0.9815
-	-	Experimental results	-	-	-	1.4245	0.9126
-	-	Discretization error	-	-	-	13.14%	26.07%
-	-	Model error	-	-	-	4.92%	6.38%

The maximum deviation from the baseline results are 0.01% for both C_L and C_D. In the next section (section 3.4.3) the pressure distribution over the wing found using the medium, fine and coarse meshes is shown in figure 3.20. Only at the very tip of the wing a small discrepancy in C_p can be observed. Using the coarser mesh (no. 3), the pressure coefficient is slightly under-predicted at $z/b = 0.9$.

Grid Convergence Index - overall aerodynamic properties

In an attempt to justify the use of the baseline mesh and to obtain guidelines for further calculations, the method of Grid Convergence Index (GCI) as proposed by [50] has been applied. Using this method the uncertainty of grid convergence is quantified. Note that this only gives insight in the discretization error of the simulation, as it can be assumed that the used code (ANSYS Fluent) and implemented turbulence model is verified and validated. Here, a least squares version of the GCI method is used, described by Eça and Hoekstra [20]. In figure 3.4 the least-squares fit of the found C_L and C_D values for the six different meshes is plotted, showing the asymptotic fit found for both parameters. The fit denoted by $p = 2$ has been used.

The estimated error $U_{\phi,rel}$ in C_L and C_D of values found using the baseline grid (no. 2) with respect to the theoretical solutions would be 0.045% and 0.598% respectively. The extrapolated theoretical values ϕ_0 are

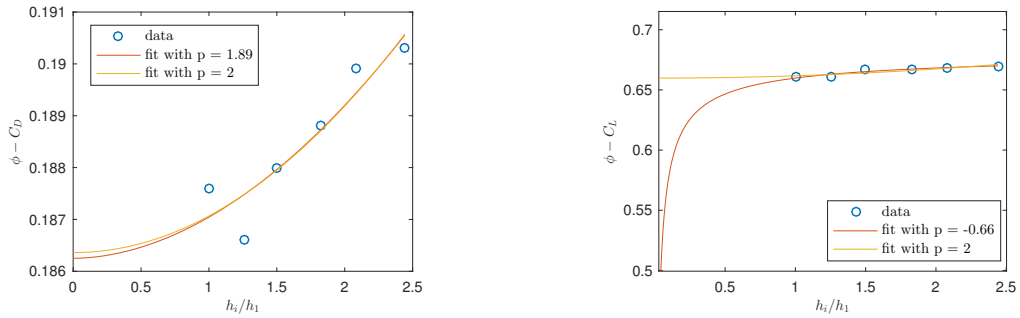

(a) C_D vs. mesh refinement (b) C_L vs. mesh refinement

Figure 3.4: Least-squares fit of C_L and C_D versus average cell size

found to be 0.6827 and 0.1863 for C_L and C_D respectively. These quantities are also listed in table 3.5. It is concluded that the use of the baseline grid is justifiable, providing a reasonable trade-off between cell count and accuracy.

GCI and discretization errors - flow field through vortex core

In table 3.5 results from a convergence study for flow velocities at the vortex core are also listed. At the vortex core location ($x/c = 0.24$ and $Z = 0.8$) the in-plane and axial velocity quantities are determined for four different mesh refinement levels. Using these values and the GCI-method extrapolated and ideal values are obtained, listed in table 3.5. These are in turn compared to the velocities found in the experimental validation study. With this difference, one can determine the model error of the used computational setup. In this case the model error is found to be 4.92% in terms of axial velocities and 7.54% in terms of in-plane velocities in the vortex core. The resulting discretization error for that location and the baseline mesh is found to be 13.14% in terms of axial velocities and 26.07% in terms of in-plane velocities. Note that this is an extreme scenario, and the velocity discrepancies are an order of magnitude smaller just outside the vortex core region. This is clearly visible in figure 3.19, further discussed in section 3.4.2.

Contour plots - visualizing the effect of grid refinement

In figures 3.5 to 3.8 contour plots of the normalized axial velocity u/U_∞ and the normalized crossflow velocity $\frac{\sqrt{v^2+w^2}}{U_\infty}$ at $x/c = -0.12$ and $x/c = 0.24$ with respect to the trailing edge of the wing are shown. It can be seen that the results obtained using the different meshes are nearly identical. As expected the build-up of the boundary layer over the wing (inboard) is identical, as is the shape of the vortex structure. Noticeable is the difference in vortex strength; especially seen in the dissipation of the vortex. The axial and crossflow velocities decrease faster for a coarser mesh moving downstream. With the finer mesh the vortex strength seems to dissipate at a slower rate, indicated by the higher velocities in the vortex region at $x/c = 0.24$, seen in figures 3.7 and 3.8. The opposite effect occurs when using a coarser mesh, where lower vortex core velocities are found. This behaviour is also found by e.g. Kim and Rhee [34], showing a clear correlation between vortex strength, dissipation speed and mesh density.

3.4. Validation of isolated wing simulation

In this section the obtained simulation results will be compared to measurement data of this experiment. As stated before Chow et al. [13] conducted velocity and pressure measurements at 12 cross planes; $x/c = -1.140; -0.596; -0.399; -0.202; -0.119; -0.015; 0.000; 0.121; 0.241; 0.448; 0.6729$ relative to the trailing edge of the wing. Velocity in three directions and static pressure was measured at these planes. Contour plots of these values give insight in the vortex formation and structure. Additional cut-planes through the available cross planes provide a detailed view of the flow behaviour at selected spanwise positions.

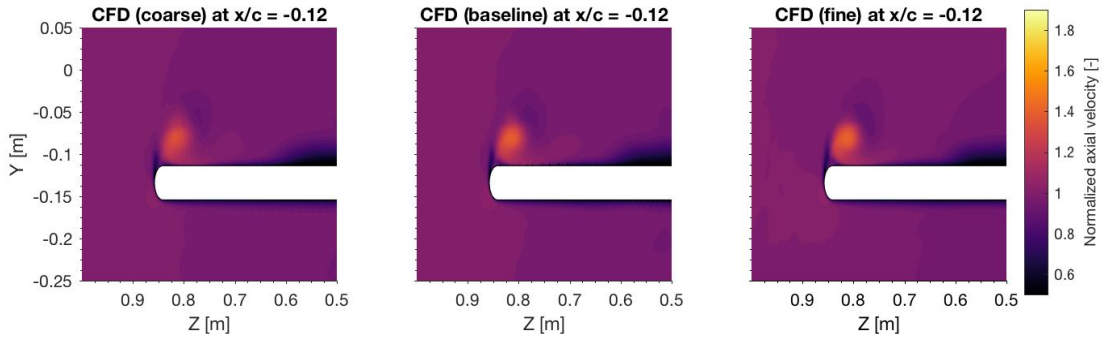

Figure 3.5: Comparison of baseline, medium and fine mesh. Contour of normalized axial velocity $\frac{u}{U_\infty}$ at $x/c = -0.12$

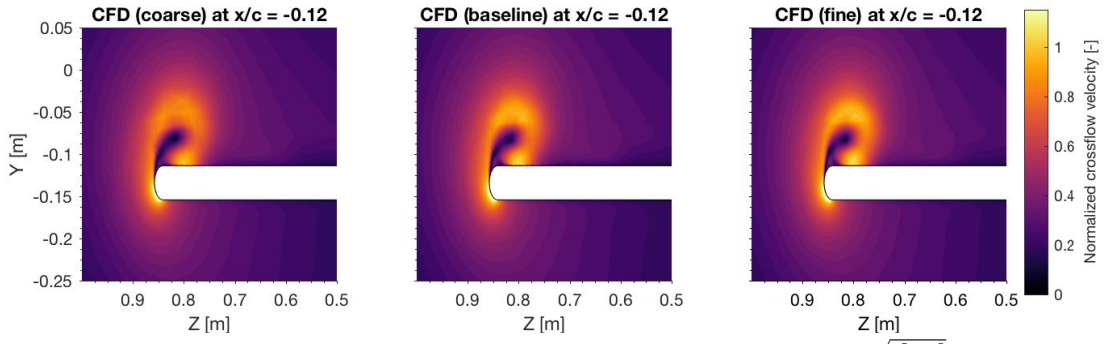

Figure 3.6: Comparison of baseline, medium and fine mesh. Contour of normalized crossflow velocity $\frac{\sqrt{v^2+w^2}}{U_\infty}$ at $x/c = -0.12$

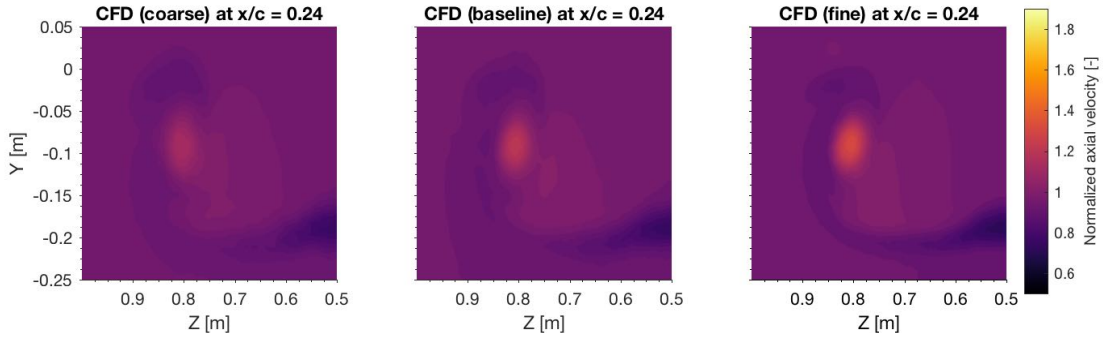

Figure 3.7: Comparison of baseline, medium and fine mesh. Contour of normalized axial velocity $\frac{u}{U_\infty}$ at $x/c = 0.24$

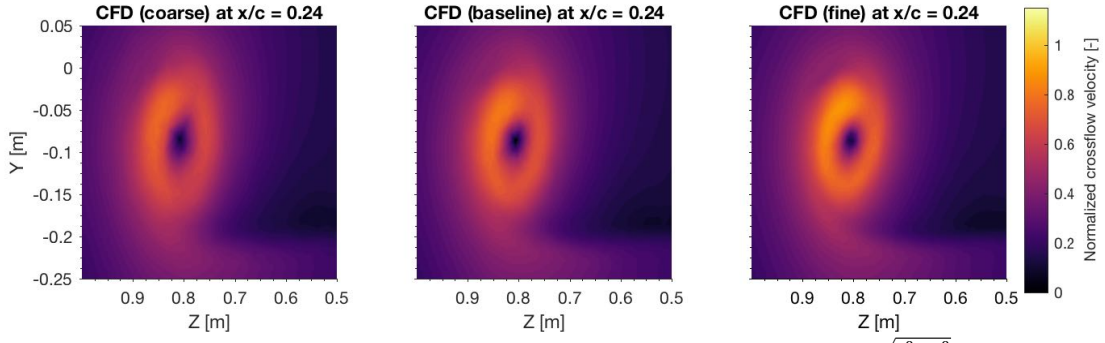

Figure 3.8: Comparison of baseline, medium and fine mesh. Contour of normalized crossflow velocity $\frac{\sqrt{v^2+w^2}}{U_\infty}$ at $x/c = 0.24$

3.4.1. Contour plots of normalized axial and crossflow velocities

In figures 3.9 to 3.12 contour plots of the normalized axial velocities are shown. Next to that the crossflow (in-plane) velocities are shown in 3.13 to 3.16. It can be seen that the vortex structure is similar, as is the build-up of the boundary layer over the wing.

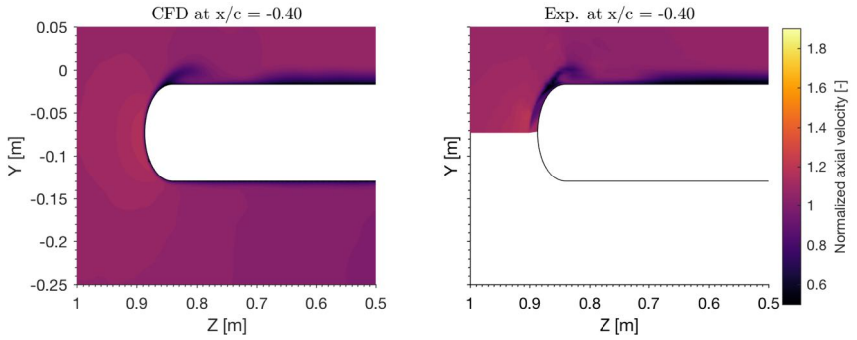

Figure 3.9: CFD (Mesh 1 - baseline) vs experimental results. Contour plots of the normalized axial velocity $\frac{u}{U_\infty}$ at $x/c = -0.399$

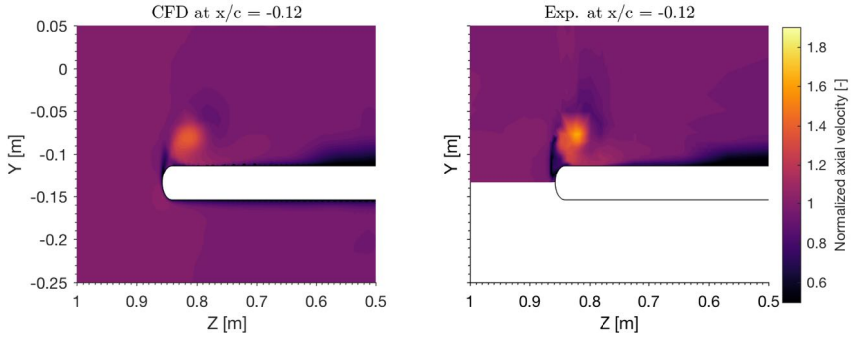

Figure 3.10: CFD (Mesh 1 - baseline) vs experimental results. Contour plots of normalized axial velocity $\frac{u}{U_\infty}$ at $x/c = -0.119$

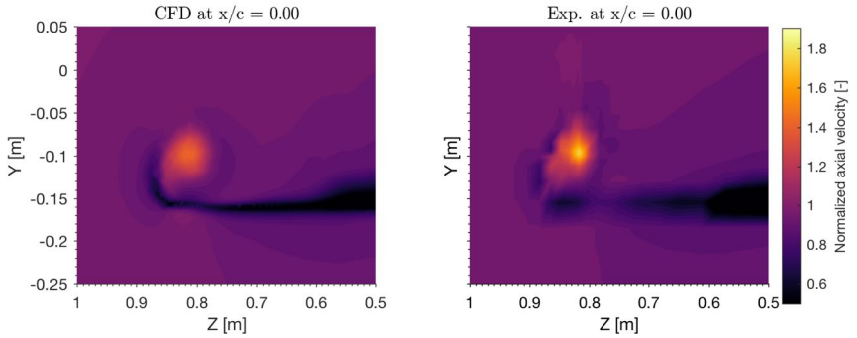

Figure 3.11: CFD (Mesh 1 - baseline) vs experimental results. Contour plots of normalized axial velocity $\frac{u}{U_\infty}$ at $x/c = 0$

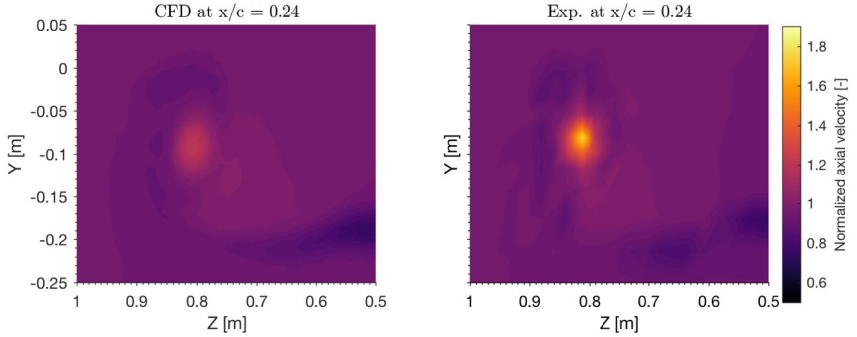

Figure 3.12: CFD (Mesh 1 - baseline) vs experimental results. Contour plots of normalized axial velocity $\frac{u}{U_\infty}$ at $x/c = 0.241$

3.4.2. Cut-planes of normalized axial and cross flow velocities

Although contour plots provide great insight in the flow field properties, a simple line plot of a 'slice' of the same cross-plane can provide even more insight. In figures 3.17a to 3.18c the results obtained using the 'baseline' mesh are compared to the experimental results. Please note that the experimental results have

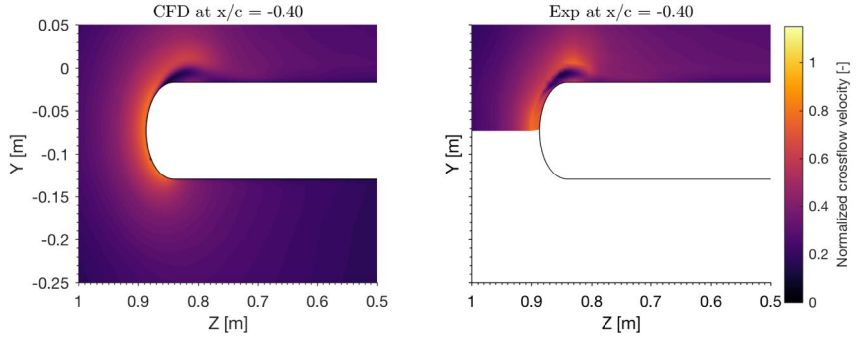

Figure 3.13: CFD (Mesh 1 - baseline) vs experimental results. Contour plots of normalized crossflow velocities $\frac{\sqrt{v^2+w^2}}{U_\infty}$ at $x/c = -0.399$

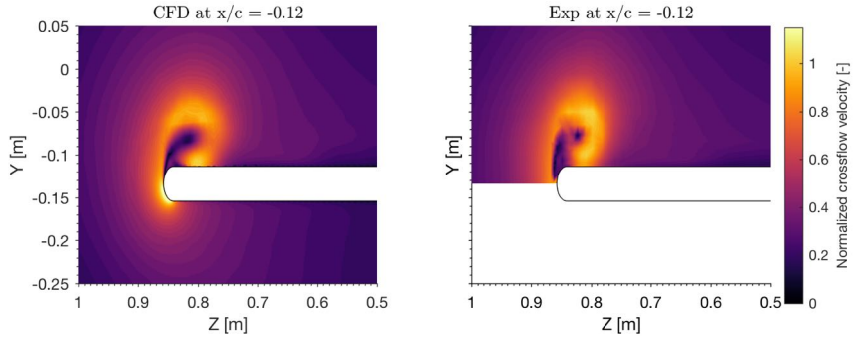

Figure 3.14: CFD (Mesh 1 - baseline) vs experimental results. Contour plots of normalized crossflow velocities $\frac{\sqrt{v^2+w^2}}{U_\infty}$ at $x/c = -0.119$

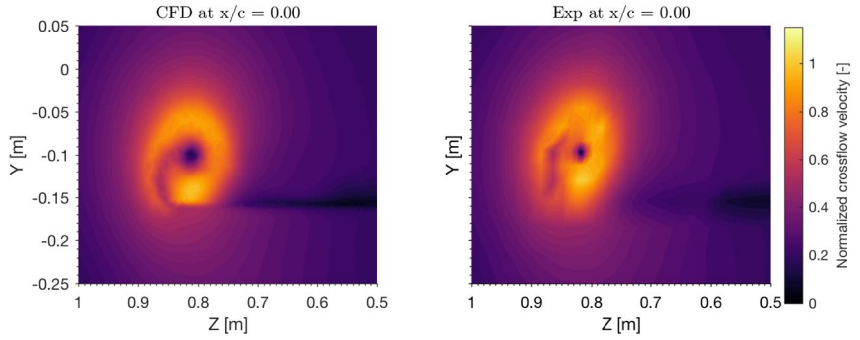

Figure 3.15: CFD (Mesh 1 - baseline) vs experimental results. Contour plots of normalized crossflow velocities $\frac{\sqrt{v^2+w^2}}{U_\infty}$ at $x/c = 0$

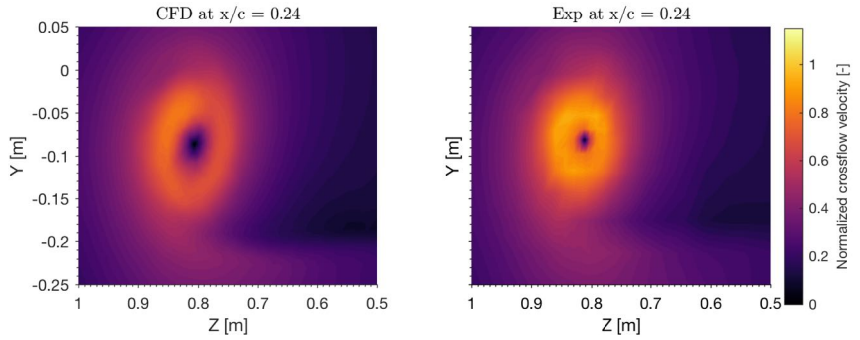

Figure 3.16: CFD (Mesh 1 - baseline) vs experimental results. Contour plots of the normalized crossflow velocities $\frac{\sqrt{v^2+w^2}}{U_\infty}$ at $x/c = 0.241$

been interpolated for clarity; hence the harsh transitions in values near the wing surface. Plots shown are at the planes $x/c = -0.119$ and $x/c = 0.241$, at 50, 70 and 90% of the span. Additional locations are shown in

appendix A, section A.2.

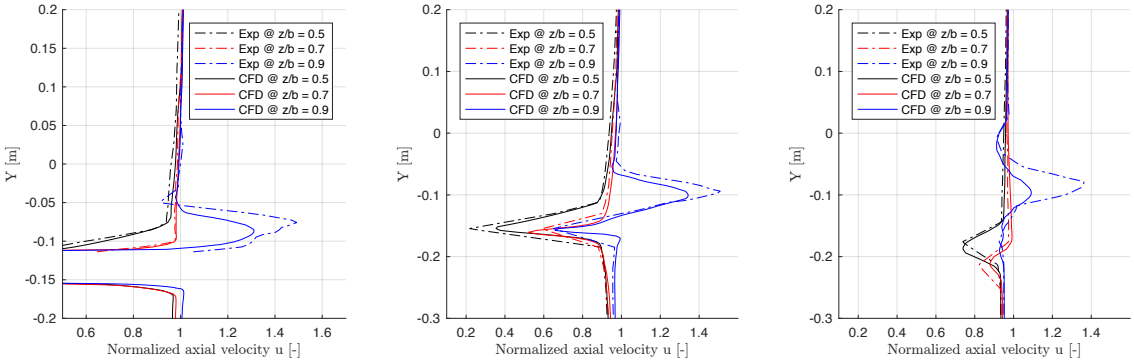

(a) $x/c = -0.12$ (b) $x/c = 0.00$ (c) $x/c = 0.24$

Figure 3.17: Comparison of CFD (Mesh 1 - baseline) and experimental results in the zy-plane at $x/c = -0.12; 0.00; 0.24$. Plots of the normalized axial velocity $\frac{u}{U_\infty}$ at 50, 70, 90% span

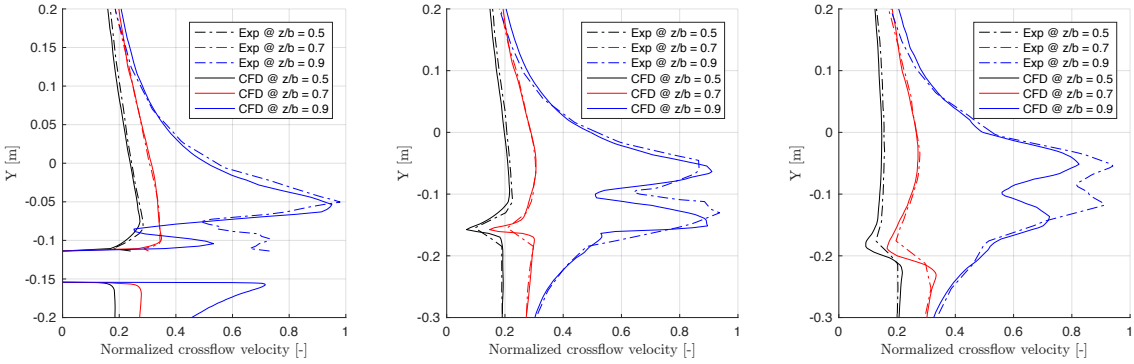

(a) $x/c = -0.12$ (b) $x/c = 0.00$ (c) $x/c = 0.24$

Figure 3.18: Comparison of CFD (Mesh 1 - baseline) and experimental results in the zy-plane at $x/c = -0.12; 0.00; 0.24$. Plots of the normalized crossflow velocities $\frac{\sqrt{v^2+v^2}}{U_\infty}$ at 50, 70, 90% span

Again it can be seen that the flow field is accurately represented with the largest deviation at 90% span. Note that the vortex geometry is accurately represented, as velocity excesses occur at the same positions. The vortex strength is slightly under-predicted, visible here at the very wingtip. In the simulation lower velocity quantities in both axial and in-plane direction are found. Because of the high pressure gradients present at this location, the error at a different sampling position, e.g. 89%, span could be much lower.

Similar cut-plane line plots were made at the exact location of the vortex, where also the grid convergence has been evaluated. These cut-planes are shown in figure 3.19. Both axial- and in-plane normalised velocities are shown at $x/c = 0.24$ and $Z = 0.8$, through the vortex core location.

The under prediction of the velocity quantities is clearly visible in figures 3.19a and 3.19b, for all mesh refinement levels. Again, the trend, shape and location of the velocity gradient in the vortex core is accurately simulated. It is seen that the finest mesh provides the best estimate of normalised axial velocities. In the actual vortex core (at $Y = -0.08$ m) all CFD results show a significant under prediction compared to the experimentally found in-plane velocities. Nevertheless, the location of this velocity gradient is correct and the region in which the discrepancy is found is limited ($0.02m$). When installing a propeller the spinner and nacelle will be subjected to the flow in this region. The majority of the flow field imposed on the propeller is represented with a higher accuracy. Thus a limited performance impact can be expected.

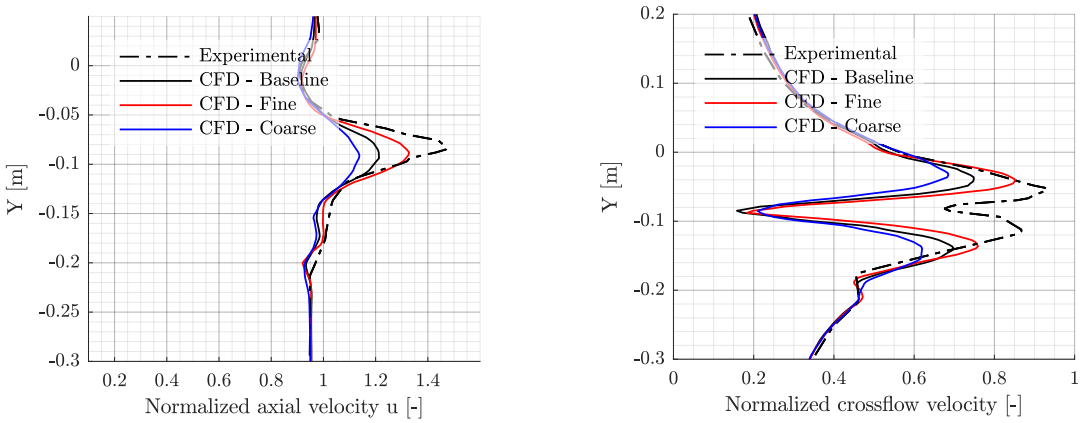

(a) Normalized axial velocities $\frac{u}{U_\infty}$.

(b) Normalized in-plane velocities $\frac{\sqrt{v^2+w^2}}{U_\infty}$.

Figure 3.19: Comparison of different CFD meshes and experimental results in the zy-plane through the vortex core: $x/c = 0.24$ and $z = 0.8$. Both normalized axial- and in-plane velocities are shown.

3.4.3. Pressure coefficients along the wing

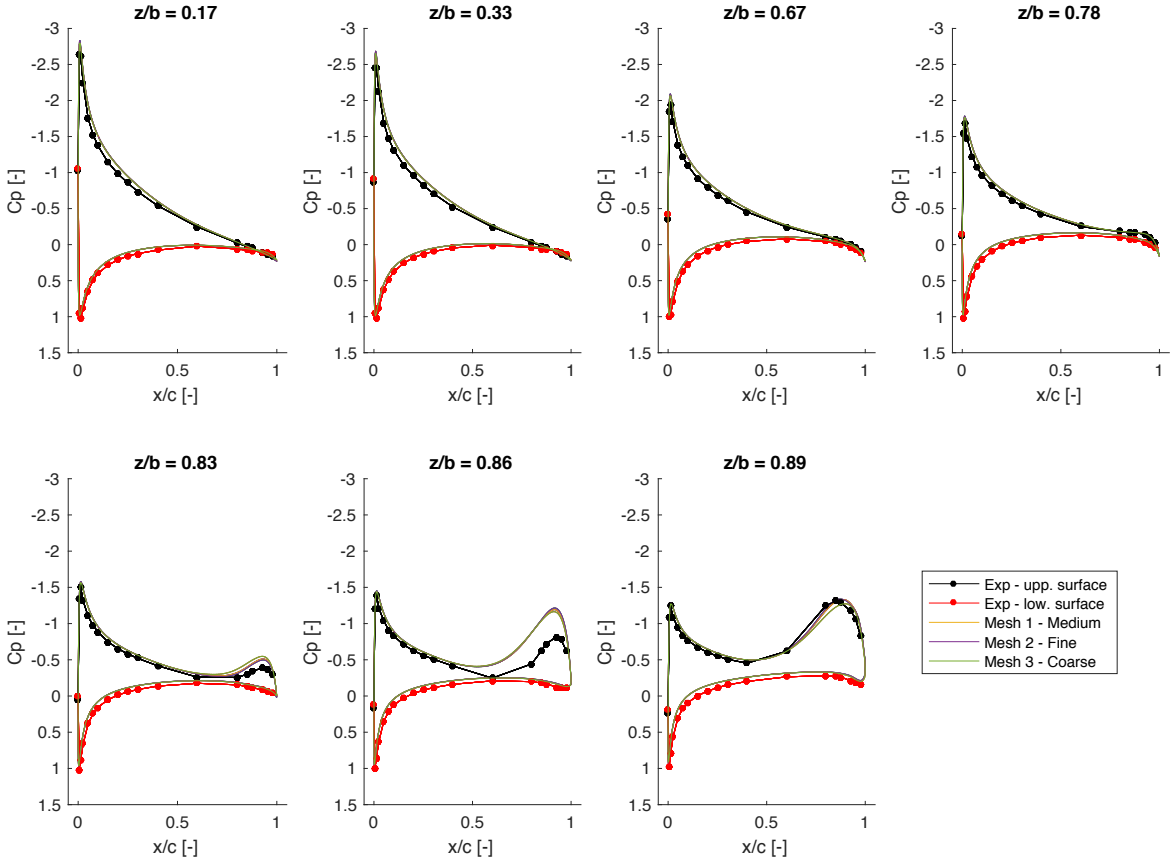

Figure 3.20: Comparison of the experimental pressure coefficients at various span-wise positions and those simulated using three different meshes in CFD.

In figure 3.20 it is seen that the simulated pressure coefficients are in good agreement with the experimental results, especially inboard up to 80% span. Near the wingtip computed pressure coefficients are over

predicted compared to the experimental results. Note that a large suction peak is present at this location. Important is the close resemblance of the trend simulated and found in experimental research. The location and shape of the suction peak is correctly predicted. To put these findings into perspective, the simulated results obtained here bear closer resemblance to experimental results than found in the work of e.g. Churchfield and Blaisdell [14] or Kim and Rhee [34].

3.5. Influence of solver settings

3.5.1. Influence of free stream turbulence parameters

The found wingtip flow field and vortex formation may be influenced by the turbulence quantities specified at the inlet boundary. In theory the turbulence level of the freestream flow would influence the boundary layer properties over the wing and thus the formation of the wingtip vortex. To investigate this dependency a simulation has been performed with turbulence quantities that differ from the proposed settings by Spalart and Rumsey [56]; a turbulence viscosity ratio of 0.20144. In this simulation the turbulence viscosity ratio $\frac{\mu_t}{\mu} = 10$. The found lift- and drag coefficients are nearly identical to those found in the 'standard' simulation case. With $C_D = 0.1877$ and $C_L = 0.6601$; respectively a 0.58% and 0.08% difference with respect to the baseline simulation was found. Furthermore the vortex shape, strength and dissipation downstream is identical, as can be seen in figures 3.21 and 3.22. It can therefore be said the proposed turbulence viscosity ratio of 0.20144 can be used, as is done in the 'baseline' case.

3.5.2. Influence of turbulence model

One can say that the choice for a certain turbulence model is (amongst others) determined by the following;

- Applicability to the problem; curvature, sharp pressure and velocity gradients etc. present
- Required accuracy of the solution; to what extend should the solution resemble the real-world problem
- Amount of computational resources available

In this case the Spalart-Allmaras turbulence model with modifications to the source terms was chosen. As shown in the aforementioned results this model is capable of accurately representing the wingtip vortex flow field, to an extent that is acceptable for this study. The velocity and pressure gradients present in the flow are correctly simulated. Furthermore, the quantitative differences between the simulation results and experimental values are small enough. Given the fact that this is a one-equation model this is favourable in terms of required computational resources. For completeness, the popular and seemingly suitable two-equation SST (Shear Stress Transport) $\kappa\omega$ model [41] was also tested. This model is designed for large adverse pressure gradients, as occur in this study. The baseline grid (no. 1) was used. Using this turbulence model, $C_D = 0.1876$ and $C_L = 0.6678$ was found. Compared to the baseline grid with S-A turbulence model this is a difference of 1.1% and 0.56%, a notably larger difference than found using the different free stream properties. Next to this a difference in vortex structure and strength was found downstream of the wing trailing edge. This can clearly be seen in figures 3.21 and 3.22.

One would expect that the use of a two-equation turbulence model would outperform the simpler, one-equation S-A model. However, using the $SST-\kappa\omega$ model the vortex strength dissipates even faster compared to the S-A model, which also under-predicts the vortex strength downstream of the wing. Furthermore, the found vortex structure slightly differs from those found using the S-A model and observed in experimental studies. This behaviour was also observed by Kim and Rhee [34], who found a similar under-prediction of the vortex strength when using the $SST-\kappa\omega$ model.

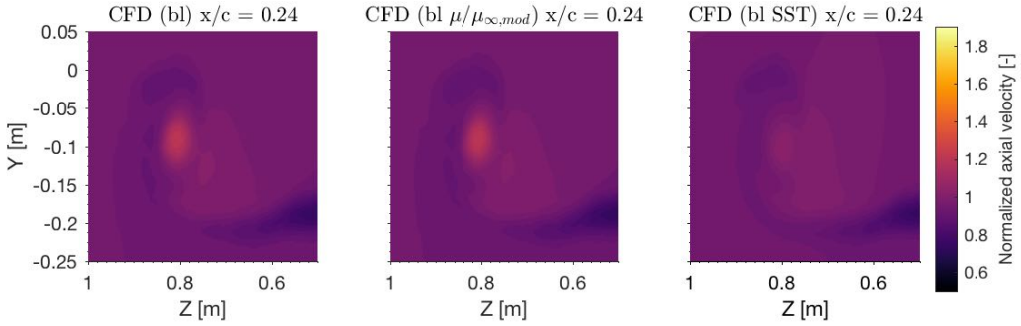

Figure 3.21: CFD S-A, $\frac{\mu_t}{\mu}_{mod}$, $SST-\kappa\omega$ compared. Contour plots of the normalized axial velocities $\frac{u}{U_\infty}$ at $x/c = 0.241$

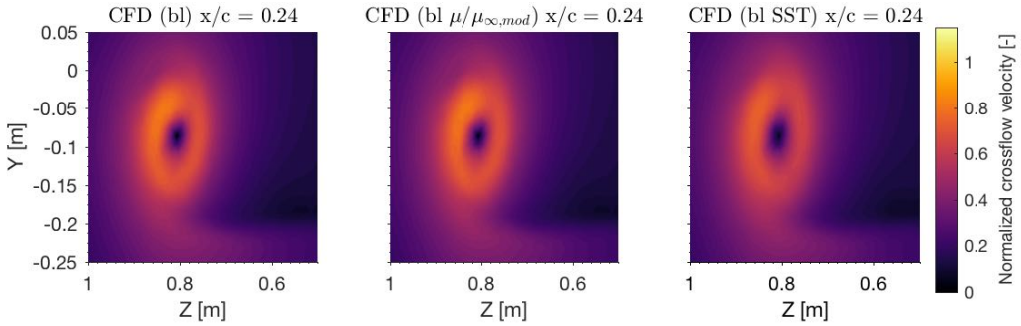

Figure 3.22: CFD S-A, $\frac{\mu_t}{\mu}_{mod}$, $SST-\kappa\omega$ compared. Contour plots of the normalized cross flow velocities $\frac{\sqrt{v^2+w^2}}{U_\infty}$ at $x/c = 0.241$

4

CFD Analysis of the wingtip flow field of baseline wing

Instead of the low aspect-ratio half wing used to investigate the wingtip flow field a realistic wing will be used in the remainder of this research. A real-life flight scenario is investigated in order to get a feeling for the applicability of this tip-mounted propeller concept. In this chapter the CFD analysis of such a scenario and according wing is described. First the used wing design including propeller and spinner is presented in section 4.1. Next the used domain, mesh, boundary conditions and solver settings in CFD (ANSYS Fluent) are described in section 4.2. Wherever applicable similar mesh properties and solver settings as used in the validation study presented in chapter 3 are used here. The results of this simulation setup are described in section 4.3. Finally the selected flow field to be imposed on the propellers to be used throughout the remainder of this research is discussed in section 4.4.

4.1. Baseline wing and spinner geometry

Used as baseline aircraft for NASA's X57 Maxwell [48], the Tecnam P2012 [60] wing was also chosen for this study. The semi-span of this aircraft's wing is $7m$ and the root chord is $2.06m$. The wing geometry used here is slightly simplified. This is justifiable as the goal of this research is to investigate the performance of a wingtip-mounted propeller in a realistic flow field and not to simulate the Tecnam P2012.

Extending from the aft wingtip is the spinner of the propeller. Dimensions of the spinner are based on requirements for the propeller to be used, described in chapter 6.1. As a pusher propeller is investigated a suitable spinner shape was designed. In figure 4.1 an isometric view of the wing including spinner is shown. Please refer to appendix B for an overview of all properties of the baseline wing and spinner design. The rotational plane of the propeller is placed at 0.262 m aft of the wingtip trailing edge.

4.2. CFD Analysis setup - baseline wing

In this section the simulation of the wing with spinner and propeller represented as actuator disk is described. The computational setup and results obtained from this simulation are presented. This will provide insight in the vortex structure originating from this wing. A very brief overview of the used domain, boundary and operating conditions, mesh and solver settings is given, as most parameters are chosen as used in the validation study presented in chapter 3.

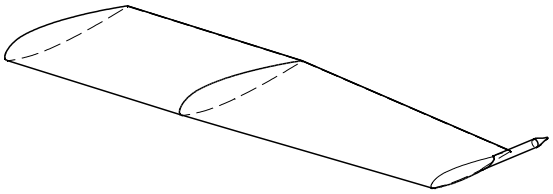

Figure 4.1: Isometric view of the used baseline wing and spinner combination

4.2.1. Domain geometry

A sufficiently large domain was constructed to minimise the influence of boundary interaction effects. In figure 4.2 the used domain is schematically shown. Furthermore, the propeller domain is visible. This is also a refined domain in which the propeller will be placed in a later phase. The propeller domain is subdivided into two parts: the propeller domain and a slipstream domain. Note that the domains are not shown to scale in figure 4.2 - the main dimensions are added for clarity.

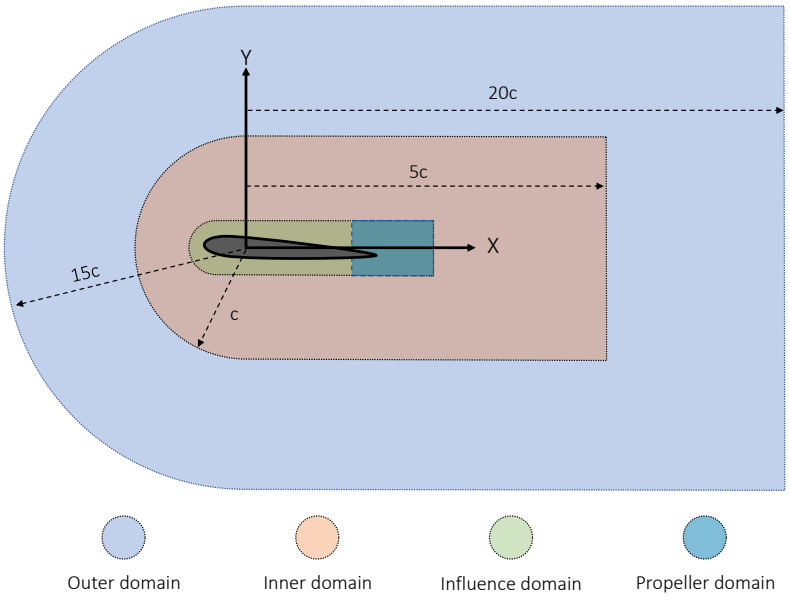

Figure 4.2: A schematic overview of the used domain and subdomains - containing the wing, propeller and refined inner domain. Note that indicated domains are not to scale.

Additionally in appendix B, figure B.1 a three-dimensional view of the implemented domain is presented. The span wise extension of the domains are also visible in figure B.1.

4.2.2. Mesh properties

The mesh used in the validation study of an isolated wing proved to be capable of representing the vortex structure accurately. Therefore similar mesh settings were used for the wing and spinner combination, scaled to the appropriate dimensions of this larger model. A similar average cell size over the wing and spinner surface has been used. The first layer thickness of the inflation layer is specified to obtain $y^+ \approxeq 1$ at the wing surface, to capture the viscous sub-layer. A total of 39 layers was set to capture the full boundary layer of the wing.

4.2.3. Boundary and operating conditions

Different from the isolated wing simulation are the used boundary and operating conditions of this simulation. The cruise speed is assumed to be 80 m/s (±90% of the Tecnam P2012T cruise speed) in combination with a cruise angle of attack of 3 degrees. This leads to a realistic lift coefficient for this wing and aircraft type and thus a realistic induced drag and downwash. The cruise altitude is 10,000 ft (3048 m). Apart from the assumed geometry, the encountered vortex structure and strength would be similar to one found in actual flight on a similar aircraft.

Table 4.1: Boundary and operating conditions specified in the domain of the wing/spinner setup

Parameter	**Symbol**	**Value**	**Unit**
Cruise altitude	h_{cruise}	10,000	ft
Mach number	M_∞	0.2436	[-]
Freestream velocity	V_∞	80	m/s
Wing angle of attack	α_{cr}	3	deg
Chord-based Reynolds number	Re_c	$8.81 \cdot 10^6$	[-]
Static (operating) temperature	$T_{s,\infty}$	268.338	K
Total temperature	T_t	271.523	K
Freestream static pressure	$P_{s,\infty}$	69,682	Pa
Freestream total pressure	$P_{t,\infty}$	72,620	Pa
Freestream density	ρ_∞	0.9046	kg/m^3
Eddy viscosity ratio	$\mu_{t,\infty}/\mu_\infty$	1	[-]

- **Inlet** At the inlet of the domain the static pressure $P_{s,\infty}$ and temperature $T_{s,\infty}$ was specified to match freestream conditions as described at cruise altitude and velocity as described above. The inlet is places at a distance of 15 chord lengths to ensure the wing model has no influence on the domain boundaries. In ANSYS the 'pressure far field' was used to specify this boundary. Freestream turbulence levels are set as listed in table 4.1.
- **Far-field** The far-field of the domain is also set as pressure far-field, simulating the freestream conditions specified. This far-field boundary is placed at a distance of 15 chords from the wing model. Freestream turbulence levels are set as listed in table 4.1.
- **Near-field** The near-field 'walls' of the domain at the root of the wing are modelled to be inviscid walls; as symmetry planes. The effect of a fuselage that would be present in real life is thus neglected.
- **Outlet** At the outlet of the domain the static pressure is set to equal the undisturbed (or freestream) static pressure. In ANSYS this boundary is specified as a 'pressure outlet'. The total temperature T_t is also specified at this boundary. This outlet is placed at 20 chord lengths aft of the wing model.
- **Wing** The surface of the wing model is set as a 'no-slip wall' as the fluid velocity with respect to the wing surface is zero.

4.2.4. Solver settings

All solver settings as used in the validation study described in section 3.2.4 of the previous chapter are also used in this simulation. Again the simple one-equation S-A turbulence model is used.

4.3. Results

In this section the resulting flow field obtained is shortly discussed. Cut planes at various downstream locations have been extracted from CFD, providing insight in the vortex development at the investigated wingtip

geometry. Furthermore a mesh dependency study has been performed, to determine influence of grid properties on the obtained results. Results are concisely presented and discussed as the validity of the used setup was shown in chapter 3.

4.3.1. Vortex build-up: cut planes at various downstream locations

To provide insight in the development of the vortex structure formed at the tip of the baseline wing cut planes at various downstream locations are investigated. Similar to the validation study the normalised axial- and in-plane velocities are discussed. In figures 4.3 to 4.5 contour plots obtained from CFD are shown. These are shown at three different downstream locations: 0.5485c, 0.75c and 1c aft of the wing quarter point. Note that the propeller plane is located at the first downstream location shown (0.5484c aft of the wing quarter point).

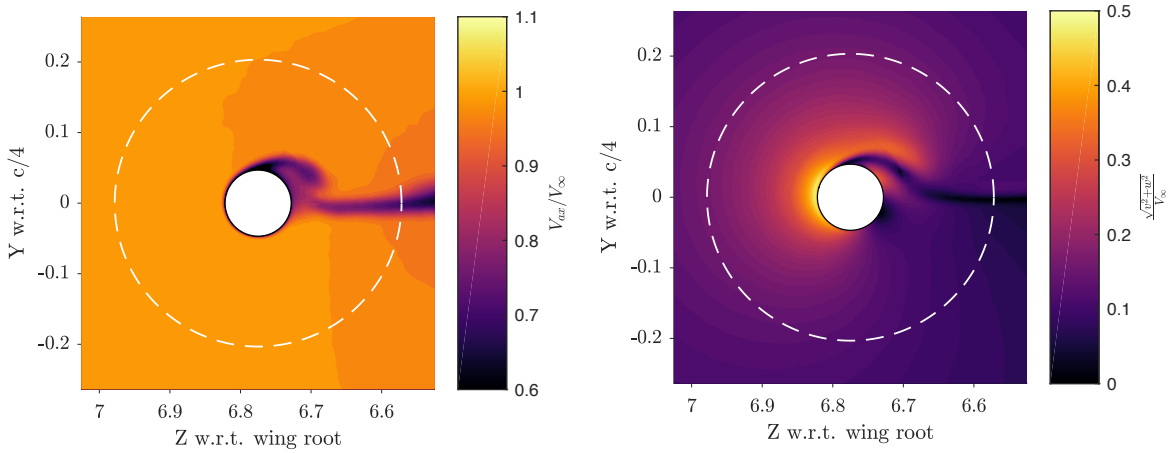

(a) Normalised axial velocity V_{ax}/V_∞ [-]

(b) Normalised in-plane velocities $\frac{\sqrt{v^2+w^2}}{U_\infty}$ [-]

Figure 4.3: Contour plot of axial- and in-plane velocities at 0.5485c aft of the wing quarter chord (the propeller location). The dotted outline indicate the stream tube of the propeller disk.

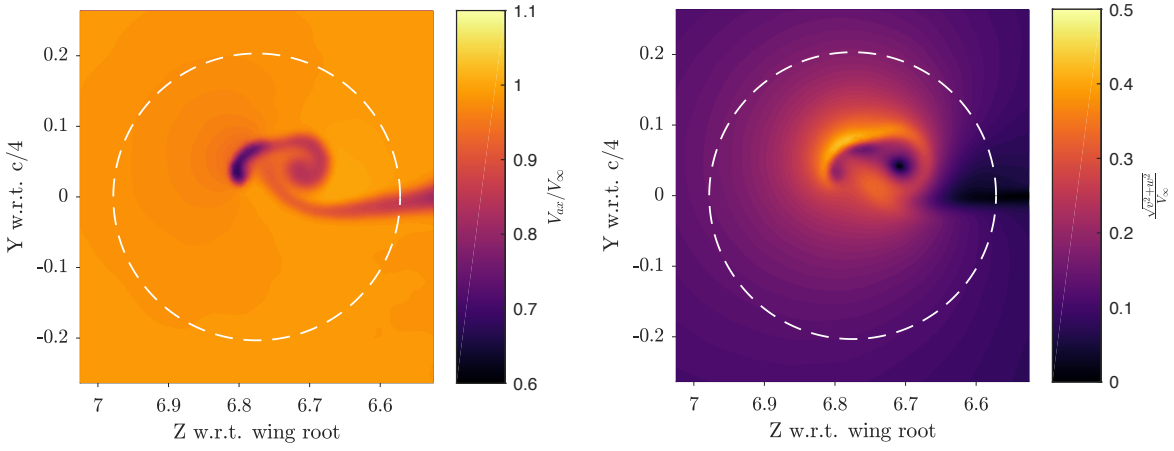

(a) Normalised axial velocity V_{ax}/V_∞ [-]

(b) Normalised in-plane velocities $\frac{\sqrt{v^2+w^2}}{U_\infty}$ [-]

Figure 4.4: Contour plot of axial- and in-plane velocities at 0.75c aft of the wing quarter chord. The dotted outline indicate the stream tube of the propeller disk.

In figures 4.3 to 4.5 the formation and dissipation of the vortex is clearly visible. Notice that the vortex formed here has a lower strength than the one found in the validation study presented in chapter 3. The maximum in-plane (normalised) velocities are found to be in the order of $0.5 \cdot V_\infty$, compared to $0.9 \cdot V_\infty$ found in the validation study. Furthermore, the maximum axial velocities do not exceed $1.05 \cdot V_\infty$, compared to $1.8 \cdot V_\infty$

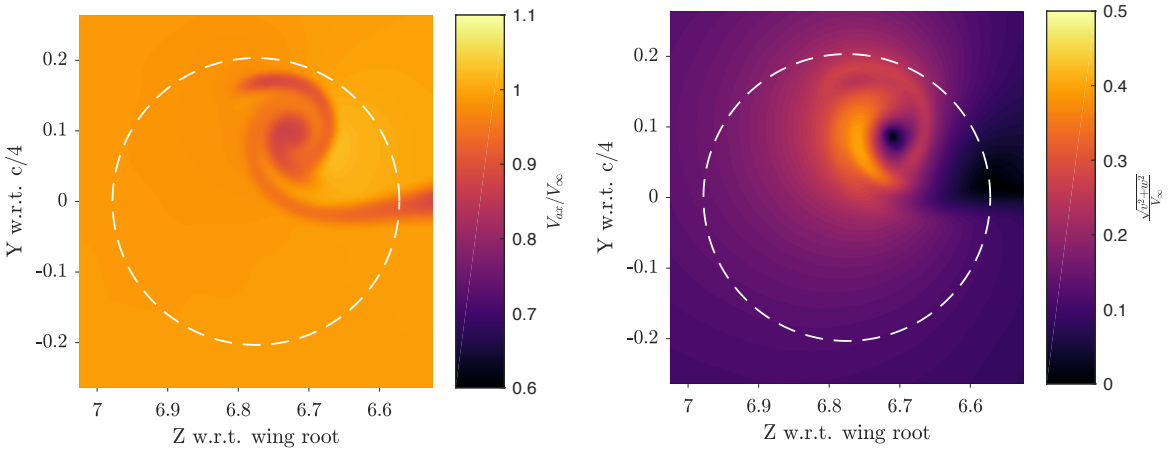

(a) Normalised axial velocity V_{ax}/V_∞ [-]

(b) Normalised in-plane velocities $\frac{\sqrt{v^2+w^2}}{U_\infty}$ [-]

Figure 4.5: Contour plot of axial- and in-plane velocities at 1c aft of the wing quarter chord. The dotted outline indicate the stream tube of the propeller disk.

found in Chow's validation study. This can be explained by a much lower angle of attack (3° vs 10°) and a higher wing aspect ratio of this baseline wing. Nevertheless a significant in-plane and thus tangential flow is present within the provided propeller radius. Regardless of the vortex strength compared to the (extreme) validation study this flow field should provide insight in (propeller) performance improvements to be achieved when placing a propeller at the wingtip.

4.3.2. Mesh dependency study - Grid Convergence Index

As in the wing validation study a mesh dependency study was performed for this CFD model. Four different refinement levels are evaluated, listed in table 4.2. In this table the respective lift- and drag coefficients found for each mesh are also shown. Again a least squares version of the Grid Convergence Index methodology ([50],[20]) has been applied. As no validation data is available for this wing geometry and operating conditions only a discretization error can be determined. This discretization error is listed in table 4.2. This was done using the idealized grid solution ϕ obtained from the CGI method. It is assumed that the model error is equal to the model error determined in section 3.3.1 of the previous chapter as solver settings and grid dimensions are similar and validated.

Table 4.2: Overview of meshes generated for mesh dependency study

Mesh	Refinement	Name	No. of elements	C_L [-]	C_D [-]
3	0.50	Extra Coarse	8,561,478	0.3434	0.1638
2	0.75	Coarse	16,315,794	0.3440	0.1622
1	**1**	**Baseline**	**32,756,863**	**0.3448**	**0.1599**
4	1.20	Fine	51,424,2206	0.3452	0.1585
-	Infinite	Idealised values ϕ	-	0.3459	0.1567
-	-	Discretization error	-	0.3013%	2.042%

In figures 4.6a and 4.6b the least-squares fit of the found C_L and C_D values for different meshes is plotted.

From the CGI and extrapolation values for C_L and C_D with an idealised, infinitely refined mesh are obtained, using the fit of $p = 2$. The values found are 0.3459 and 0.1567 for C_L and C_D respectively. Comparing these values to the used mesh in this case (no. 1), a discretization error can be obtained. The discretization error is found to be 0.3013% and 2.042% for C_L and C_D respectively.

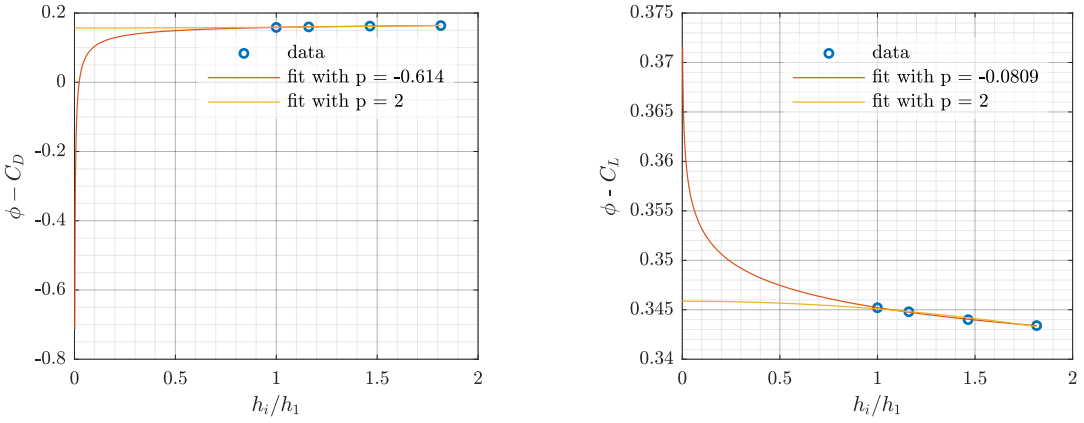

(a) C_D vs. mesh refinement

(b) C_L vs. mesh refinement

Figure 4.6: Least-squares fit of C_L and C_D versus average cell size for the baseline wing.

4.4. Flow field to be imposed on the propeller

In this final section the flow field quantities in which the propeller will be placed is presented. The rotational plane of the propeller is placed at 0.262 m aft of the wingtip trailing edge. At this location the flow properties are extracted from the CFD simulation described previously in this chapter. In figure 4.7a the normalised axial velocities (u/V_∞) at the propeller plane are visualised. At the same location the normalised tangential velocity V_{tan}/V_∞ is shown in figure 4.7b.

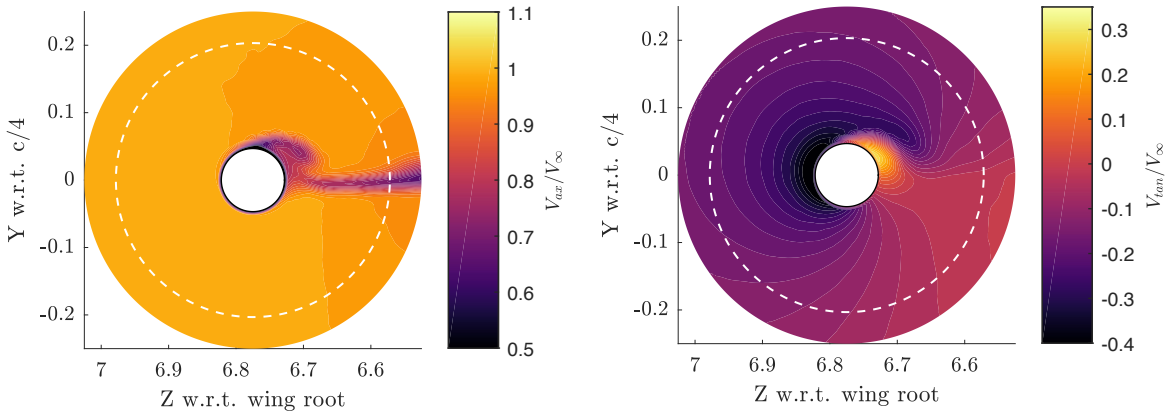

(a) Normalised axial velocity V_{ax}/V_∞ [-] at the propeller plane location

(b) Normalised tangential velocity V_{tan}/V_∞ [-] at the propeller plane location

Figure 4.7: Contour plot of axial- and tangential velocities at the propeller plane, extracted from CFD simulation. Dotted outline indicate the propeller disk.

In figure 4.8a the (normalised) circumferentially averaged tangential velocity at the propeller plane is plotted. Line plots of all imposed velocities on the propeller are shown in figure 4.8b. The tangential velocity ratio is shown: $V_{tan_{circ,av}}/V_{ax_{circ_{av}}}$. Note that this is the ratio of the *local* tangential and *local* axial velocity. Also, the normalised circumferentially averaged tangential velocity profile is shown. Finally, the fraction of axial velocity is shown in figure 4.8b. Positive tangential velocity is defined as outboard *down* as seen from the propeller rotational axis. Thus, outboard upward flow of the wingtip vortex is shown as negative tangential velocity.

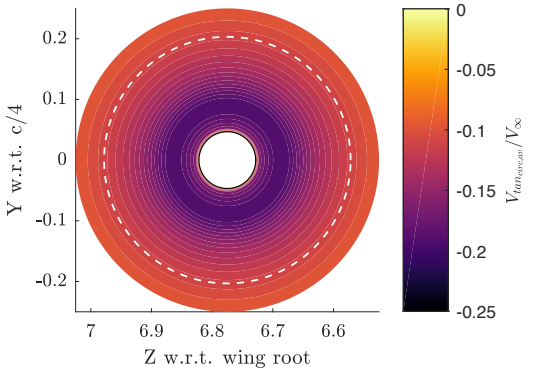

(a) Contour plot of circumferential average of normalised tangential velocities $V_{tan_{circ,av}}/U_\infty$ [-] at the propeller plane location.

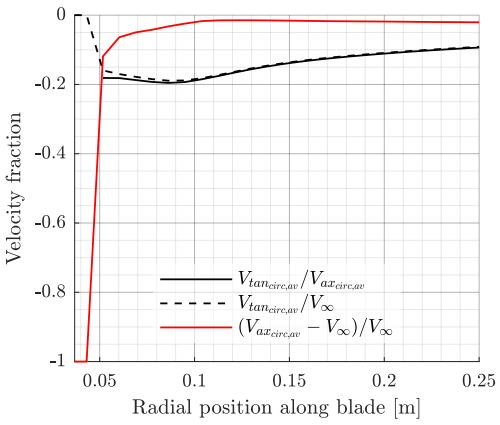

(b) Circumferentially averaged tangential velocity ratio $V_{tan_{circ,av}}/V_{ax_{circ_{av}}}$ [-].

Figure 4.8: Flow field quantities in terms of normalised and circumferentially averaged tangential velocities at the propeller plane, extracted from CFD simulation. Dotted outline indicate the propeller disk.

Placing the propeller in the discussed flow field and subsequent evaluation of its performance will be presented in chapter 6.

4.5. Conclusions of part I

The goals set out for this first part of the research, investigation of the wingtip flow field, have all been reached:

- ☑ Discuss the fundamental principles of wingtip flow fields
- ☑ Select and implement a suitable simulation method for wingtip flow fields
- ☑ Validate the used simulation method with experimental data
- ☑ Describe and simulate a baseline wing model, to which a wingtip-mounted propeller can be added in a later part

The fundamental principles of wingtip flow fields have been discussed, which provided the needed insight in the complexity of these flow fields. Furthermore, various influencing factors in the formation and behaviour of wingtip vortices were discussed. Next, a CFD analysis was set up to determine the required turbulence model, grid properties and computational domain. This setup was validated by means of an experimental study by Chow [13]. It is concluded that the set up CFD analysis enables accurate representation of the wingtip vortices. Next, a wing geometry of a representative general aviation aircraft (Tecnam P2012) was selected. This provides a real-life use case for the eventual quantification of wingtip-mounted propeller performance improvements. The respective wingtip flow field was simulated using the validated CFD setup. A realistic wingtip flow field and wing model is now available, to be used as incoming flow properties for a propeller. In the next part of this research a propeller aerodynamic analysis tool will be set up, enabling optimisation of the propeller geometry for the non-uniform flow field it is immersed in.

II

Investigation and modelling of (pusher) propellers

In the second part of this research the (isolated) propeller is investigated. The required propeller analysis and optimisation tools will be presented in this part. Goals set out for this part are:

- ☐ Describe the fundamental principles of propeller performance
- ☐ Build an analysis tool capable of analysing and optimising an arbitrary propeller geometry given a (non-) uniform inflow field
- ☐ Validate this analysis tool using experimental and CFD results
- ☐ Implement a (validated) CFD simulation to investigate isolated propellers

5

Propeller theory and modelling

In this chapter the modelling and fundamentals of the (isolated) propeller will be discussed. First, the working principle of propellers is explained in section 5.1 to gain a proper understanding of these propulsive devices. Next the different possible analysis methods are reviewed in section 5.2 and a suitable analysis method is chosen.

5.1. Working principle of propellers

The propeller of an aircraft has a single function: converting rotational energy into thrust. To do this, propellers of various shapes and matching efficiencies exist. Propeller performance and characteristics are often described by a few universally used parameters. Often used parameters are, in no particular order:

- **Propulsive power:** The power delivered by the propeller at a given rotational and free stream velocity. This is a measure of the (rate) of useful work done by the propeller.
- **Propulsive efficiency:** The fraction of power delivered (shaft power, P_s) that is actually converted to propulsive power, i.e. the efficiency of the propeller. As defined here the efficiency is always less than the ideal 100 percent for propellers with axial inflow. This is because of the loss of energy in the slipstream, frictional losses, pressure drag at the blades and losses due to compressibility. However, propellers with tangential inflow can theoretically have an efficiency higher than 100 percent according to this definition of propulsive efficiency.
- **Thrust:** This is essentially the change in momentum due to the pressure difference in front and aft of the propeller; obviously resulting in the force that 'drags' or 'pulls' an aircraft forward.

Note that all are highly dependent on the propeller geometry and operating conditions. Specific performance parameters used are the power coefficient C_P, thrust coefficient C_T and advance ratio J of the propeller:

$$C_P \equiv \frac{P_s}{\rho_\infty n^3 D_p^5} \tag{5.1}$$

$$C_T \equiv \frac{T_p}{\rho_\infty n^2 D_p^4} \tag{5.2}$$

The loading of the propeller blades is often described using a non-dimensional parameter; the advance ratio J. A high blade loading is denoted by a low advance ratio and vice versa.

$$J \equiv \frac{V_\infty}{nD_P} \tag{5.3}$$

In these equations D_p is the propeller diameter, n is the rotational speed of the propeller and ρ_∞ is the free stream air density. Finally the propeller efficiency can be expressed as follows:

$$\eta_{prop} = \frac{2}{1 + \frac{u_e}{u_0}} \tag{5.4}$$

5.2. Selection of a propeller analysis method

Similar to modelling the wingtip and the associated vortices, it would be preferably to model the propeller flow at high fidelity and accuracy. However, the final research goal is to optimize the propeller shape, geometry and placement with respect to the main wing. The use of RANS-based methods would be too computationally expensive for use in optimization routines and thus a lower-fidelity tool is needed. Note that RANS-based methods are perfectly suitable for the validation of the calculated propeller performance and combined, optimized wing-propeller configuration.

Widely used lower-fidelity tools are based on the Actuator Disk Theory (ADT), or momentum theory, and Blade Element Theory (BEM). Simply stated, in ADT one focuses on the motion of the fluid and the forces exerted by the propeller on the flow. Thus the actual shape of the propeller does not matter and cannot be determined. In contrast, one does focus on the aerodynamic characteristics and thus geometry of the propeller blade sections when using BEM. Both methods will be explained in the following sections.

5.2.1. Actuator Disk Theory

The actuator disk theory (ADT), also referred to as the momentum theory, is perhaps the most basic representation of a propeller. It was described by Rankine as early as 1865, and still serves as a great explanation to show why a propeller generates thrust. In this theory the propeller is modelled as an infinitely thin actuator disk which exerts a distributed force on the flow field. The surface area of the actuator disk is identical to the swept area of the propeller blades. One defines a stream tube and control volume, and basic integral momentum theory can be applied. Refer to figure 5.1 for a schematic overview of the described control volume and pressure jump across the disc. For a full derivation of the actuator disk theory, refer to Ruijgrok [51].

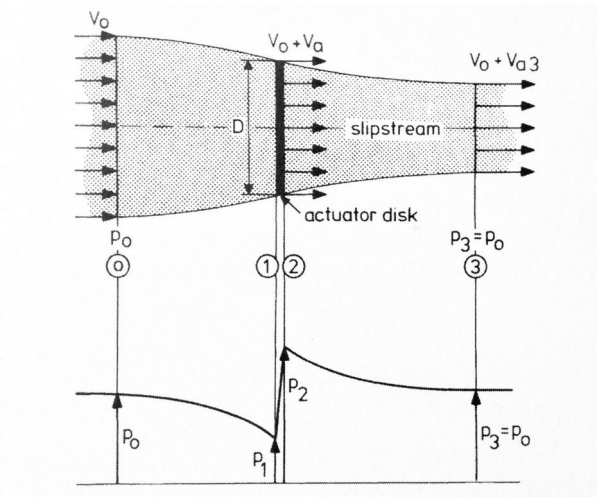

Figure 5.1: A control volume and stream-tube of an arbitrary propeller modelled as an actuator disk, including the pressure across the disk [51]

A pressure jump is created across the disk because of the momentum inserted into the flow. By integrating

the pressure over the entire disk the thrust can be found. The following assumptions are made:

- The flow is incompressible, irrotational, inviscid and steady
- A uniform pressure and velocity distribution exists (at each cross section of the stream tube)
- The effect of separate blades present is neglected (i.e. a single solid disk is assumed)

These assumptions obviously limit the applicability of this method, especially if one wants to optimize the propeller geometry. An extended and more elegant version of the actuator disk theory is presented in the work of Delano and Crigler [16]. In their work the simple momentum theory as described above was extended to include the effects of compressibility. Note that also Delano and Crigler assume a uniform, one-dimensional inflow over the entire actuator disk.

In general, the upside of ADT is the speed and simplicity, allowing for a fast indication of the propeller performance. However, a more refined method is needed in order to be able to optimize the actual geometry of the propeller, especially one with non-uniform inflow.

5.2.2. Blade Elements Models

Blade element tools have been used for the modelling of propellers ever since the early 1920s, and are still widely used for the optimization of propellers. In blade element models one divides a propeller blade into small segments (the elements dr), assumed to behave similar to a two-dimensional wing. Refer to figure 5.2 for the description of a blade element and the forces acting on this element.

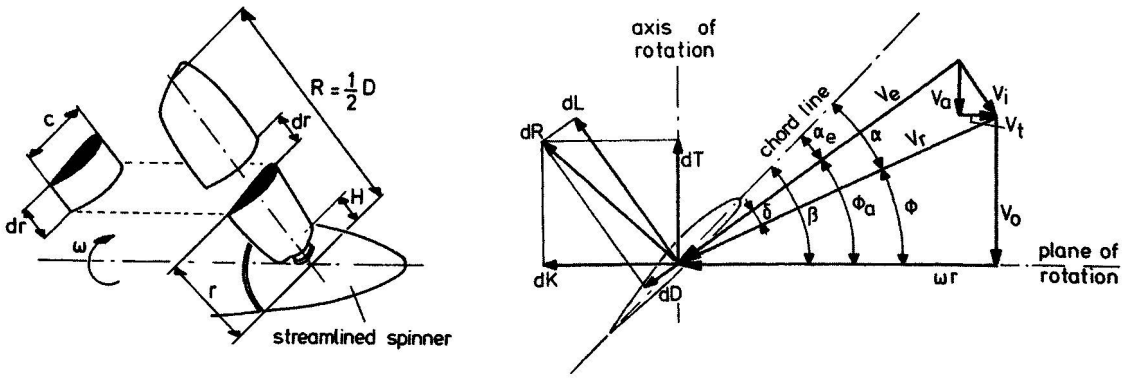

Figure 5.2: A blade element with the forces acting on it and associated velocities (from Ruijgrok [51])

For each element the lift- and drag coefficients are determined as function of the angle of attack, Reynolds number and finally Mach number. In order to determine these three parameters, the flight velocity, rotational velocity of the propeller blade and propeller induced velocity must be known. Both the flight velocity and rotational velocity are known, but the induced velocity has to be calculated using an additional model alongside the blade-element model. Most used are the momentum and lifting-line models. These will be briefly described in the following, along with their limitations. A comparison of the most used variants of these models can be found in the work of Gur and Rosen [26]. Another possibility would be to obtain the induced velocities directly from the CFD simulation, which is essentially a highly refined momentum model.

Momentum model

The momentum model is essentially a combination of the actuator disk theory and the general blade element model. Again, the propeller is represented as an actuator disk that has the swept area of the propeller. This disk is infinitely thin and can exert axial and circumferential momentum on the flow that passes through it. The disk is then divided into concentric annuli (rings that have the same midpoint as the centre of the disk).

As with ADT, a pressure jump is created across the disk because of the momentum inserted into the flow. Integrating these pressure jumps over the entire disk gives the total thrust.

The combined solution of the blade-element/general-momentum model starts by assuming an initial induced velocity distribution along the blade. Then, the thrust and torque distributions along the blades are calculated by using the blade-element model. This is followed by calculating the induced velocity using the general-momentum model. This scheme is repeated iteratively until convergence.

A limit of this model is, as with the classical momentum theory, that flow phenomena are averaged over the concentric annuli. This essentially means that an infinite number of blades is assumed to be present. Goldstein [24] came up with a correction factor - $\kappa(r)$, a function of the number of blades, the radial coordinate and local inflow angle. Correction is implemented by multiplying all induced velocities by $\kappa(r)$. Another solution to the averaging problem was presented by McCormick [40], proposing a correction to account for the chancing cross-sectional angle of attack.

Lifting-Line model

A well-known method used in aerodynamic analysis is the lifting-line model originally developed by Prandtl. The wing (section), or propeller in this case, is represented by a vortex filament at the quarter-chord line of the wing. Since the circulation Γ_x varies along the wing the bound vortices vary in strength, creating trailing vortices and forming the wake behind the wing. In the case of (ideal) propellers, the vortex sheets of each blade move downstream of the propeller in as rigid screw surfaces, shown in figure 5.3. With this knowledge, the wake geometry and properties can be determined.

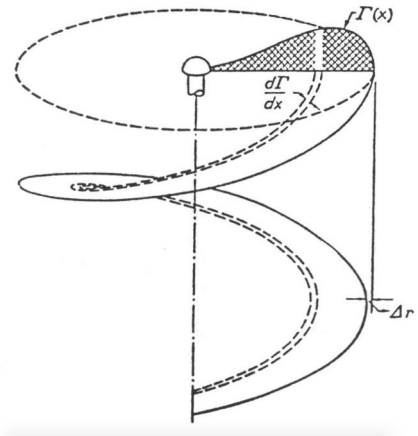

Figure 5.3: The screw-like vortex lines forming the wake of an ideal propeller [61]

Theodorsen first showed that the properties of a (ideal) propeller can be completely derived from the far wake properties [61]. This could be done using either a free or fixed wake model. In the former, the actual geometry is calculated based on the local resulting velocities. This requires an iterative solution process, since the propeller performance is derived from the wake geometry, which in turn depends on the propeller performance. The second option is to use a so-called fixed wake model, where the wake geometry is prescribed based on certain parameters. For example, it can be assumed that the wake of a propeller is shaped in a helical manner with constant pitch and radius. After defining the wake the induced velocities can be calculated using e.g. the Biot-Savart law. Please refer to the work of Theodorsen [61] for an extensive explanation of this process.

5.3. XRotor: a suitable propeller analysis tool

In the remainder of this research the widely used BEM-tool called XROTOR, an open-source code by Drela and Youngren [18] will be used for lower-order propeller analysis. XROTOR is a numerical, iterative BEM method

that can design and analyse rotor geometries. It is largely based on the works of Betz [8], Theodorsen [61], Goldstein [24] and Larrabee [37]. A graded momentum formulation, fixed wake and free wake method can be used. For an extensive overview of these different vortex theories, please refer to the work of Zondervan [65]. One can define a radially varying incoming flow in both axial and tangential direction in XRotor. This can be done by simulating the propeller as if it were used in tandem configuration, with a propeller upstream and thus experiencing an incoming slipstream [18]. This functionality was also used in the work of van Arnhem [5]. In conclusion XRotor is a suitable tool for the remainder of this thesis work because of the following capabilities:

- Any feasible propeller geometry can be specified, in terms of twist, chord and profile variations along the blade.
- Support for input of radially varying a non-uniform inflow profile in both axial and tangential direction.
- The tool is proven and validated.
- Computational time for single analysis should be in the order of seconds, to allow for inclusion in an optimisation routine.
- Results are consistent and offer sufficient significant digits in the output. This is required for inclusion in an optimisation routine, enabling the use of a gradient-based optimisation tool.
- Local aerodynamic performance of the blade elements can be specified or calculated.
- Compressibility effects are taken into account.
- Can be controlled from a MATLAB environment.

The implementation of XRotor in the full analysis and optimisation tool will be explained in the following chapter.

6

Propeller analysis and optimisation routine: PROPR

The theoretical framework needed to analyse the performance of a propeller was presented in the previous chapter. In this chapter the actual analysis procedure built will be discussed. The presented theory is implemented into a practical analysis tool, called *PROPR*. An overview of the baseline propeller geometry to be used is listed in section 6.1. Next an overview of *PROPR* will be presented in section 6.2. The setup, assumptions made and resulting limitations are discussed. Then, the built tool is validated using multiple wind tunnel results of the XPROP at two different operating conditions. Finally, in section 6.4 the implementation of a propeller optimisation routine is presented. This tool is designed specifically with non-uniform inflow in mind, allowing optimisation of the propeller geometry when placed in such a flow field.

6.1. Baseline propeller geometry - XPROP propeller

Throughout this complete research a single baseline propeller is selected: the XPROP propeller. This propeller has been used in a multitude of research works within Delft University of Technology. Therefore extensive validation and simulation data is available from wind tunnel experiments and previous work. In table 6.1 the main geometrical properties of the XPROP propeller are listed.

Note that the propeller centre axis is assumed to be at $0.3c$. This has no influence on the final calculations using XRotor as no rake or sweep is present in this propeller's geometry.

Table 6.1: Geometry definitions of the baseline XPROP propeller

Parameter	**Symbol**	**Value**	**Unit**
Number of blades	Z	6	[-]
Blade radius	R	0.2032	m
Hub radius	R_{hub}	0.0468	m
Blade rake	-	0	deg
Sweep angle	-	0	deg
Propeller Centre Axis	PCA	0.3	$1/c$

6.2. Overview of the propeller analysis tool: PROPR

In this section an overview of the built propeller analysis tool called *PROPR* is presented. *PROPR* is written in the MATLAB environment. A multitude of custom functions were written by the author and two external programs (XRotor and XFoil) are controlled from *PROPR*. The tool is designed to be used either stand-alone or integrated into an optimisation routine. A simplified program was written by Sinnige [53], later extended by van Arnhem [5] - called *N-XROTOR*. Their work served as a great foundation for the development of *PROPR*.

Fundamentally, *PROPR* consists of four main parts which are normally executed in the order as listed below. These parts are: defining the incoming flow field and operating conditions, calculation of sectional airfoil performance, calculate the total rotor performance and finally perform post-processing of the output obtained in step 3. In figure 6.1 a functional flow diagram of *PROPR* is provided.

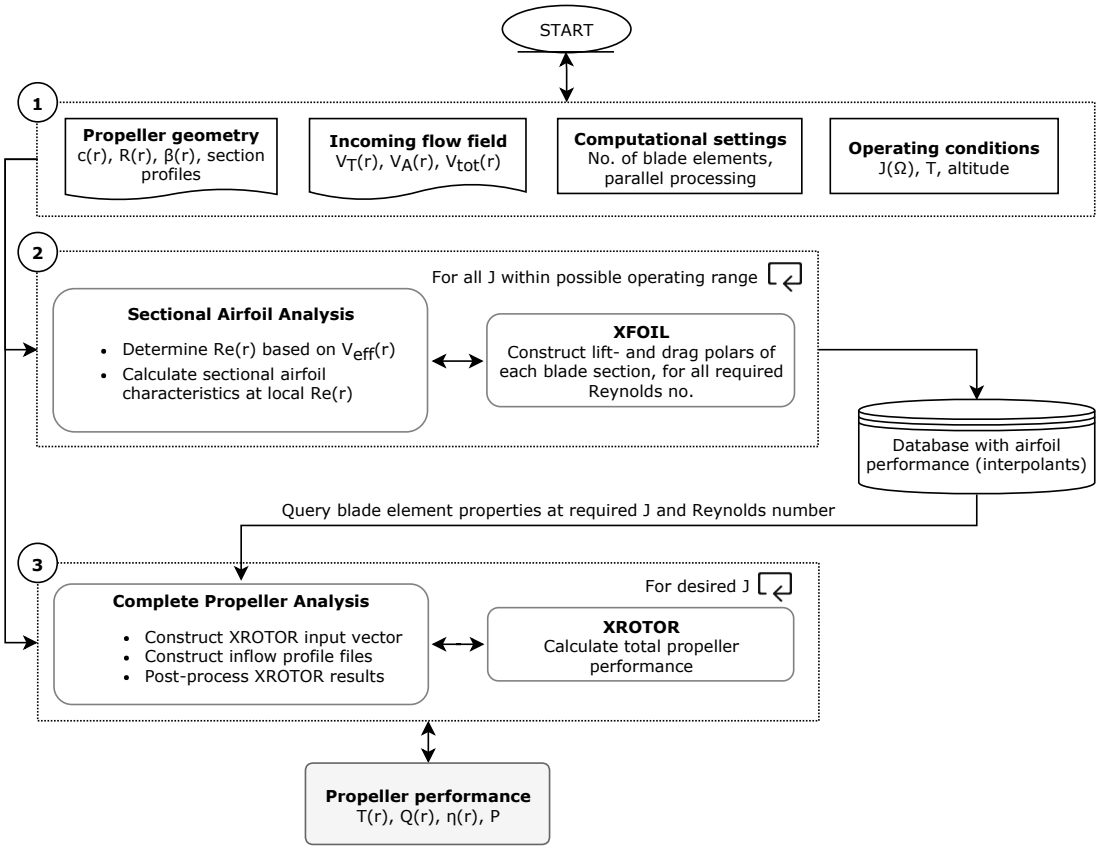

Figure 6.1: A functional overview of the propeller modelling tool *PROPR*.

The detailed implementation providing insight in the assumptions and simplifications made is presented next.

6.2.1. XRotor implementation and simplifications in the inflow

The propeller performance analysis is performed using *XRotor*. The main assumptions and implementation steps are listed below, in no particular order.

- **Rotor geometry:** The rotor geometry is defined by 25 blade elements along the blade span. For each element the local chord length fraction c/R, location along the blade r/R, blade pitch β, airfoil coordinates is provided.

- **Blade element performance:** The blade element aerodynamic performance is defined at 20 stations, as this is the maximum that XROTOR can process. Performance of intermediate stations are interpolated within XRotor. The aerodynamic performance is expressed in the parameters as listed in table 6.2. Within XRotor the blade is represented as 60 discrete stations used to calculate induced velocities.
- **Incoming velocity profile:** The incoming velocity profile is circumferentially averaged and provided in terms of axial and tangential velocity magnitude, both as a function of radius along the blade. This is implemented using the slipstream capabilities built into XRotor, where one can model propellers in tandem configuration. Although large gradients in circumferential direction are present in the wing-tip flow field , XRotor only supports incoming velocity profiles as a function of blade radius. The effect of this simplification is explored in chapter 7.
- **Wall velocity:** Because of a no slip condition at the wall of the propeller hub the actual velocity would be $V_{wall} = 0\ m/s$. However, XRotor can only process non-zero velocities at the very root of the propeller. Thus a finite value for the velocity at the hub wall is assumed, $V_{wall} = 0.01\ m/s$. The effect of this assumption is assumed to be negligible.
- **Wake modelling:** A semi-rigid wake model is used in XRotor. As explained in section 5.2.2, the direction of the vortex sheet originating from the lifting line has to be determined in order to calculate the induced velocities along the propeller blade. XRotor does not support a so-called free wake model, in which not only the induced velocities are taken into account but also the wake contraction and roll-up. As noted by van Arnhem [5] amongst others, the assumption of a semi-rigid wake has little to no impact on the found propeller performance.
- **Compressibility effects (lift):** XRotor uses the standard Prandtl-Glauert correction to account for compressibility effects occurring at higher Mach numbers, shown in equation 6.1.

$$C_{l,c} = \frac{C_l}{\sqrt{(1-M^2)}} \tag{6.1}$$

- **Compressibility effects (drag):** In XRotor the drag components for each blade element are also corrected for compressibility effects occurring. For the unstalled region, C_D has a quadratic dependence on the lift coefficient. A power-law dependency of the actual Reynolds number is used. Finally, a drag rise model representative for NACA airfoils is used. In equation 6.2 all described terms are combined.

$$C_D = \left(C_{D_0} + \frac{dc_d}{d(c_l)^2} \cdot \left(C_{L_0} - C_L\right)^2\right)\left(\frac{Re}{Re_{ref}}\right)^f + k \cdot (M - M_{crit})^n \tag{6.2}$$

  An exponent $f = -0.5$ is advised by Drela for the Reynolds regime under investigation in the current research. It is of the essence to properly determine the incoming Reynolds number Re_{ref}, to minimise the use of this empirical estimate. This implementation of drag estimation does influence the found propeller performance, especially in the higher Mach regime.
- **Freestream flow properties assumed:** At the propeller location the freestream pressure, density and turbulence intensity are used. Furthermore, turbulence intensity is constant along the blade radii.

6.2.2. Calculation of blade element aerodynamic properties

In XROTOR one must define the (2D) blade element aerodynamic properties specified in table 6.2. These properties can be calculated using a multitude of tools. To select a suitable tool a number of requirements are set:

Table 6.2: Sectional airfoil properties used as input for XROTOR

Symbol	Parameter	Unit	Determined by
Re_{ref}	Reynolds number at which drag coefficient is determined	[-]	Inflow profile
$c_{l,max}$	Maximum lift coefficient	[-]	XFOIL
$c_{l,min}$	Minimum lift coefficient	[-]	XFOIL
$c_{l,\alpha}$	Lift curve slope	[1/rad]	XFOIL
$c_{l_\alpha,stall}$	Lift curve slope beyond stall	[1/rad]	XFOIL
α_0	Angle of attack at $c_l = 0$	[deg]	XFOIL
$\delta c_{l,stall}$	Lift coefficient increment to stall - $c_{l,max} - c_{l,non-linear}$	[-]	XFOIL
$c_{d,min}$	Minimum drag coefficient	[-]	XFOIL
$c_{l,0}$	Lift coefficient at $c_{d,min}$	[-]	XFOIL
$\frac{dc_d}{d(c_l)^2}$	Derivative of drag coefficient to square of lift coefficient	[-]	XFOIL
M_{crit}	Critical Mach number	[-]	User
f	Exponent used in drag determination - Reynolds number scaling	[-]	User

- Because of the large number of blade sections to be analysed at different operating conditions, computational time for a single blade element should be in the order of seconds.
- Any airfoil geometry can be loaded from an external file or defined.
- Stall behaviour is included.
- The turbulence intensity of the incoming flow can be specified.
- The tool can be incorporated or executed from a MATLAB environment, without intervention of the user.
- The tool is proven and validated.

A widely used airfoil analysis tool meeting the above requirements is Drela's open-source XFoil [18], the creator of XRotor. For a given range of angle of attack α the airfoil performance in terms of lift- and drag coefficients are obtained. Although XFoil is an excellent and proven tool a few input an post-processing steps were added to improve the accuracy of the analysis in context of a propeller blade element. In the following these are discussed.

- **Effective velocity:** As a blade element is considered, the local velocity over the airfoil depends not only on the freestream velocity. Due to the blade rotation also the rotational velocity Ω and span-wise location of the blade element r/R define the effective velocity experienced by the blade. This can be estimated using equation 6.3. Note that the induced velocities are not included in this effective velocity as these are unknown prior to the complete rotor analysis.

$$V_{eff}(r) \approx \sqrt{V_a(r)^2 + (\Omega R(r))^2} \tag{6.3}$$

- **Local Reynolds number:** Airfoil data is computed at a Mach number of $M = 0$ and the local experienced Reynolds number based on the local chord length $c(r)$ and $V_{eff}(r)$ as explained above. In XRotor compressibility effects are included. Note that this local estimate of Reynolds aids in minimising the empirical estimate of drag coefficient shown in equation 6.2, as the ratio between the actual and estimated Reynolds number is close to one. Furthermore, the critical Mach number is set to be $M_{crit} = 0.75$ for the entire blade.
- **Turbulent boundary layer:** A fully turbulent boundary layer is assumed to be present, thus transition over the airfoil occurs close to the leading edge. This is implemented by defining $N_{crit} = 0.5$ in XFoil. This N is the critical amplification factor in the e^N method by van Ingen [31], used in XFoil to predict transition from

laminar to a turbulent boundary layer. The motivation for this assumption is two-fold. Primarily, all CFD simulations in this research are computed with a fully turbulent boundary layer. Results obtained from PROPR and CFD simulations are therefore more comparable. Secondly XFoil tends to be more stable and converges more often at the described $N_{crit} = 0.5$.

- **Convergence aids in XFoil:** If XFoil did not converge interpolation is done using four adjacent Reynolds numbers. The airfoil is analysed for two Reynolds numbers 10 points higher than the original Reynolds number, and 10 points lower. Only when this interpolation also yields non-convergence, the particular operating condition is rejected.
- **3D lift-correction:** Due to centrifugal and Coriolis forces present, the non-linear part of the lift curve of a 2D airfoil section on a propeller is under-predicted. When separated flow occurs over the blade the local chord-wise pressure gradient is negligible. Thus, the boundary layer is stabilised primarily because of the Coriolis force, thus a higher lift coefficient can be achieved compared to a two-dimensional airfoil. Various empirical correction models exist to account for this. An example is the work of Snel [28], a comparison of multiple methods is presented in the work of Bak [6]. In the current research the correction proposed by Snel is implemented, described in equation 6.4. In this equation $C_{l_{lin}}$ is the inviscid lift coefficient, obtained from extrapolating the linear lift curve at the desired angle of attack. The lift coefficient obtained from XFoil without any correction is denoted by $C_{l_{2D}}$. This correction is dependent on local chord length, expressed as a chord fraction here by $\frac{c}{R}$. Using this method one obtains the lift coefficient corrected for the three-dimensional case: $C_{l_{3D}}$.

$$C_{l_{3D}} = C_{l_{2D}} + 3 \cdot \left(\frac{c}{R}\right)^2 \left(C_{l_{lin}} - C_{l_{2D}}\right) \tag{6.4}$$

- **Interpolant for airfoil properties:** For all required aerodynamic performance properties listed in table 6.2 an interpolant is built by generating a fit through the entire operating range for a given aerodynamic variable. The required aerodynamic properties are now a function of Reynolds number and can be queried as such when analysing the rotor at a given operating condition. This also eliminates the need for storage of all XFoil output.

As an example the lift curve of an arbitrary blade element is shown in figure 6.2a, along with identified blade element properties to be used in XRotor. The resulting maximum lift coefficient as function of Reynolds number for the same given element and corresponding fit is shown in figure 6.2b.

This fitting quality is exemplary for the entire blade and all properties evaluated.

6.3. Validation for uniform inflow of the XPROP propeller

In this section the results obtained using the PROPR tool are validated using two different experimental studies:

- 'Shoptest' of the XPROP propeller, performed by NLR.
- XPROP analysis at the Open Jet Facility of Delft University of Technology, performed by Tomas Sinnige.

In table 6.3 the operating conditions and settings are listed for both experiments. Note that in the first study (Shoptest) the advance ratio was varied by variation of the freestream velocity, and a constant rotational velocity. In the second study (OJF), the opposite was done.

In the following a short comparison between the experimental results and those obtained from *PROPR* is presented. For a blade pitch angle $\beta_{0.7R} = 30°$ the resulting torque, thrust and power coefficients are shown.

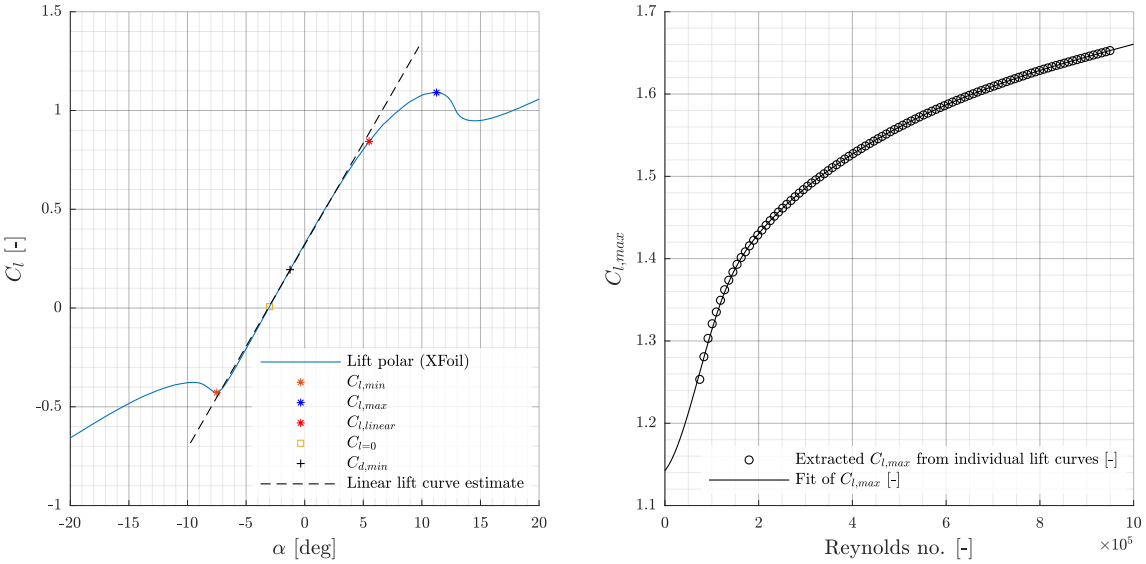

(a) α vs C_l (b) Reynolds no. [-] vs $C_{l,max}$

Figure 6.2: Example of blade element ($r \approx 0.4R$) properties found on original lift curve and corresponding fit of $C_{l,max}$ for range of Reynolds numbers.

Table 6.3: Operating parameters of two validation studies used in PROPR validation.

Symbol	Parameter	Shoptest XPROP	OJF XPROP	Unit
V_∞	Freestream velocity	40 - 101	30	m/s
P_∞	Freestream pressure	$1.0124 \cdot 10^5$	$1.0146 \cdot 10^5$	Pa
ρ_∞	Freestream density	1.225	1.1743	kg/m^3
T_{atm}	Freestream temperature	288.15	300.88	K
Ω	Rotational velocities	10000	2900 - 8850	rpm
J	Advance ratios	0.5 - 1.5	0.55 - 1.5	[-]
$\beta_{0.7R}$	Blade pitch	25 - 35	30	deg

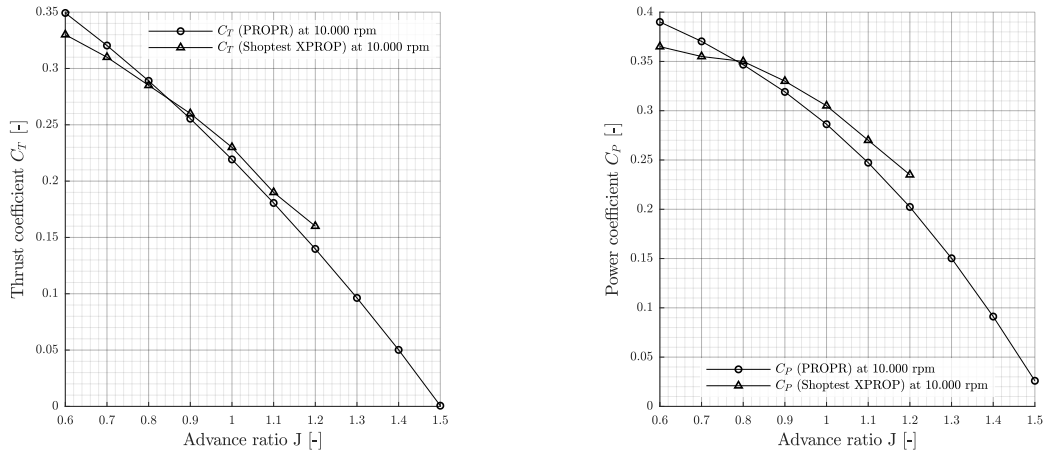

(a) C_T vs J (b) C_P vs J

Figure 6.3: Comparison of XPROP performance - Shoptest results and *PROPR* for $\Omega = 10000 rpm$ and $\beta_{0.7R} = 30°$

In figure 6.3 the thrust- and power coefficients for a range of advance ratios of the XPROP propeller is shown

for both the 'Shoptest' and *PROPR*.

In figure 6.4 the performance characteristics of the XPROP propeller obtained in the OJF and *PROPR* is shown. Note that thrust- and torque coefficients are shown here, again with $\beta_{0.7R} = 30°$. For completeness, results from *PROPR* without 3D-correction as proposed by Snel are also included. However, the propeller does not operate at C_l-values that are higher than $C_{l,linear}$ -values. Thus no 3D-correction is applied in this case.

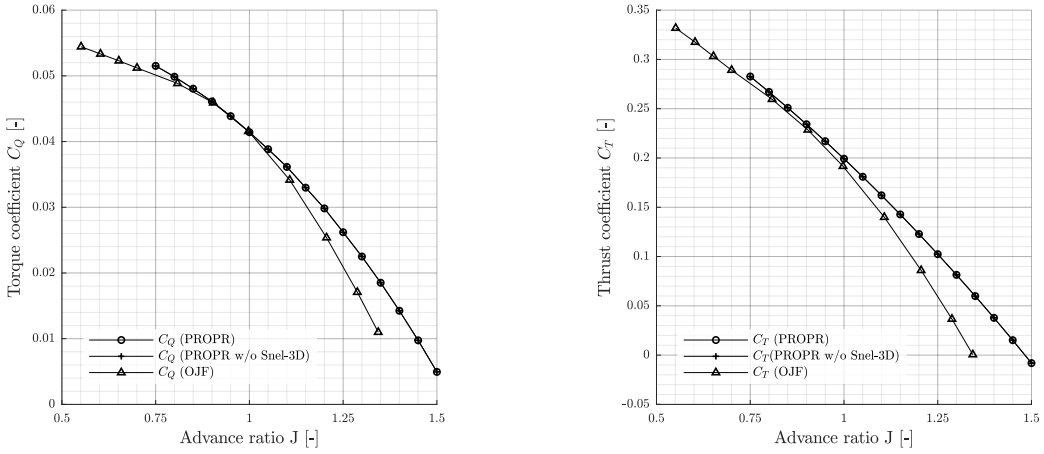

(a) C_Q vs J (b) C_T vs J

Figure 6.4: Comparison of XPROP performance - OJF results and *PROPR* for $V_\infty = 30$ m/s and $\beta_{0.7R} = 30°$

The results obtained from *PROPR* are in good accordance with experimental results shown in figures 6.3 and 6.4. At advance ratios of $0.8 < J < 1.2$ the found torque-, thrust- and power coefficients in *PROPR* are within 15% deviation from the both wind tunnel results. The found differences are in correspondence with those found by other authors ([5], [53]). The moderate advance ratios ($0.8 < J < 1.2$) will also be of interest when optimising the propeller geometry and operating conditions. Thus, *PROPR* can be assumed to provide the user with accurate results given these geometries and advance ratios.

6.4. Optimisation setup

PROPR is integrated in an optimisation routine written in MATLAB. This optimisation routine is built to find the optimal propeller geometry leading to minimum power requirement when placed in a given flow field. This is the first step in quantifying the possible performance benefits when placing a propeller aft of the wingtip. In this section the methodology, resulting setup and obtained results are discussed.

6.4.1. Optimisation methodology and objective function

First and foremost, the objective function used is defined in equation 6.5 below. The minimisation problem is subject to both non-linear equality and inequality constraints: c_{eq} and c_{in} respectively.

$$\min_x P(x) \text{ such that } \begin{cases} c_{eq}(x) = 0 \\ c_{in}(x) \leq 0 \\ lb \leq x \leq ub \end{cases} \tag{6.5}$$

Simply put, this means that a geometry must be found that, when placed in the given flow field, has the lowest possible power requirements whilst satisfying the imposed constraints. These constraints are discussed in the following section. The optimisation routine used written in MATLAB, using the built-in *fmincon* solver. This solver is a gradient-based non-linear programming solver and is widely used. Within *fmincon* one

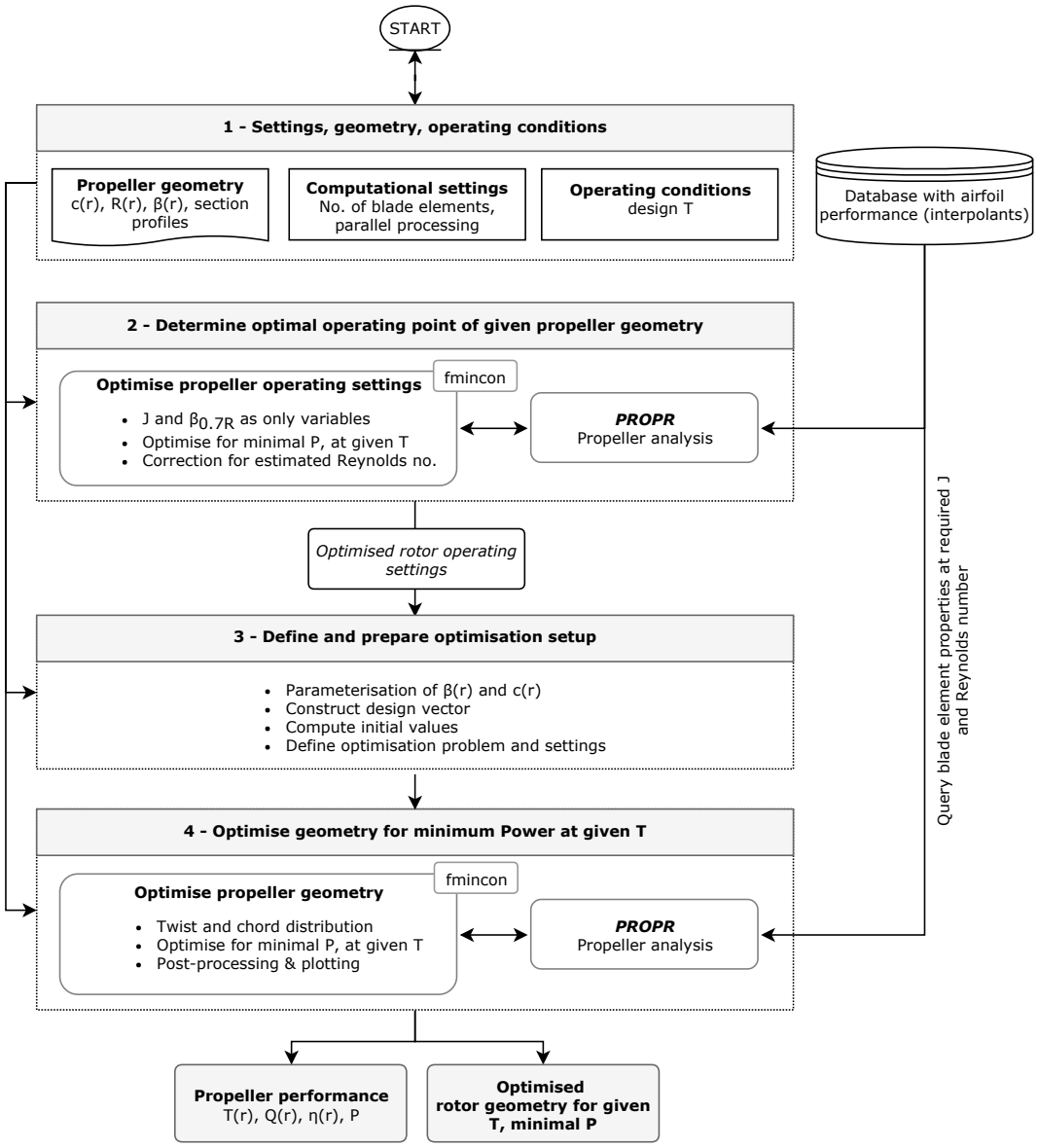

Figure 6.5: Functional diagram of the propeller optimisation tool, including PROPR.

can use different algorithms to determine the search gradient. Throughout this research the SQP algorithm is used. This algorithm is capable of recovering from NaNs in the constraint vector, which could occur when evaluating a non-feasible propeller geometry. Furthermore, SCP tends to have a higher convergence speed when compared to for example interior point algorithms. An overview of the complete optimisation routine is provided in figure 6.5.

Within the blocks as displayed in the functional diagram (figure 6.5) some notable subroutines and calculations are implemented to improve convergence speed, stability or execution speed in general. These are listed below, in no particular order:

- **Blade station properties:** An interpolant of blade element properties (as defined in table 6.2) is created using XFoil for the entire range of operating conditions expected. When analysing the propeller these airfoil properties are queried at the correct local experienced Reynolds number. This is possible because the airfoil shapes are excluded from the optimisation.

- **Reynolds number estimation:** In the first optimisation routine used to determine the optimal operating setting of the propeller the actual Reynolds numbers experienced and determined in *XRotor* are used as input in the first iteration of this optimisation routine. This minimises the influence of drag estimation inaccuracy as implemented in *XRotor*.

- **XRotor convergence:** If XRotor did not converge, interpolation is done using two adjacent operating points, to ensure continuation of the search algorithm. This is similar to what has been implemented for XFoil non-convergence. If unsuccessful, two additional adjacent operating points are included in the interpolation routine. Only when this interpolation also yields non-convergence, the particular operating condition is rejected.

- **Efficient setup:** The objective and constraint function defined in *fmincon* share persistent variables, to enable all calculations to be executed once in a single function call. The need for so-called global variables or intermediate storage of variables in external files as often implemented in previous work is avoided.

- **Parallel processing:** Unique identifiers are assigned to each XRotor instance and corresponding files. Any number of processor cores available can be used simultaneously.

- **Problem scaling:** Within the optimiser all constraints, design variables and objective value are normalised to provide *fmincon* with a properly scaled optimisation problem. This greatly improves the speed and gradient determination required within *fmincon*.

- **XRotor output precision:** The number of significant digits output by XRotor is increased to six, allowing for a smoother response to varying operating conditions. This aids in the determination of the search gradient within *fmincon*.

6.4.2. Design variables

A total of 15 design variables are used to define the propeller geometry and operating condition. These are listed in table 6.4 along with their respective upper- and lower bound. The step size used in finite differencing within *fmincon* is specified per design variable. Finally, the optimisation problem is set up in such a way that individual design variables can be easily toggled on or off. This makes it convenient to exclude a design variable from the optimisation routine and investigate the influence of individual variables to the optimisation routine. The advance ratio J is also a design variable in order to optimise the operating condition. As the velocity is prescribed by the incoming flow field, optimising the advance ratio essentially optimises the propeller rotational velocity.

Geometry parametrisation

The blade geometry is defined by a total of 14 parameters. The twist angles and chords lengths along the blade are defined by the root- and tip values and intermediate variation. The distribution is parametrised using a shape function and so-called Class Shape Transform (CST) coefficients, following the proven method of Kulfan [36]. Five CST-coefficients are used in the parametrisation of the chord- and twist distribution.

The airfoils themselves are unchanged during the optimisation, original *XPROP* airfoils are used. Excluding the airfoil from the optimisation routine greatly reduces the computational demands and enables the use of the described airfoil aerodynamic property database. Furthermore, one also does not have to take into account the structural consequences of changing the airfoil shape. This is especially relevant for the choice of a feasible airfoil thickness over chord ratio. The resulting optimised propeller geometry is therefore more likely to be a realistic and feasible geometry.

Table 6.4: Overview of all design variables used in the optimisation routine.

	Design variable	Lower bound	Upper bound	Unit
$x(1)$	CST 1 - $\beta(r)$	-2	1	[-]
$x(2)$	CST 2 - $\beta(r)$	-2	1	[-]
$x(3)$	CST 3 - $\beta(r)$	-2	0.75	[-]
$x(4)$	CST 4 - $\beta(r)$	-2	0.75	[-]
$x(5)$	CST 5 - $\beta(r)$	-1	0.75	[-]
$x(6)$	β_{root}	$0.6 \cdot \beta_{root}$	$1.5 \cdot \beta_{root}$	degrees
$x(7)$	β_{tip}	$0.6 \cdot \beta_{tip}$	$2 \cdot \beta_{tip}$	degrees
$x(8)$	CST 1 - $\frac{c}{R}(r)$	-1	1.5	[-]
$x(9)$	CST 2 - $\frac{c}{R}(r)$	-1	1.5	[-]
$x(10)$	CST 3 - $\frac{c}{R}(r)$	0	2	[-]
$x(11)$	CST 4 - $\frac{c}{R}(r)$	0	3	[-]
$x(12)$	CST 5 - $\frac{c}{R}(r)$	-2	7	[-]
$x(13)$	$\frac{c}{R}_{root}$	$0.75 \cdot \frac{c}{R}_{root}$	$1.5 \cdot \frac{c}{R}_{root}$	[-]
$x(14)$	$\frac{c}{R}_{tip}$	$0.75 \cdot \frac{c}{R}_{tip}$	$1.5 \cdot \frac{c}{R}_{tip}$	[-]
$x(15)$	J	0.75	2	[-]

6.4.3. Constraints imposed

A number of constraints are imposed in the optimisation routine, both equality- ($\bar{c}_{eq}$) and inequality constraints ($\bar{c}_{in}$). All constraints are normalised using their initial values to ensure a properly scaled design problem. The equality constraint imposed is used to enforce the thrust found for the given rotor geometry is equal to the set design thrust T_{des}. A maximum allowable deviation from the set constraint of 0.1% is defined. This provides an acceptable trade-off between accuracy and computational time.

$$\begin{aligned} c_{eq,1} &= \frac{T_{des} - T}{T_{des}} \quad \text{if XRotor converged, else:} \\ &= NaN \end{aligned} \tag{6.6}$$

A total of three inequality constraints are imposed. The first is used to limit the lift regime in which the blade stations are allowed to operate in. This is done for all stations individually. With this an extreme propeller design condition is avoided such that the propeller can also operate in off-design conditions without immediate stall over the entire blade. The constraint definition is shown in equation 6.7 below.

$$\begin{aligned} \bar{c}_{in,1} &= \frac{\bar{C}_l - 0.8 \cdot \bar{C}_{l_{max}}}{\bar{C}_{l_{max},init}} \quad \text{if XRotor converged, else:} \\ &= NaN \end{aligned} \tag{6.7}$$

The second and third inequality constraint are imposed to control the optimised geometry. It is desired to have a decreasing chord- and twist distribution towards the tip in the outer region of the blade. The reasoning is twofold; because of structural reasons and to ensure a smooth geometry. The constraints as implemented for the chord- and twist distribution are shown in equation 6.8 and 6.9 respectively. Note that only stations within $0.9 \leq \frac{r}{R} \geq 1$ are included in these both constraints.

$$\begin{aligned} \bar{c}_{in,2} &= \frac{\frac{c}{R}(r_{n-1}) - \frac{c}{R}(r_n)}{\frac{c}{R}(r_{n-1})} \quad \text{if XRotor converged, else:} \\ &= NaN \end{aligned} \tag{6.8}$$

$$\begin{aligned} \bar{c}_{in,3} &= \frac{\beta(r_{n-1}) - \beta(r_n)}{\beta(r_{n-1})} \quad \text{if XRotor converged, else:} \\ &= NaN \end{aligned} \tag{6.9}$$

In case of a non-feasible design point, due to for example divergence of XRotor, all constraints are assigned NaNs. The optimiser in that case tries a new design point.

6.4.4. Example optimisation of XPROP for uniform inflow

As an initial indication of the validity of the optimisation routine written, the baseline XPROP is optimised for uniform inflow. The optimisation goal is minimum power required of the propeller at given design thrust and provided inflow profile. As described in section 6.4 first the operating settings of the propeller are optimised. This is set to be the optimisation 'baseline'. After that, the propeller geometry is optimised for the found optimal operating condition. Different initial conditions led to the same converged design vector.

In this example uniform inflow with $V_\infty = 80 m/s$ and a design thrust of $T_{des} = 150N$ is considered. A comparison is made between the baseline XPROP and XPROP with optimised geometry. The baseline XPROP geometry is described in appendix B. In figure 6.6a and the efficiency as over the blade radius is shown. Similarly, the lift-over-drag ratio over the blade is shown in figure 6.6b. Over the entire blade both quantities are increased due to optimisation. The resulting optimised efficiency distribution approaches the ideal (constant) efficiency distribution as described by Betz. In the root region the efficiency is increased significantly due to optimisation. The required power of the optimised propeller is reduced with 10% compared to the standard propeller configuration. This is a first indication of a proper functioning of the optimisation methodology.

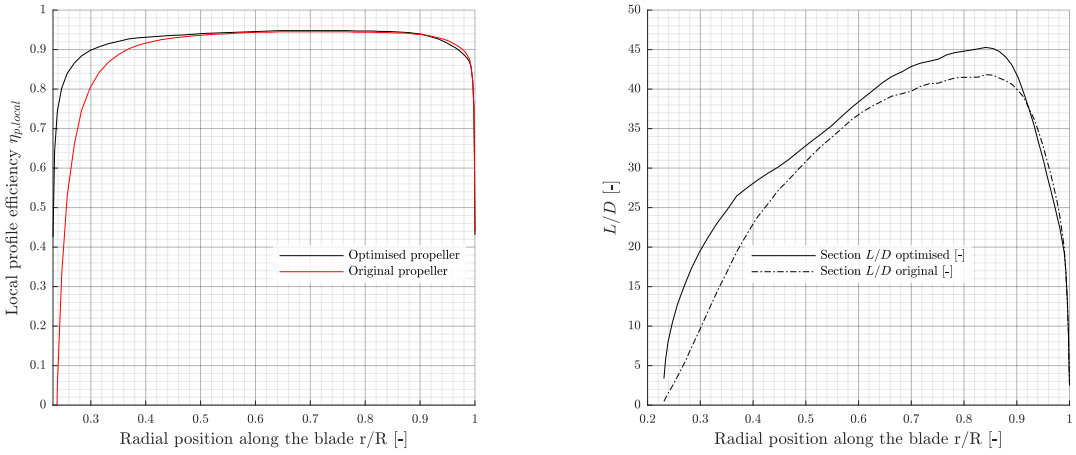

(a) Local blade efficiency η

(b) Lift-over-drag ratio L/D

Figure 6.6: Initial optimisation results of the original XPROP propeller with uniform inflow, $V_\infty = 80 m/s$ and $T_{des} = 150N$

7

CFD analysis of isolated propeller

With the lower-order propeller analysis and optimisation tool in place a higher-order method is used to further validate the obtained results from *PROPR*, in addition to the validation performed using wind tunnel results. With a CFD simulation also insight in the validity of propeller blade loadings is obtained. This is done by means of an isolated propeller CFD simulation using *ANSYS Fluent*, described in this chapter. The resulting blade loadings for different operating conditions are compared to the blade loadings obtained from the lower-order tool *PROPR*.

7.1. CFD Analysis setup - isolated propeller

The CFD analysis setup used here is developed in-house at Delft University of Technology. This setup is extensively validated with the use of multiple wind tunnel studies. However, to this date the exact set up has not yet been published. As the isolated propeller CFD simulation is simply used as validation tool within this research, no extensive reproduction of a validated setup is described. Therefore, a very brief description of the used setup is presented here. Wherever applicable solver settings as presented in chapter 3 and 4 are used here. This is done to enable integration of the isolated wing and isolated propeller simulation in a later part of this research, allowing for a relatively straightforward CFD simulation of the combined setup.

This CFD simulation is a direct reproduction of the OJF wind tunnel conditions performed at Delft University of Technology, described in section 6.3. Operating conditions are matched to those in the wind tunnel testing.

In figure 7.1 a schematic two-dimensional representation of the used domain is shown. To limit computational resources a wedge-shaped domain was used that encapsulates a single propeller blade.

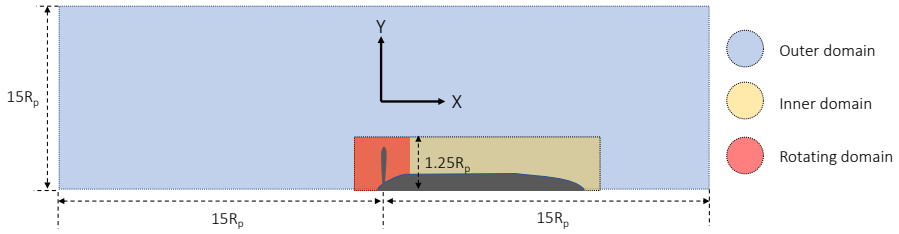

Figure 7.1: Schematic representation of the propeller CFD domain used.

The inlet, far field and outlet boundaries are placed at $15 \cdot R_p$ to prevent possible boundary interactions. A rotating reference frame is used to simulate the propeller rotation, imposed on the rotating- and inner

domain. The reference frame of the outer domain is stationary. The 'sides' of the domain are defined as periodic boundary conditions, since only a wedge of the entire propeller domain is simulated. A conformal mesh is used, thus no interpolation between the mesh interfaces is required. The used turbulence model is the Spalart-Allmaras model with modified source terms, as used in the validation- and baseline wing study presented in chapter 4.

As a transient simulation of the propeller is computationally intensive, the solving strategy used here differs from that described for the baseline wing. A pseudo-transient simulation is performed, with the propeller rotation simulated at various RPM using a rotating reference frame. For each RPM 3000 iterations are simulated to ensure convergence. This methodology has also been extensively validated in-house at Delft University of Technology and therefore not further discussed here.

7.2. Results: comparison of blade loadings from PROPR and CFD

In the following a comparison of results obtained from the isolated propeller CFD simulation and numerical tool *PROPR* is provided. As reference case the OJF wind tunnel tests are used, described in section 6.3. In figures 7.2a and 7.2b the torque distribution (dQ) over the propeller blade is shown. The advance ratio J is varied by variation in rotational velocity of the propeller. Two different advance ratios were analysed: $J = 0.74$ and $J = 1.11$, corresponding to $\omega = 6000$ rpm and $\omega = 4000$ rpm respectively. The freestream velocity is $V_{inf} = 30$ m/s. The results obtained from *PROPR* are included with and without 3D-correction implemented.

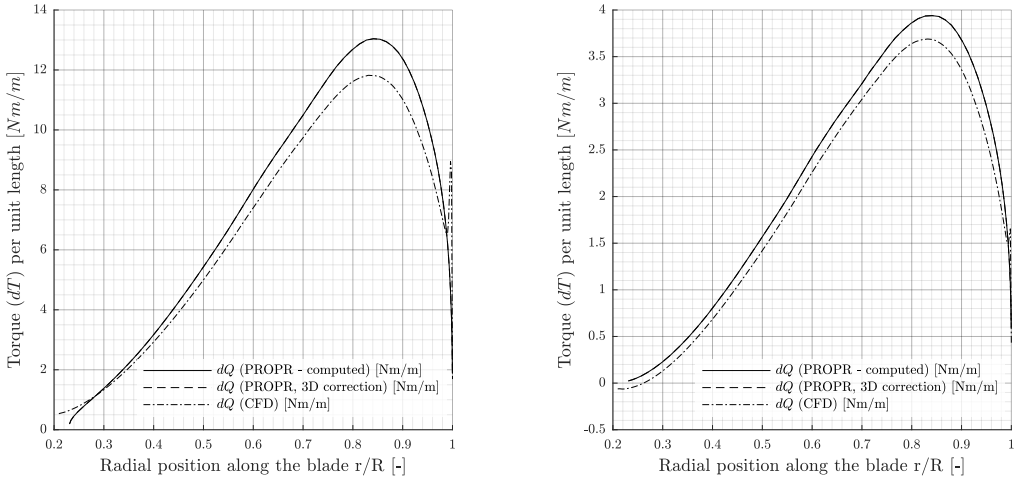

(a) dQ vs r/R - 6000 rpm (b) dQ vs r/R - 3000 rpm

Figure 7.2: Torque coefficient found in CFD and *PROPR* for XPROP propeller at $\Omega = 4000 rpm$ and $\Omega = 6000 rpm$, $V_\infty = 30 m/s$, $\beta_{0.7R} = 30°$

In figures 7.3a and 7.3b the thrust distribution (dT) over the propeller blade is shown for 6000- and 4000 rpm respectively.

It is seen that *PROPR* yields a slight overestimation of the torque- and thrust distribution. Integrated values of thrust- and torque are listed in table 7.1. A maximum deviation of 9.56% is found in total propeller thrust at the lowest RPM. Similarly, torque at 4000 RPM is overestimated by *PROPR* with 8.7%. At higher RPM *PROPR* seems to yield more accurate results with an overestimation of 4.5% and 7.6% in thrust and torque respectively.

When investigation the blade loadings, it is seen that at a lower RPM ($\omega = 4000 RPM$) there is a slightly higher deviation in both thrust- and torque at the inner sections of the blade. Near to the very root of the blade a slight deviation in the trends of dT and dQ are observed. Due to the presence of the spinner and nacelle wall effects are present in the CFD simulation, that are not accounted for in *PROPR*. The shape of

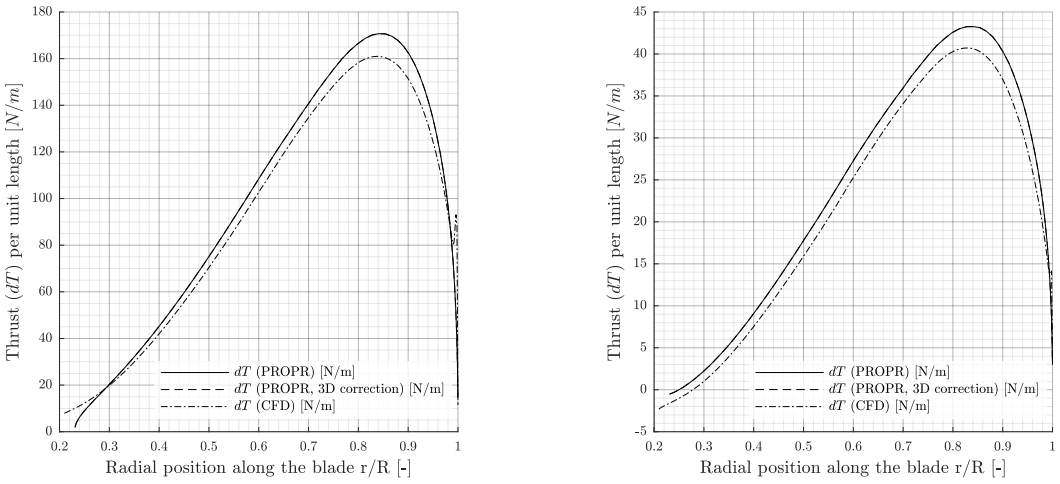

(a) dT vs r/R - 6000 rpm (b) dT vs r/R - 4000 rpm

Figure 7.3: Thrust coefficient found in CFD and *PROPR* for XPROP propeller at $\Omega = 4000 rpm$ and $\Omega = 6000 rpm$, $V_\infty = 30 m/s$, $\beta_{0.7R} = 30°$

Table 7.1: Comparison of CFD and *PROPR* of total thrust- and torque values

	4000 rpm		6000 rpm	
	T [N]	**Q [Nm]**	**T [N]**	**Q [Nm]**
PROPR	22.63	2.05	93.26	6.98
OJF CFD	20.66	1.89	89.27	6.49
Difference [%]	9.56	8.69	4.46	7.56

both distributions is very well matched. Also, the flow behaviour at the very tip of the blade $r/R > 0.97$ is not captured by the lower-order tool - as expected. However, this does not have any significant influence on the overall propeller performance estimation. The 3D-correction as implemented in PROPR has no influence in the considered operating conditions. The lift coefficients over the blade are not near maximum lift coefficients, and thus no correction is applied.

It is concluded that the lower-order tool *PROPR* provides an accurate representation of the thrust- and torque distributions over the blade. The observed discrepancies of the lower-order tool are equal to those found in previous research [5], [53]. The calculated (isolated) propeller performance in *PROPR*, considering comparable flow regimes, are assumed to be accurate.

7.3. Conclusions of part I

The goals set out for this second part of the research, investigation and modelling of the (isolated) propeller, have all been reached:

- ☑ Describe the fundamental principles of propeller performance
- ☑ Build an analysis tool capable of analysing and optimising an arbitrary propeller geometry given a (non-) uniform inflow field
- ☑ Validate this analysis tool using experimental and CFD results
- ☑ Implement a (validated) CFD simulation to investigate isolated propellers

The fundamental principles of propeller performance have been discussed, which provided the basis for selection of a suitable propeller analysis and modelling tool. Next, the setup and implementation of the

lower-order propeller analysis tool *PROPR* was presented. This tool was validated by means of existing wind tunnel studies. It is concluded that *PROPR* yields accurate results. Then *PROPR* was integrated into an optimisation routine to allow for geometrical design and aerodynamic optimisation of a propeller with non-uniform inflow fields. Preliminary results show successful optimisation of the propeller geometry with increased efficiency over the full blade radius. Finally, an isolated propeller was modelled using a (validated) RANS-CFD simulation. This was used to validate the blade loadings found in *PROPR*. Acceptable differences in the order of $5-7\%$ in total thrust- and torque were found comparing CFD and *PROPR*.

In the next and final part of this research all built tools will integrated, allowing for investigation of the combined wing- and propeller setup.

III

Propeller operating in the wingtip flow field

The final part of this research forms the synthesis of the foregoing investigations into the isolated wing and propeller. In this part of the research, the built tools will be combined and used to quantify the possible performance gains of wing-tip mounted propellers. The following goals are set:

- ☐ Present a quantified comparison of the baseline and optimised propeller performance
- ☐ Implement and validate a CFD analysis of the baseline wing and installed propeller
- ☐ Quantify the interaction effects of the wing and installed propeller
- ☐ Evaluate the validity of the lower-order propeller analysis tool by means of a transient CFD analysis

8

Optimising the propeller for the wingtip flow-field

In this chapter the optimisation results for a propeller placed in the wing-tip flow field are discussed. Following the optimisation methodology presented in section 6.4 multiple optimisation cases are evaluated. The effect of installing the propeller at the wingtip will be thoroughly reviewed. A range of thrust settings, the resulting changes in blade loading and geometry are explored. Variation in propeller performance due to geometrical changes such as propeller radius and number of propellers blades is presented in the final section of this chapter. Along with the presentation of results an elaborate discussion of these results is presented.

8.1. Influence of installing and optimising the propeller

The effect of geometry optimisation, installation and the combination of this is shown in this section. In table 8.1 the used propeller geometries are listed. Each point represents the performance of optimal operating conditions (in terms of $\beta_{0.7R}$ and J). Throughout this chapter the propellers are referred to as 'Geometry (condition)', e.g: 'OR-XPROP (installed)'.

Table 8.1: Overview of different propeller geometries used in performance comparison.

Propeller name	**Description**
OR-XPROP	XPROP
ISO-XPROP	Optimal geometry for isolated conditions
INS-XPROP	Optimal geometry for installed conditions

In figure 8.1 the propeller performance in terms of relative power required P (with respect to the OR-XPROP (isolated) propeller, total propeller efficiency η and rotational speed rpm is shown for a range of design thrust levels T_{des}. Dashed lines refer to performance in isolated conditions, solid lines indicate installed propeller performance. The maximum thrust level evaluated is $T_{des,max}$ = 275 Newton as this is the maximum thrust level that can be achieved by the OR-XPROP propeller in the desired isolated conditions. Put in perspective, the Tecnam (half) wing induced drag is $D_i \approxeq 240$ Newton.

Efficiency gains

From figure 8.1 a number of clear trends are observed. First, the overall propeller efficiency decreases with increasing design thrust in both the isolated and installed case. The possible efficiency gains due to installation of the propeller are significant. Up to 20 percent points increase in efficiency is achieved at lower design

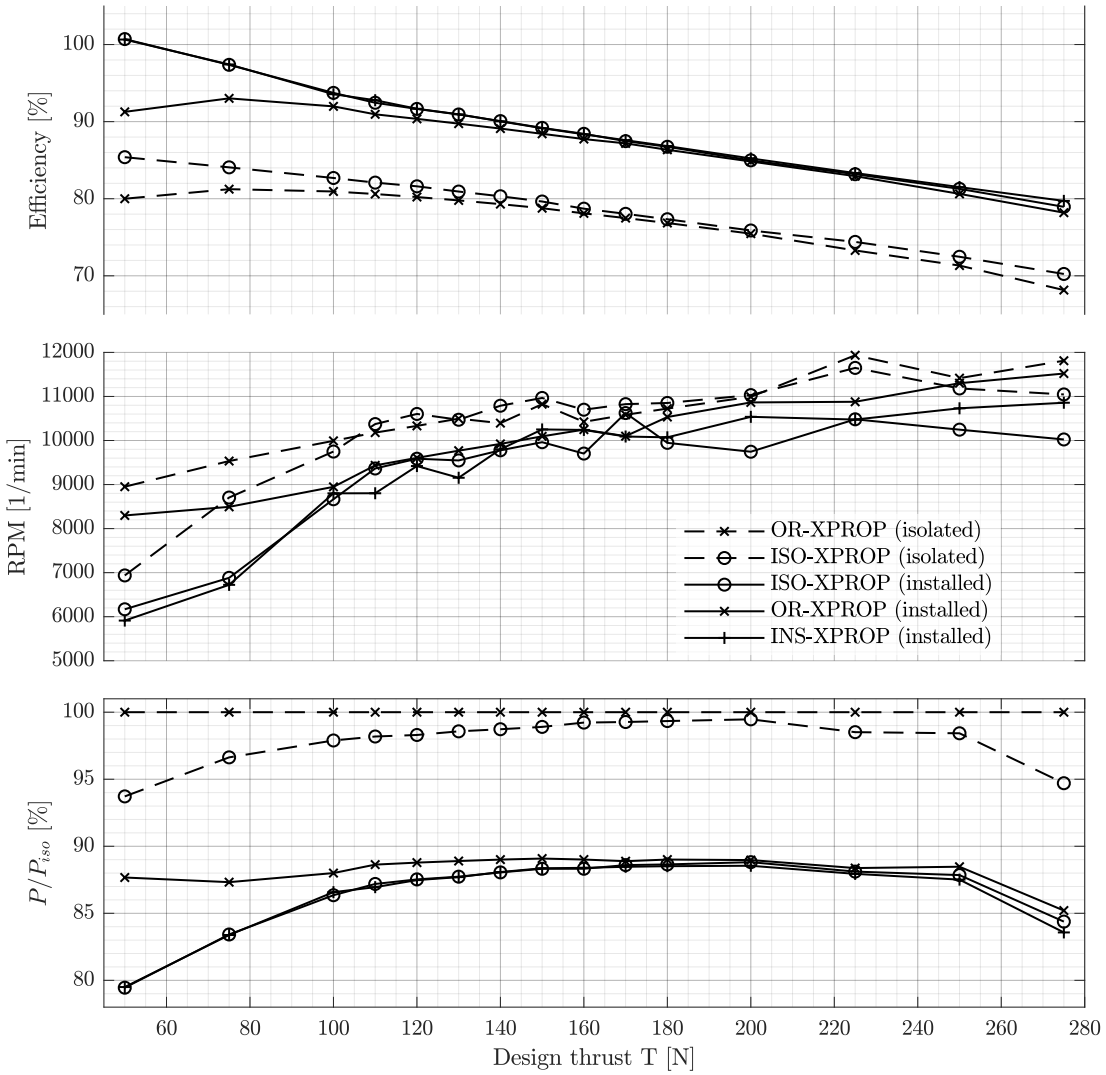

Figure 8.1: Optimisation results of XPROP propeller with $V_\infty = 80 m/s$ and Z = 6, for isolated and installed conditions and a range of design thrust levels. All cases are at optimal operating conditions.

thrust levels, decreasing to approximately 10 percent points at high thrust levels. Also, the $\delta\eta$ is nearly constant for the thrust range of $100 < T_{des} < 200$ N. The OR-XPROP propeller is apparently well-suited for this thrust regime and these inflow conditions. An interesting observation is the large relative gain in efficiency due to optimisation of the propeller geometry in both isolated and installed conditions at low ($T_{des} < 100$ N) and very high ($T_{des} > 200$ N) thrust levels. In these off-design conditions ($T_{des} > 200$ N) a large portion of the blade is stalled and geometrical changes lead to significant improvements compared to the OR-XPROP propeller. At low design thrust ($T_{des} < 100$ N) the root chord sections are relatively large, causing high profile drag. Both are aided due to geometry optimisation.

Optimal RPM and advance ratios

Since the freestream velocity is constant in this research, changes in advance ratio of the propeller are achieved by varying the propeller RPM. As expected the RPM increases with required design thrust, as there is a maximum effective blade angle $\beta_{0.7R}$ at which the propeller can operate. With installation of the propeller(s) the effective blade angle is increased to benefit from the incoming tangential flow. Thus a lower rotational speed

is required to deliver the same design thrust. There is a direct relation between RPM and efficiency: the most efficient propeller design and condition operates at the lowest rotational velocities. At higher thrust levels the optimiser no longer increases the propeller RPM. The high blade tip speeds cause excessive drag rise or even stall of the outer blade sections.

Relative power required

In the bottom graph of figure 8.1 the relative power required for each propeller design and inflow condition is plotted for various thrust levels. Again the effectiveness of geometrical optimisation in both isolated and installed conditions at low ($T_{des} < 100$) and very high ($T_{des} > 200$) thrust levels is clearly visible. This effect diminished at more average thrust levels, as the XPROP is apparently designed for those flow regimes and thrust levels. The reduction in required power is significant when installing the propeller, even for the XPROP with non-optimised geometry (OR-XPROP). Reductions up to 20% are achieved. Note that the installed propeller with optimised geometry for uniform inflow yields almost identical power reductions compared to the installed propeller with optimised geometry (INS-XPROP). Thus, effectively the propeller geometry is optimised for the required thrust level and to a lesser degree for the incoming flow field. Only at very high design thrust levels ($T_{des} > 220$) a noticeable difference in performance between the two different optimised propellers is observed.

The $\Delta(P/P_{iso})$ is nearly constant for the entire thrust regime of $T_{des} > 100$ N, meaning that the effective power reduction that can be achieved by installation and optimisation of the propeller does not change with thrust requirements. One would expect that the effective power reduction would decrease with increasing required propeller design thrust, as there is only a finite amount of energy to be 'extracted' from the wingtip vortices present in the installed case. Interestingly, the possible power reduction increases at very high thrust levels ($T_{des} > 250$ N). Because of the limited maximum thrust that can be delivered by the OR-XPROP propeller it is not possible to investigate the effective power decrease at even higher thrust levels. To overcome this thrust limitation the effective power decrease with varying design thrust is investigated for a modified XPROP propeller with more blades. This is described in section 8.3.

Bar chart of relative power reduction due to installation and optimisation

The relative power reduction for different design thrust levels is also plotted as a bar chart in figure 8.2. This provides a different visualisation of the power reductions achieved. Again the baseline (0%) is the OR-XPROP propeller in isolated conditions. As discussed, the maximum power reduction realised is more than 20% at $T_{des} = 50$ N.

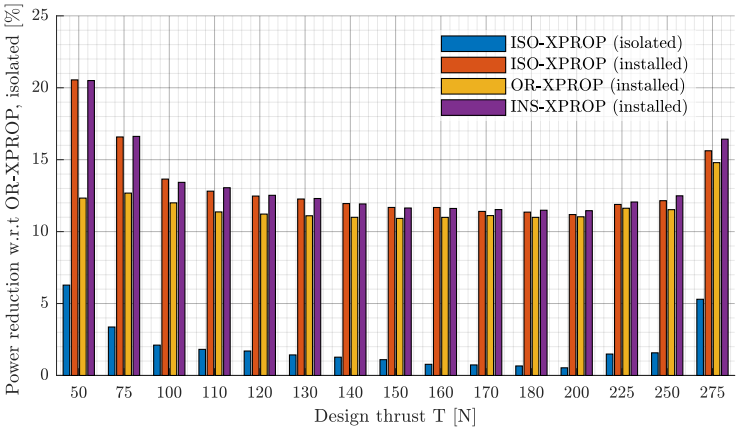

Figure 8.2: Bar chart of relative power reduction achieved due to geometry optimisation and installation effects for a range of design thrust levels. $V_\infty = 80 m/s$ and Z = 6

In figure 8.2 it is also very clearly visible that the power reduction of the propellers optimised for isolated and installed inflow conditions are nearly identical. As suggested, this indicates that the propeller is essentially optimised for the required thrust level. Apparently no extra power reduction when optimising the propeller geometry for the incoming flow field in installed conditions is possible. In some cases the power reduction by installing the ISO-XPROP propeller is slightly larger than that achieved by the INS-XPROP propeller. A difference in power reduction between the ISO-XPROP and INS-XPROP propellers is in the order of 0.1 percent points. This can be attributed to design freedom in the optimisation routine as the set constraint tolerances are finite.

Breakdown of contribution to total power reduction

Finally a visualised breakdown of the total power reduction is shown in figure 8.3. Here the power reduction achieved by installing the OR-XPROP propeller and by optimising the geometry of the OR-XPROP propeller for installed configuration (leading to the INS-XPROP propeller) as a percentage of the total power reduction ($P_{iso,OR-XPROP} - P_{ins,INS-XPROP}$) is shown. Again, this is done for a range of thrust levels of 50 – 275 N, well outside of the design thrust levels of the OR-XPROP.

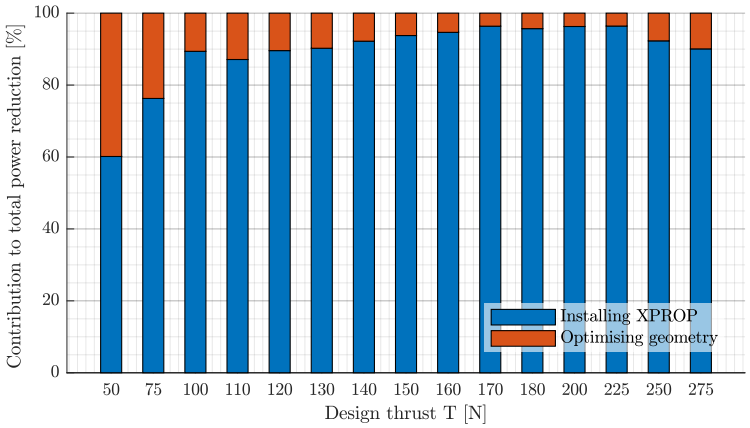

Figure 8.3: Bar chart with breakdown of contribution to total power reduction by optimisation and installation of the OR-XPROP propeller. $V_\infty = 80 m/s$, and Z = 6

What figure 8.3 shows is the decreasing effectiveness of optimising the propeller geometry with increasing thrust levels up to T_{des} = 170 N. Simply installing the OR-XPROP propeller at optimal operating conditions accounts for the majority of power reduction that can be achieved. At higher thrust levels ($T_{des} > 170$ N) the effectiveness of optimising the propeller geometry increases again. This can be explained by the fact that said thrust levels are outside of the design thrust regime of the OR-XPROP propeller. Stall at the root or tip of the blade (for low or high thrust requirements respectively) is mitigated by changes in propeller geometry done in the optimiser.

8.1.1. Changes in blade loadings and geometry

The resulting changes in the propeller blade loadings and geometry due to optimisation and installation are discussed for two different design thrust levels: T_{des} = 125 N and T_{des} = 225 N. The incoming velocity profile is expressed as the circumferentially averaged tangential velocity ratio: V_{tan}/V_{ax}. Furthermore the blade loadings and geometry of the OR-XPROP propeller in isolated conditions are shown as reference in each plot.

Optimisation for T_{des} = 125 N

First the results from optimisation of the OR-XPROP propeller with T_{des} = 125 N is discussed. In figure 8.4 the incoming velocity field, chord fractions, blade pitch angles, thrust- and torque distribution and the profile

efficiency over the entire blade radius are shown. Note that the tangential velocity ratio plotted is the ratio of the local tangential velocity over the local axial velocity.

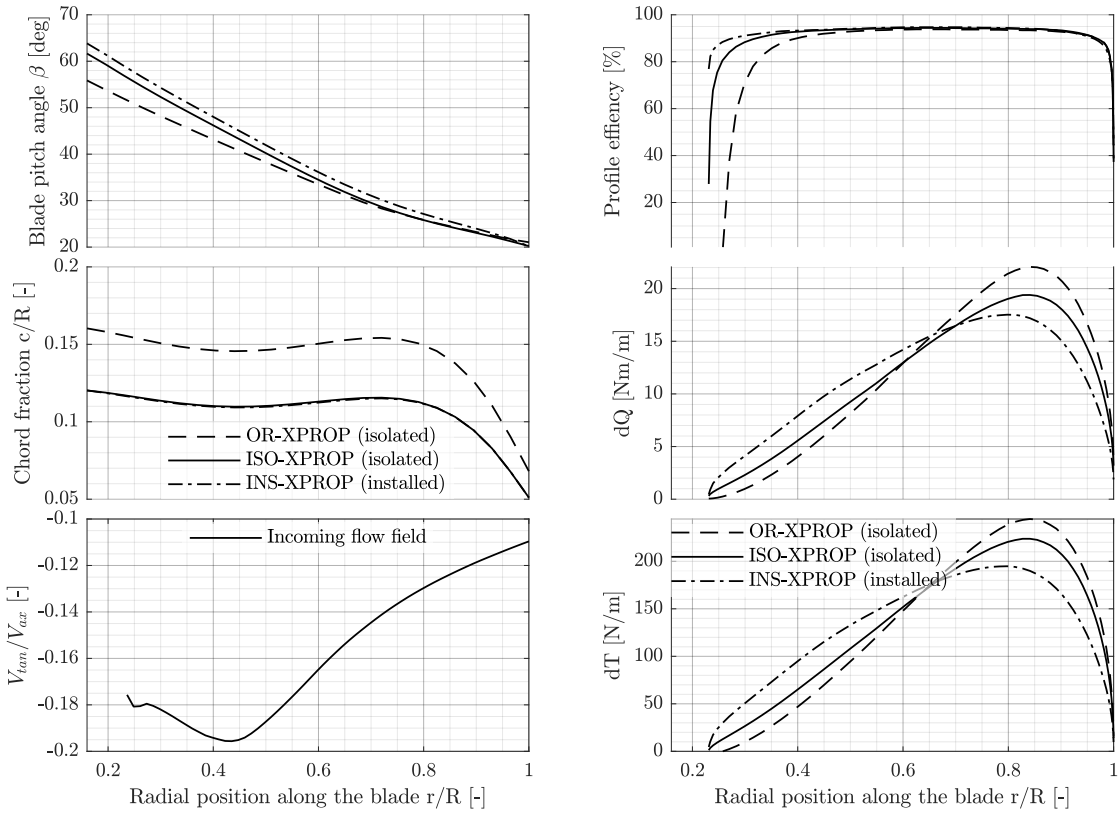

Figure 8.4: Blade loading and geometry changes of the OR-XPROP (isolated), ISO-XPROP (isolated) and the ISO-XPROP (installed) propellers. T_{des} = 125 N

It is seen that the chord distribution of the INS-XPROP and ISO-XPROP propellers are nearly identical, even though the INS-XPROP propeller is subjected to the non-uniform wingtip flow field. In both cases, the chord lengths are reduced by as much as 40% compared to the OR-XPROP. A slight increase in blade pitch angle in the root sections is observed. Note that all geometry parameters are well within the set boundary values. Both the optimised ISO-XPROP and INS-XPROP propellers show significantly higher efficiency in the root sections. Presence of the non-uniform inflow enables further efficiency gains. Combined, this leads to a higher local profile efficiency for the INS-XPROP propeller, especially in the root sections ($r/R < 0.4$). A clear trend is visible in the thrust- and torque distributions over the blade. Geometry optimisation of the OR-XPROP propeller causes both torque- and thrust distributions to shift inboard towards the root. Furthermore, the maximum value of both decreases. The same behaviour is observed when investigating the INS-XPROP propeller. An extra shift towards the root in both thrust- and torque distribution over the blade is seen, as well as lower maxima for both quantities.

In figure 8.5 the local lift coefficient, blade circulation and lift-over-drag ratio over the blade radius is shown. Again the incoming flow field is plotted as the fraction of tangential velocity over axial velocity.

It is seen that the lift coefficient and lift-over-drag ratio are increased over the full blade radius for both the ISO-XPROP and INS-XPROP propellers due to optimisation. Due to the presence of the tangential flow in the root sections ($r/R < 0.4$) of the propeller the local lift coefficients of the INS-XPROP propeller can be

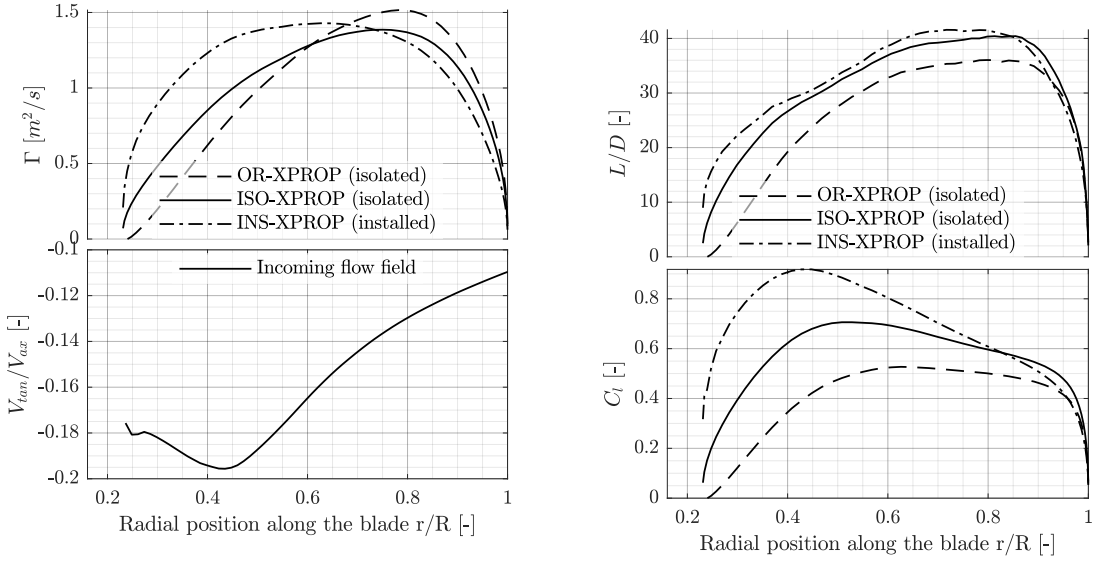

Figure 8.5: Blade loading and geometry changes of the OR-XPROP (isolated), ISO-XPROP (isolated) and the ISO-XPROP (installed) propellers. T_{des} = 125 N

increased with nearly 50% compared to the ISO-XPROP propeller. Note that in the tip region ($r/R > 0.8$) the lift-over-drag and lift coefficient of the INS-XPROP propeller is actually slightly lower than that of the ISO-XPROP. Apparently, this geometry leads to the highest overall efficiency. The blade circulation is clearly shifted inboard due to optimisation of the propeller geometry. This shift is more pronounced in installed conditions - for the INS-XPROP propeller the blade circulation is shifted inboard significantly with respect to the original OR-XPROP propeller in isolated conditions. Furthermore, the maximum blade circulation is decreased compared the OR-XPROP propeller.

Optimisation for T_{des} = 225 N

Next a higher thrust level of T_{des} = 225 N is investigated for all propeller geometries. In figure 8.6 the incoming velocity field, blade chord fractions, blade pitch angles, thrust- and torque distribution and the profile efficiency over the entire blade radius are shown.

In figure 8.6a it is seen the local blade chord lengths are increased in both the ISO-XPROP and INS-XPROP propellers compared to the original OR-XPROP propeller. This geometry change due to optimisation show a reverse trend than what was seen for the lower design thrust of T_{des} = 125 N, where the chord fractions were decreased due to optimisation. The local blade pitch angle is higher for both the ISO-XPROP and INS-XPROP propellers, as was the case for the propellers optimised for T_{des} = 125 N. As both the chord fraction and blade pitch angles are increased with respect to the baseline propeller geometry (OR-XPROP), the overall RPM is decreased for both propeller geometries to deliver equal design thrust. This is also visible in figure 8.1. Improvements in local efficiency are similar to those found when optimising the propellers for T_{des} = 125 N. In the root section efficiency is increased for both the ISO-XPROP and INS-XPROP propeller geometries. Note that the efficiency of the OR-XPROP propeller is relatively low in the tip region ($r/R > 0.85$) due to tip stall. Optimisation of the propeller geometry reduces this tip stall and the overall efficiency distribution is again an almost ideal constant distribution. Finally, again an inboard shift in thrust- and torque distribution is seen for the optimised propeller geometries.

In figure 8.5 the local lift coefficient, blade circulation, lift-over-drag ratio and incoming velocity profile over the blade radius is shown for propeller geometries with T_{des} = 225 N.

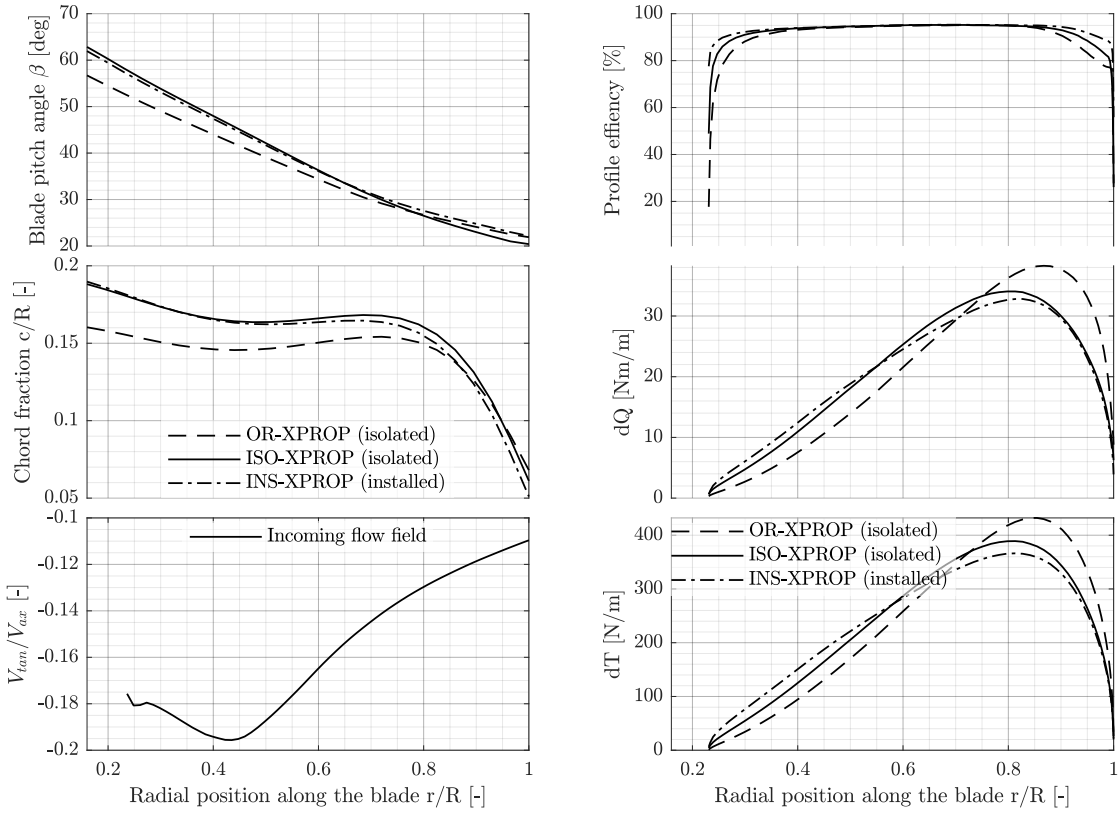

(a) $T = 225$ N (b) $T = 225$ N

Figure 8.6: Blade loading and geometry changes of the OR-XPROP (isolated), ISO-XPROP (isolated) and the ISO-XPROP (installed) propellers. $T_{des} = 225$ N

In figure 8.7a it is seen that blade circulation distribution shifts inboard due to optimisation and even more so for the installed INS-XPROP propeller. This was also observed for the propellers optimised for $T_{des} =$ 125 N. Also, the lift-over-drag ratio and local lift coefficients are increased over the entire blade radius, shown in figure 8.7b. The lift-over-drag ratio distribution of the OR-XPROP propeller clearly shows the presence of reduced aerodynamic performance of the tip sections. This effect is mitigated by optimisation, shown in the L/D distribution of the ISO-XPROP propeller. With installation and optimisation for the installed conditions the L/D distribution is increased even more, seen in the distribution of the INS-XPROP propeller.

8.2. Changing the propeller radius

Although not included in the optimisation routine, the propeller radius is an important design parameter. Therefore the performance of the propeller placed in the wingtip flow field is investigated for different propeller radii. This radius is varied between $0.8R < R < 1.2R$. A constant design thrust of $T_{des} = 100$ N is chosen, such that geometries with smaller propeller radii can also deliver the required design thrust. The hub dimension is kept constant and is not scaled with propeller radius. All other geometrical properties are scaled with propeller radius. Again the isolated, (scaled) OR-XPROP propeller at optimal operating settings is considered as baseline for each different scaling factor.

From figure 8.8 it is clear the overall efficiency η increases with increasing propeller radius. With increasing radius and equal design thrust, more mass is accelerated but over a lower velocity jump, thus at higher efficiency. Furthermore, some efficiency gains can be attributed to the lower required RPM with increasing

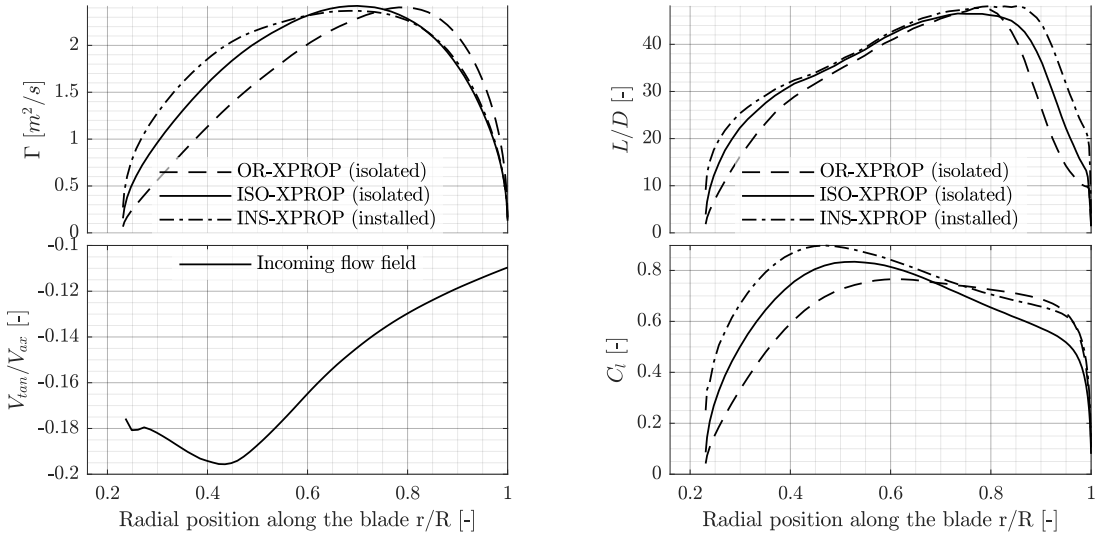

(a) $T = 225$ N (b) $T = 225$ N

Figure 8.7: Blade loading and geometry changes of the OR-XPROP (isolated), ISO-XPROP (isolated) and the ISO-XPROP (installed) propellers. $T_{des} = 225$ N

propeller radius. For a smaller propeller diameter, the RPM has to be increased to deliver the required design thrust. This leads to higher tip speeds and a large part of the propeller blade operates in Mach regimes of $M > 0.5$. Significant drag rise occurs because of this, increasing the required power to drive the propeller. Note that the drag rise model as implemented in XRotor represents a simplification of the actual stall behaviour that would occur over the blade. Thus efficiency losses for smaller propeller radii observed here could therefore be an overestimation. Nevertheless, the performance trend of a real-life propeller would be similar. It is concluded that given this design thrust level the power reduction that can be obtained increases with propeller radius.

In figure 8.9 the local blade circulation Γ and thrust dT are shown for different blade radii. Again, each line represents a propeller with optimal geometry and operating settings for installed conditions.

As expected the thrust- and circulation distributions shift towards the root and are increased in magnitude for propeller radii $R < R_{OR-XPROP}$. This is done in order to deliver the required propeller design thrust level. The opposite occurs for larger blade radii. For the largest propeller the maximum thrust shifts towards the region $0.7 < r/R < 0.8$.

8.3. Increasing the number of propeller blades for higher maximum thrust

As discussed in 8.1 the maximum sustainable thrust level delivered by the OR-XPROP (isolated) propeller is $T_{des} \approxeq 275$ N. In order to investigate the possible power reductions for higher thrust levels, the number of blades is increased to $Z = 8$ and $Z = 10$ from the original six-bladed XPROP propeller. These eight- and ten-bladed propellers are again evaluated and optimised in both isolated and installed configuration for a range of design thrust levels. In figure 8.10 the *absolute* power decrease with respect to the OR-XPROP propeller (with the respective number of blades) in isolated conditions is shown. All points represent the power difference found when analysing optimised propeller geometries.

The maximum design thrust that can be achieved with a 10-bladed XPROP propeller is $T_{des} = 360$ N. In figure 8.10 it is seen that the absolute power reduction ΔP increases over the entire thrust region. Interestingly, the absolute power decrease at a given design thrust level is nearly identical for any number of blades.

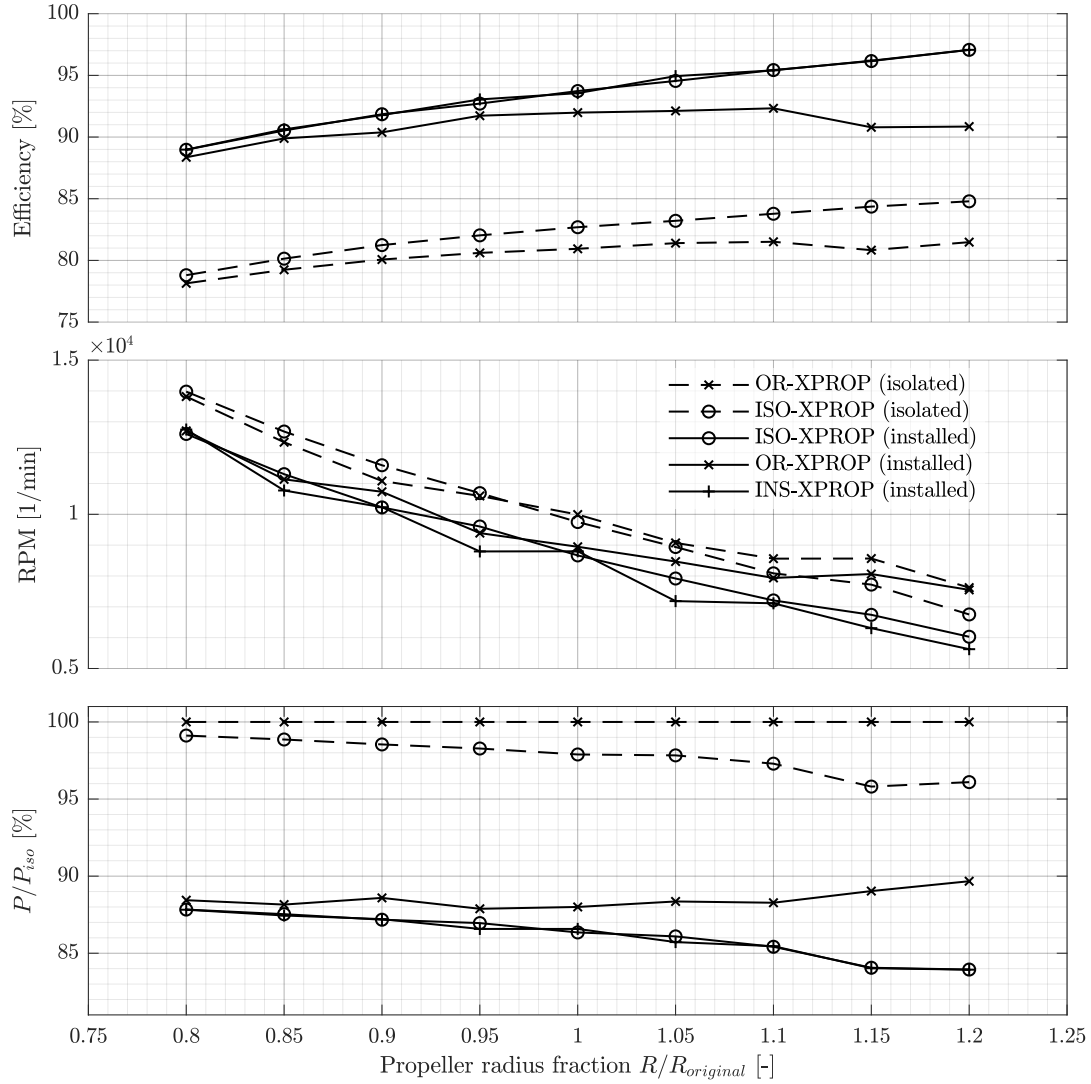

Figure 8.8: Propeller performance with varying propeller radii, with $V_\infty = 80 m/s$, Z = 8, T_{des} = 100 N. Geometries are that of the OR-XPROP, ISO-XPROP and INS-XPROP propellers in isolated and installed conditions.

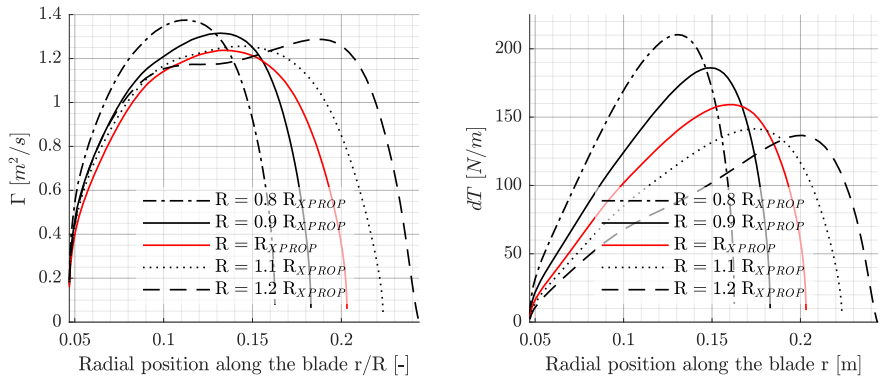

Figure 8.9: Circulation Γ and local thrust dT over the blade for different blade radii R. Properties for optimised propeller geometries (INS-XPROP) are shown.

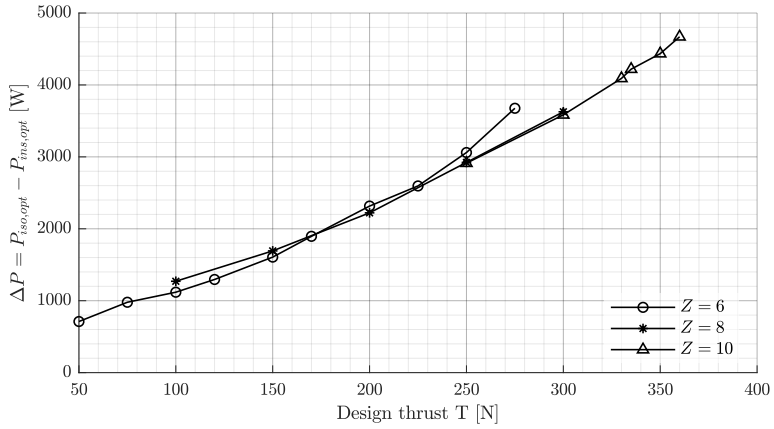

Figure 8.10: Absolute decrease in P_{req} for installed ISO-XPROP and INS-XPROP propellers with different number of blades Z and design thrust levels, $V_\infty = 80 m/s$

Thus the performance reductions that can be achieved by installing the propeller are independent of the number of blades on that propeller. Note that the assumed decoupled behaviour of the wing and propeller performance is invalid at higher thrust levels ($T_{des} >> D_{i,wing}$). In the next chapter (9) the upstream effects of placing a propeller in the wingtip flow are explored for different thrust levels.

8.4. The effect of a constant airfoil over the blade radius

The last optimisation case done is that of a fictitious XPROP propeller with a constant airfoil over the entire blade radius. In terms of structural properties this propeller geometry could be infeasible, but provides an interesting aerodynamic optimization study. In the following discussion the continuous airfoil propeller is referred to as *CA-XPROP*. For this study the airfoil normally at $R \approxeq 0.7R$ (section Q of the OR-XPROP propeller) was selected. Normally, this radial position is designed for the highest blade loading. In figure 8.11 an overview of blade loading and geometry properties for the ISO-XPROP (installed) and optimised constant airfoil CA-INS-XPROP (installed) is shown. As reference, the properties of the OR-XPROP (isolated) propeller is shown.

In figure 8.11 it is seen that the blade pitch angle and chord fractions are decreased for the optimal CA-INS-XPROP propeller, with the exception of the tip region. Because of these geometrical changes the blade efficiency is increased over the entire blade. Especially in the root section it is clearly seen that a small increase in efficiency is obtained for the ISO-XPROP propeller. The overall efficiency distribution of the CA-INS-XPROP (installed) is close to an ideal continuous distribution.

There is a notable overall increase in L/D of the ISO-XPROP (installed) compared to the OR-XPROP (isolated). A nearly constant lift-over-drag ratio is achieved over the entire blade radius, close to the maximum lift-over-drag ratio of the selected airfoil. The CA-INS-XPROP (installed) propeller provides significant additional improvement over the OR-XPROP in the root section of the blade. With the C_l behaviour in mind, this is mostly due to a lower drag coefficient in the root sections.

Finally it is observed that both the thrust- and torque distributions shift slightly outboard. As a result, the circulation distribution also shifts outboard. It is concluded that different airfoils in the root section allow for more efficiency improvements, compared to the original airfoil distribution of the OR-XPROP. Normally this would not be the main interest in propeller optimisation. However, given the presence of tangential flow in the root region in this scenario, airfoil optimisation for such a flow does impact the propeller performance.

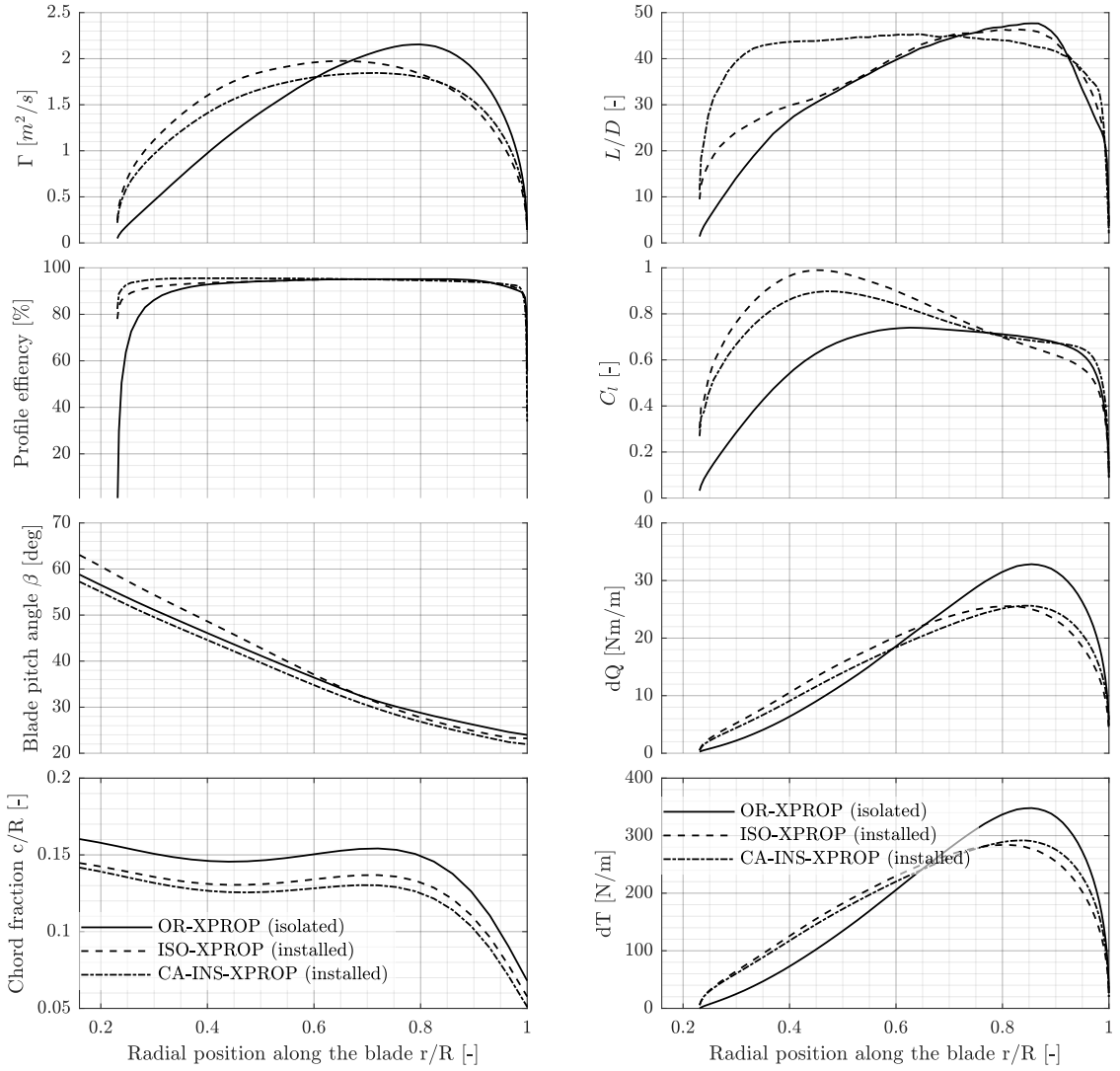

Figure 8.11: Blade loading and geometry changes of optimised propeller with constant airfoil along the radius, T_{des} = 180N

Breakdown of contribution to total power reduction for single airfoil

A breakdown of the contribution to total power reduction for the optimisation of the single airfoil XPROP propeller is shown in figure 8.12. Two different design thrust levels are evaluated: T_{des} = 100 N and T_{des} = 180N. Both cases are compared to the results obtained from optimisation and installation of the OR-XPROP propeller.

In figure 8.12 it is seen that geometry optimisation of the continuous airfoil OR-XPROP propeller has a greater relative influence (5%) on the power reduction in comparison to the original XPROP, at a design thrust level of T_{des} = 100 N. When optimising the propeller at a design thrust level of T_{des} = 180 N the influence of geometry optimisation is nearly identical in terms of relative power reduction for both propeller geometries evaluated.

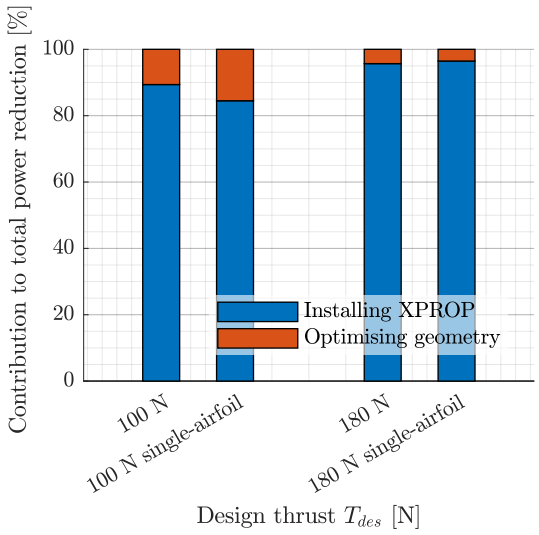

Figure 8.12: Power reduction breakdown of optimisation of single airfoil XPROP propeller (CA-OR-XPROP). $V_\infty = 80 m/s$, Z = 6.

8.5. Conclusions of the optimisation studies performed

From the extensive optimisation studies presented here a number of conclusions can be drawn. The optimiser successfully increases the propeller efficiency and reduces the power required. The reduction of required power of the propeller that can be achieved is significant. Over the entire thrust regime evaluated ($50 < T_{des} < 275$) N a power reduction of 12% with respect to the OR-XPROP (isolated) propeller is achieved. With $T_{des} = 50$ N more than 20 percent points in power reduction is obtained. Geometry optimisation has the most effect outside of the OR-XPROP propeller's design thrust regime. Optimisation of the propeller's geometry is dominated by optimisation for thrust level, not the incoming velocity profile. This is concluded from the comparison of the ISO-XPROP (installed) and INS-XPROP (installed) propellers - limited or even no difference in power reduction is observed. Interestingly the relative power reduction that can be achieved does not decrease with increasing thrust levels. Also, this is independent of the number of blades. Note that this conclusion only holds for the investigated range of design thrust levels.

A clear shift in blade loadings towards the root of the propeller is visible for all design thrust levels. Non-uniform flow present when installing propellers allows for an even stronger inboard shift of blade loadings. At higher design thrust levels performance at the blade tip is also of influence, as these tend to stall in non-optimised geometries due to high rotational velocities required.

From the final optimisation study of a constant airfoil propeller it is clear that the root sections have a large influence on the propeller performance when placed in the wing-tip flow field. The airfoil distribution of the OR-XPROP propeller seems to be a limiting factor in fully capturing the benefits offered by the presence of tangential flow in the root sections of the propeller. As shown a different airfoil in these root sections allows for a greater power reduction. Thus, it would be interesting to include airfoil optimisation of at least the inboard section in the design and optimisation routine to further improve the possible power reduction.

9

CFD Analysis with propeller actuator disk representation

Both the isolated wing and propeller have been investigated, using a high-order CFD tool and lower-order blade-element tool respectively. Furthermore the performance of a propeller subjected non-uniform inflow fields have been analysed and optimised for minimal propeller power required. A way of combining the lower-order *PROPR* and CFD method is simulating the wing in CFD and representing the propeller as an actuator disk. The actuator disk properties are obtained from *PROPR* described in chapter 6. In this chapter the method and obtained results using an actuator disk in CFD to simulate the propeller-wing combination will be described. Furthermore initial insight in the interaction effects of the propeller and wing is provided, in terms of the upstream effect of placing the propeller aft of the wingtip.

9.1. Implementation of actuator disk representation

Instead of resolving the full propeller blades individually in a (RANS) CFD simulation, the propeller can be modelled as an actuator disk (AD) [43]. Fundamental principles of actuator disks have been explained in section 5.2. In this research a method proposed by Sørensen et. al. is implemented [55]. This same methodology was successfully implemented and thoroughly validated by Stokkermans et al. [57]. In their research this actuator disk methodology was used to model wingtip-mounted (tractor) propellers. For an extensive overview and validation of said actuator disk implementation the reader is kindly referred to the work of Stokkermans, T.C.A et al. [57].

9.1.1. Actuator disk theory and methodology

In this research the propeller blades are replaced by a radial distribution of momentum and energy sources. An actuator disk (instead of a line-model) is used because blade loadings are only available as function of radius, since *PROPR* does not support azimuthal variations in incoming flow fields. Thus, the blade loading distributions are constructed using the radial thrust- and torque distribution over the propeller blade obtained from the lower-order *PROPR* tool. The momentum source term is presented in equation 9.1 below. In this equation T' and Q' are the thrust- and torque distributions per unit blade length. Furthermore $\vec{n}_T$ is a unit vector opposed to the thrust direction. Similarly a unit vector is introduced opposing the local torque direction, denoted by $\vec{\eta}_Q$.

$$\vec{F}(x,r,\theta) = \eta_x \eta_\theta \left(T' \vec{n}_T + \frac{Q'}{r} \vec{\eta}_Q \right) \tag{9.1}$$

The energy source term is presented in equation 9.2.

$$S(x,r,\theta) = \eta_x \eta_\theta \vec{F} \cdot \vec{V} \tag{9.2}$$

Regularization terms in axial- and azimuthal direction, η_x and η_θ respectively, are introduced to smoothly distribute the source terms in the propeller volume. This avoids possible singular behaviour and introduces a natural transition within the simulation domain. The axial regularization term is shown in equation 9.3. The regularization constant ϵ is set equal to the local cell size in the propeller domain, as suggested by S ørensen

$$\eta_x(x) = \frac{1}{\epsilon\sqrt{\pi}} e^{-\left(\frac{|x|}{\epsilon}\right)^2} \tag{9.3}$$

As an actuator disk model is used the regularization term in azimuthal direction is only a function of radius and not of θ. This term is shown in equation 9.4 below. In this equation Z is the total number of propeller blades (6 in this case), r is the local radial location along the blade.

$$\eta_\theta(r) = \frac{Z}{2\pi r} \tag{9.4}$$

A major advantage of using the actuator disk instead of line representation is the fact that the simulation becomes time-independent. Thus, the CFD simulation is solved as a steady problem, greatly reducing the computational intensity.

9.1.2. Computational setup

The complete simulation setup of this CFD simulation is identical to that described in 4, with the addition of the actuator disk implementation. The latter is implemented in the form of an external 'User Defined Function' (UDF) in *ANSYS Fluent*. With this UDF the radial distribution of blade loadings are read from external files generated within *PROPR*. The actuator disk methodology as described in the previous section (9.1.1) is executed within the UDF. This tool has been developed and validated in-house by T.C.A Stokkermans at Delft University of Technology and is implemented as such within this research.

All grid properties, solver settings and domain used here are described in chapter 4.

9.2. Upstream effect on the flow field of the installed propeller

The effects of installing of the propeller aft of the wingtip on the upstream (wing) flow field are explored in this section. For a range of propeller design thrust levels the combined wing- and propeller as actuator disk have been simulated. Unless otherwise noted, the location of investigation is at 0.05c upstream of the propeller.

Cut-planes upstream of propeller

Following the comparison of flow velocities as presented in chapter 3, cut planes at various upstream locations of the propeller are made here. The cut planes shown are at span-wise locations as visualised in figure 9.1. They are at 0.5c aft of the wing quarter chord point, or 0.05c upstream of the propeller. Propeller design thrust levels of T_{des} = 50, 120, 200, 275 N are investigated, complemented by a simulation without propeller present. No difference in grid properties exists between these simulations at various propeller design thrust levels. The span-wise location of flow investigation are also indicated in figure 9.1.

In figure 9.2 the normalised axial velocities are shown at z = 6.976, z = 6.775 and z = 6.663 m respectively. The second location is chosen to coincide with the (approximate) maximum loading location along the propeller blade ($r \approxeq 0.7R$).

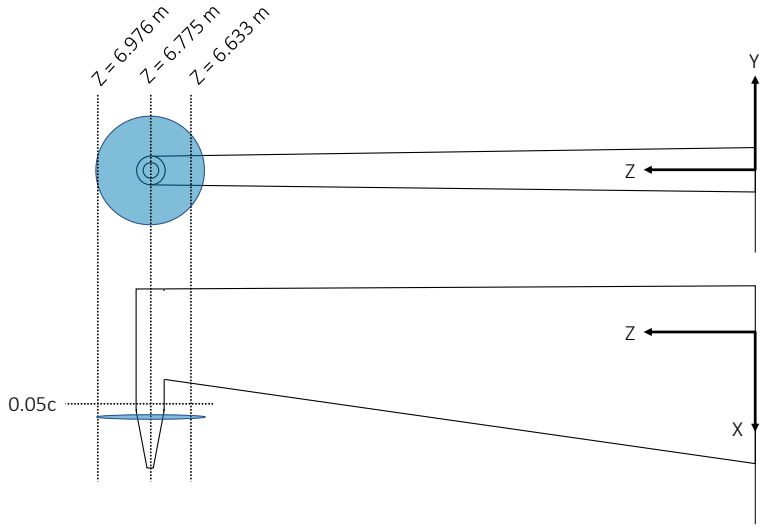

Figure 9.1: Top and rear view of the wing, propeller and defined cut planes at various span-wise locations. Note that the indicated wing and propeller are not to scale

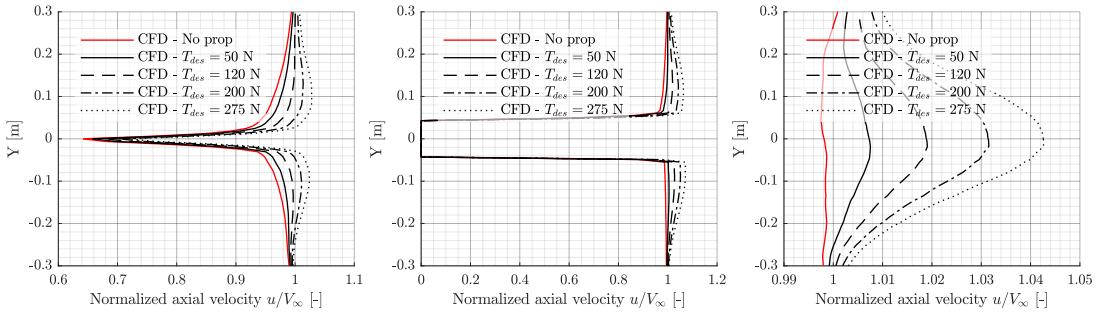

(a) $z = 6.663m$ (b) $z = 6.775m$ (c) $z = 6.876m$

Figure 9.2: Normalized axial velocity profile for various propeller design thrust levels, 0.05c upstream of the propeller. Three different span-wise locations shown: $z = 6.663$, $z = 6.775$ and $z = 6.976$ m w.r.t the wing root.

In figure 9.2 it is seen that the influence of the propeller on the upstream axial velocity increases with increasing propeller design thrust. Just outboard of the wing, at a single propeller radius away from the wingtip, an increase of 7.5% in axial velocity is observed for the highest propeller thrust level. Directly upstream of the propeller rotational axis the upstream effect of installing a propeller is slightly lower. An increase up to 6% is observed at $z = 6.775m$. At the exact same locations the in-plane velocities $\sqrt{v^2 + w^2}/V_\infty$ are evaluated, shown in figure 9.3.

Also when considering in-plane velocities it is observed that a higher propeller design thrust leads to a larger influence of the upstream flow field. In figures 9.3a and 9.3b it seen that above the wing the in-plane velocities are actually reduced due to the propeller installation. Outboard of the wing, at $z = 6.876m$ the in-plane velocities are increased with increasing propeller design thrust levels. Increases of in-plane velocities are in the order of $5-8\%$.

Changes in wing lift- and drag coefficient due to propeller installation

In figure 9.4 the change in wing lift- and drag coefficient due to installation of the propeller is shown.

The changes in overall wing lift- and drage coefficients are negligible, in the order of 0.1%. This variation can also arise due to further convergence of the CFD simulation. However, an increasing trend in both coef-

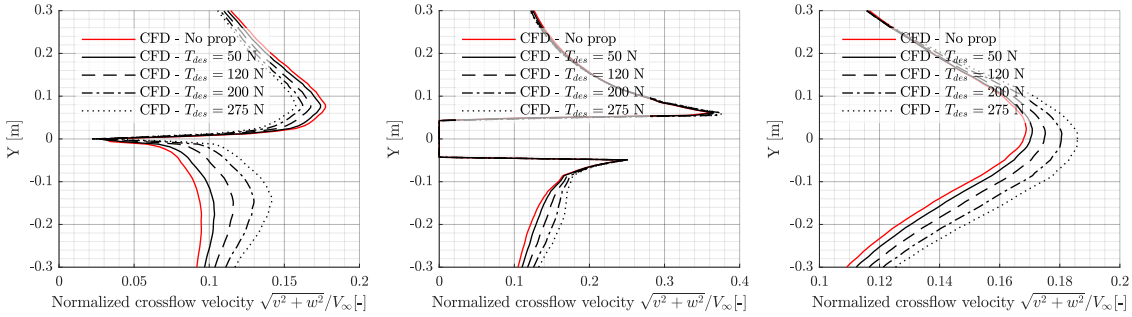

(a) $z = 6.663m$ (b) $z = 6.775m$ (c) $z = 6.876m$

Figure 9.3: Normalized in-plane velocity profile for various propeller design thrust levels, 0.05c upstream of the propeller. Three different span-wise locations shown: $z = 6.663$, $z = 6.775$ and $z = 6.976$ m w.r.t the wing root.

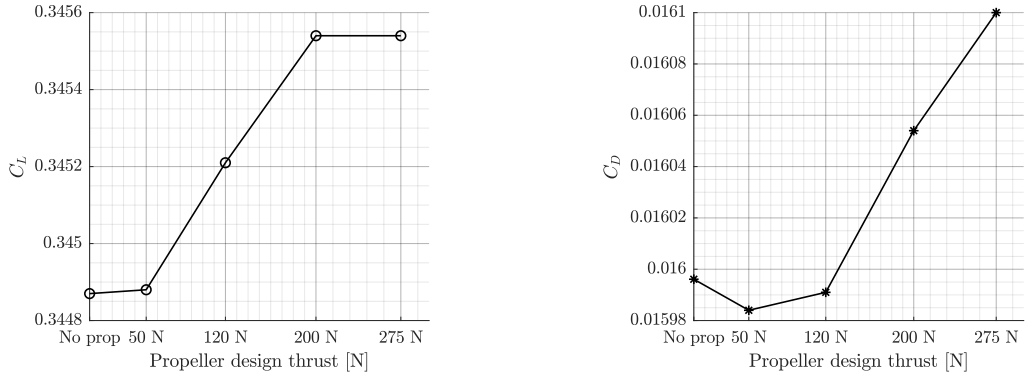

(a) C_L vs T_{des} (b) C_D vs T_{des}

Figure 9.4: Lift- and drag coefficients of the main wing - with and without installed propeller at various design thrust levels.

ficients is visible with increasing propeller thrust level. This could be explained by a slightly stronger suction over the wing due to the presence of the propeller. Nevertheless it is concluded the upstream effect of the propeller on the wing flow field is limited. The upstream influence is only noticeable (locally) at the very tip of the wing.

Changes in wing pressure coefficient due to propeller installation

A comparison of pressure coefficient over the main wing is made for the various propeller installation cases. The pressure coefficient C_P is evaluated at $b = 6.663$ m, directly upstream of the maximum blade loading of the propeller. Results are shown in figure 9.5, for propellers with T_{des} = 50, 120, 200, 275 N and an isolated wing without installed propeller.

It is seen that the pressure distribution over the wing is only changed at wing trailing edge due to propeller installation. A shift in pressure coefficient at the very wing trailing edge is visible with increasing propeller design thrust levels. Note that this shift seems to occur both under- and over the wing. From this preliminary investigation and thrust range the net effect of propeller installation on the wing pressure coefficient is found to be zero. Considering the trend in lift- and drag coefficient found, it could be that a stronger suction effect will occur at higher propeller thrust levels. Then, the overall wing lift coefficient increases.

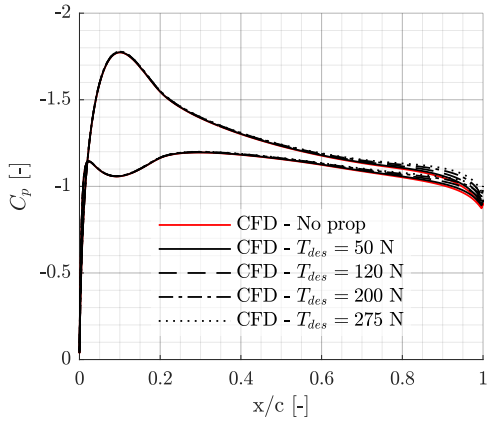

Figure 9.5: Variation in pressure coefficient over the wing due to propeller installation. Wing chord section at the span-wise location of $z = 6.663$ m is shown.

9.3. Downstream effect of the installed propeller

Finally the downstream effect of installing the propeller is investigated. The rationale of installing the propeller in part to cancel the tangential flow field present at the wingtip. As the propeller rotates in opposite direction of the wingtip vortex, the tangential velocity component should be cancelled or even reversed downstream of the propeller. Note that outboard *down* is defined as positive tangential velocity as seen from the propeller rotational axis. Thus the wingtip vortices causing downwash shows as *negative* tangential velocities outboard of the wing. In this section contour plots of the tangential velocity at 0.1c and 0.45c aft of the propeller plane are presented. This is done for the wing without propeller installed and including propeller at a design thrust of $T_{des} = 120$ N and $T_{des} = 275$ N.

In figures 9.6 and 9.7 contour plots of the tangential flow field at 0.1c and 0.45c downstream of the propeller respectively are shown. Dotted outline indicates the stream tube of the propeller, if present.

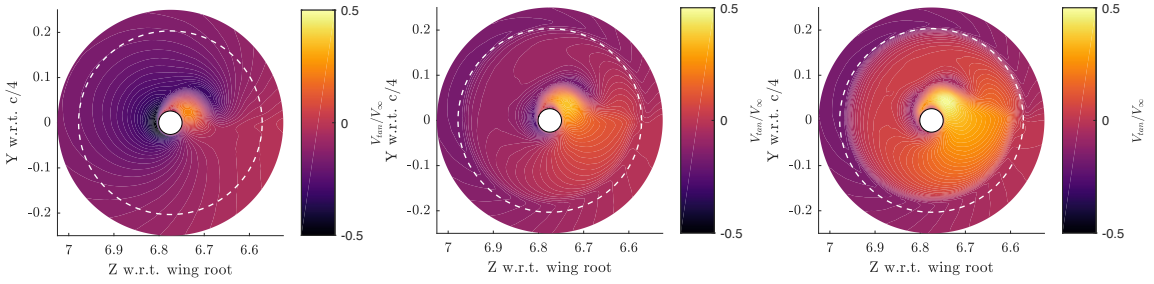

(a) No propeller (b) $T_{des} = 120$ N (c) $T_{des} = 275$ N

Figure 9.6: Contour of normalized tangential velocities for a wing without propeller, propeller at $T_{des} = 120$ N and $T_{des} = 275$ N. Cut plane at 0.1c downstream of the propeller.

It is clearly seen that the tangential velocities induced by the isolated wing are cancelled by installation of the propeller. This effect increases with increasing propeller design thrust, visible when comparing figures 9.6a and 9.6c. More downstream of the propeller the reversed tangential flow due to installation of a propeller is still visible but to a lesser degree.

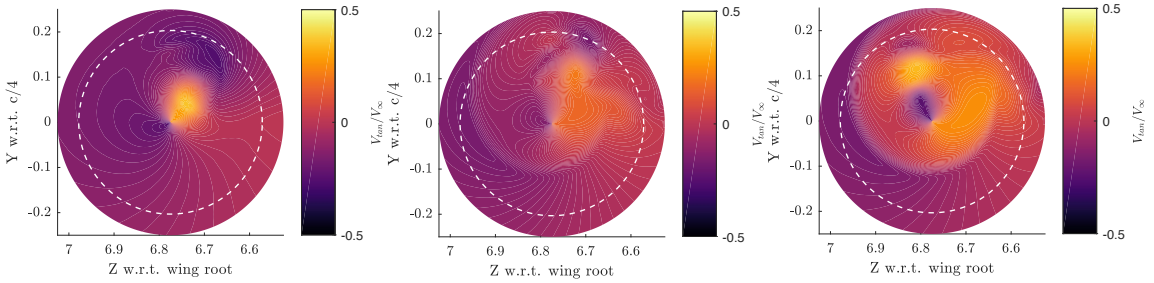

(a) No propeller (b) T_{des} = 120 N (c) T_{des} = 275 N

Figure 9.7: Contour of normalized tangential velocities for a wing without propeller, propeller at T_{des} = 120 N and T_{des} = 275 N. Cut plane at 0.45c downstream of the propeller.

9.4. Conclusions

From this investigation into installation effects of the pusher propeller on the surrounding flow field a number of conclusions are drawn. First and foremost, it is observed that there is a negligible upstream effect of the propeller on the wing flow field, especially at moderate thrust levels of $T_{des} < 200$. The changes in upstream axial- and in-plane velocities at the location of highest vorticity are limited, but increasing with propeller design thrust. The wing lift- and drag coefficients are effectively unchanged due to propeller installation within the considered propeller thrust range. Local wing pressure distributions upstream of the highest blade loading location show changes in the aft section of the wing only. Thus, the upstream effect on the wingtip flow field is very local. Downstream of the propeller plane successful cancellation of tangential flow is observed due to installation of the propeller. Again, this effect increases with increasing propeller design thrust.

Combined, the assumption that the propeller analysis and wing flow field can be decoupled seems to be valid for the considered range of propeller design thrust. A transient CFD-analysis in the next chapter will truly validate this.

10

Validation: RANS CFD analysis of wing and installed XPROP propeller

As final validation step of the lower-order tool *PROPR* a RANS CFD analysis is performed of the Tecnam wing and resolved XPROP propeller. This will provide accurate insight in the upstream effects and unsteady loading phenomena of the installed propeller.

10.1. Simulation setup and conditions

This CFD simulation is the integration of the baseline wing simulation (chapter 4) and the isolated propeller as described in chapter 7. The complete computational setup is thus equal to those presented in chapters 7 and 4. The only differences are the following:

- A transient CFD simulation is performed with the XPROP propeller installed.
- The propeller is fully resolved, no actuator disk is implemented. A rotating mesh is used to simulate rotation of the propeller.
- The solving strategy for this simulation is two-fold. First a steady (time-independent) simulation with rotating reference frame is performed to obtain an initial condition within relative limited computational time. Then, a transient simulation is performed, with time steps that correspond to a propeller rotation of $\theta = 2°$. Two full propeller rotations are simulated to ensure convergence.

The XPROP propeller operates at optimal operating conditions determined in *PROPR*, listed in table 10.1. A propeller design thrust level of $T_{des} = 175$ N is considered. As reference, the Tecnam wing induced drag is estimated to be $D_i = 240$ N considering a freestream velocity of 80 m/s, wing angle of attack of $\alpha = 3°$ and wing lift coefficient of $C_L = 0.345$.

10.2. Comparison of transient CFD and *PROPR*

In this section the comparison of results obtained from *PROPR* and the described transient CFD simulation is described. Comparisons in overall blade thrust, torque and wing lift and drag will be made. Streamlines over the individual propeller blades will be shown to investigate possible flow separation. In figure 10.1 a rear view of the wing and installed propeller combination is shown, including sign convention. The propeller rotates counter-clockwise, outboard down.

Table 10.1: Optimal operating conditions of the installed XPROP propeller for T_{des} = 175 N.

Parameter	Symbol	Value	Unit
Blade pitch	$\beta_{0.7R}$	30.085	deg
Advance ratio	J	1.162	-
RPM	ω	10169	1/min
Design thrust	T_{des}	175	N
Torque	Q	15.1	Nm

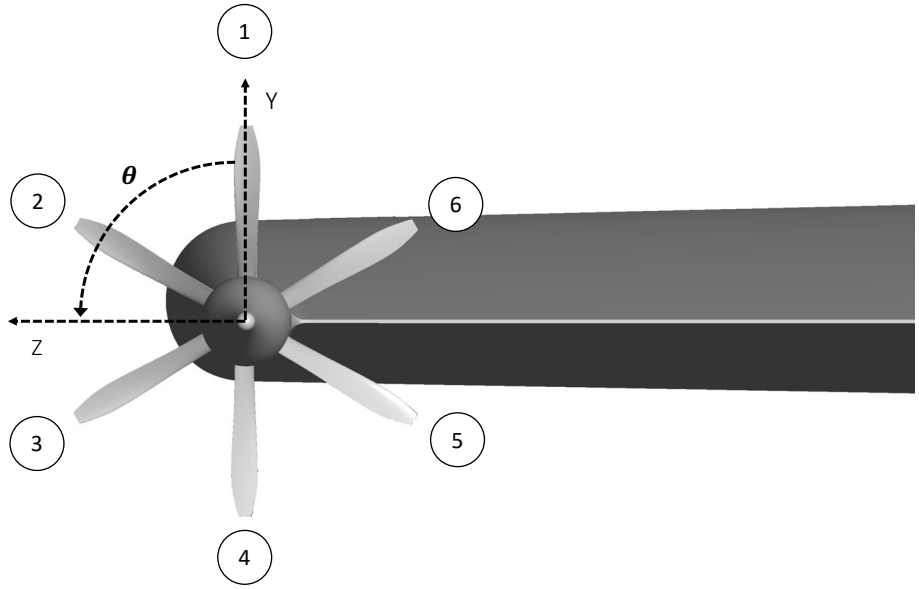

Figure 10.1: Schematic rear view of the wing and installed propeller, including sign convention.

The changes in (peak) total lift- and drag due to propeller installation and rotation are 0.08% and 0.85% respectively, compared to the actuator disk representation described in chapter 9. This difference is including the nacelle and spinner. Note that the drag found here is slightly higher than that found using the actuator disk simulation - 0.4 percent point. This could be attributed to small geometrical differences changes (blades and spinner surface) and a different solving strategy. Furthermore, the fact that discrete pressure sources are modelled instead of an actuator disk representation yields differences in found wing lift- and drag values with blade rotation.

10.2.1. Comparison of total thrust- and torque of the installed propeller

In figures 10.2a and 10.2b the normalized blade thrust- and torque (T/T_{PROPR}, Q/Q_{PROPR}) as function of propeller rotation is shown. For clarity the loading of a single blade is shown, blade 1, as indicated in figure 10.1. In addition the mean thrust- and torque obtained from transient CFD are shown, as well as the thrust- and torque values calculated using *PROPR*.

In figure 10.2a it is seen that the maximum thrust- and torque variations over a full blade rotation deviates no more than 20% from the mean thrust level found. Minimum thrust- and torque found are no lower than 65% of the mean values. Following the trajectory of the blade clear trends are observed:

- $\theta = 0°$: Initial position, blade up and perpendicular to the wing surface.
- $\theta = 90°$: Blade is fully outboard and subjected to the largest (negative) tangential velocities, thus highest thrust.

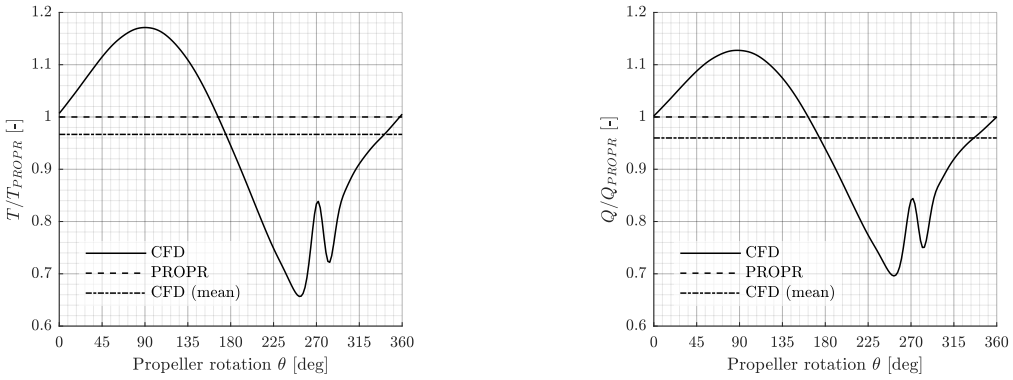

(a) T/T_{PROPR} vs θ

(b) Q/Q_{PROPR} vs θ

Figure 10.2: Comparison of normalised propeller thrust- and torque as function of blade rotation from transient CFD, mean values from transient CFD and lower-order tool *PROPR*. Following blade 1.

- $\theta = 180°$: Blade is again perpendicular to the wing but now fully down. Thrust delivered with inflow from under the wing is slightly lower.
- $\theta = 270°$: At this angle the blade is fully immersed in the wake region of the wing, showing a clear peak in thrust level, due to the lower axial velocity. The effective blade angle is increased of this.

Identical trends are observed when investigating the torque versus propeller rotation. The difference in mean torque- and thrust obtained from CFD is very similar to the torque- and thrust obtained from *PROPR*. Total blade thrust- and torque are overestimated 3.33% and 4.02% by *PROPR* respectively. This confirms the validity of implementing *PROPR* given these non-uniform flow fields.

10.2.2. Comparison of blade distributions of the installed propeller

In figures 10.3a and 10.3b thrust- and torque distributions over a blade at various propeller rotational positions θ obtained from transient CFD and *PROPR* are shown. Distributions at radial locations indicated in figure 10.1 are shown.

In figure 10.3a it seen that the thrust loading over the blade found in *PROPR* is nearly identical to that found in transient CFD over blade 1. Blade 2 and 3 are subjected to the largest tangential velocity field and indeed show the highest thrust magnitude over the blade. Most notably, these blades have a significantly higher thrust at the root sections of the blade. A drop in thrust near the root occurring over blades 5 and 6 is seen, as they are immersed in a flow with near-zero tangential velocity compared to the rest of the flow field.

Upon inspection of the torque distribution it is seen that again torque loadings obtained from *PROPR* are nearly identical to those over blade 1 in transient CFD.

10.2.3. Vortex structure aft of the wingtip

A final qualitative comparison is made between the vortex structure at the wingtip of the isolated wing and wing with installed propeller. Using a tangential vorticity definition the vortex structure originating from the wing- and propeller have been separated to allow for visual inspection. Identical isosurfaces are considered. The two vortex structures have a vorticity opposite in (in-plane) direction and are thus easy to separate using this definition. Note that this tangential vorticity is defined as seen from the propeller rotational axis. In figure 10.4 a side view of the vortex structure is shown. In the top view the vortex structure originating from the isolated wing is shown, in the bottom view that of the wing with installed propeller.

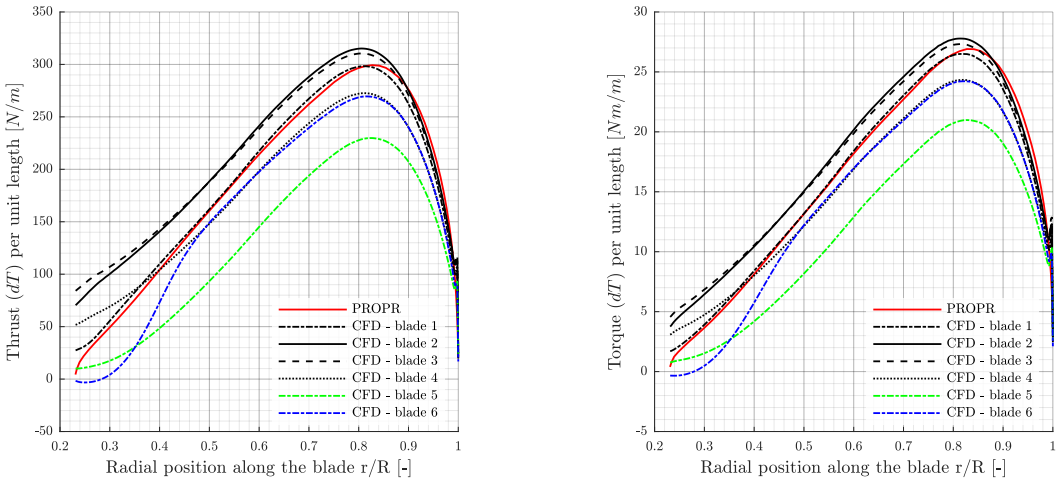

(a) dT vs r/R (b) dQ vs r/R

Figure 10.3: Comparison of propeller thrust- and torque distributions for a number of blade rotations θ from transient CFD and lower-order tool *PROPR*. Numbering of locations corresponds to those shown in figure 10.1

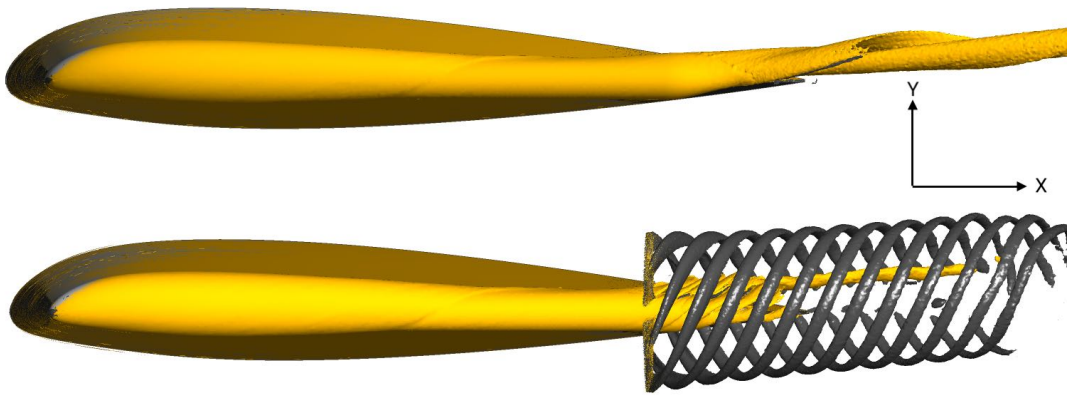

Figure 10.4: Side view of vortex structure. Comparison of vorticity in tangential direction (in-plane of propeller axis), for the wing (orange) and propeller vortex system (black). Top view is the isolated wing, bottom view depicts wing with installed propeller. Identical isosurfaces are shown.

It is clearly observed even with installed propeller blades the vortex originating from the main wing still exists downstream of the propeller. However, the vorticity aft of the wing is reduced as is clearly seen in the case with installed propeller. The trajectory is tilted downward due to the propeller. In figure 10.5 a rear view of the same vortex structure is shown. At the left-hand side of this figure the vortex originating from the isolated wing is visible, at the right-hand side the vortex originating from the wing with installed propeller is shown.

From figure 10.5 it is observed that the propeller blade (number 6) moves directly through the vortex core formed by the wing. This was also shown in chapter 9. A drop in thrust- and torque at the blade root was observed because of this.

In conclusion, the lower-order tool *PROPR* with circumferential averaging of the incoming flow provides an accurate estimate of the overall propeller performance. Both in terms of total thrust- and torque and their respective blade loadings, the non-uniform inflow considered here is shown to have limited impact on the accuracy of *PROPR*.

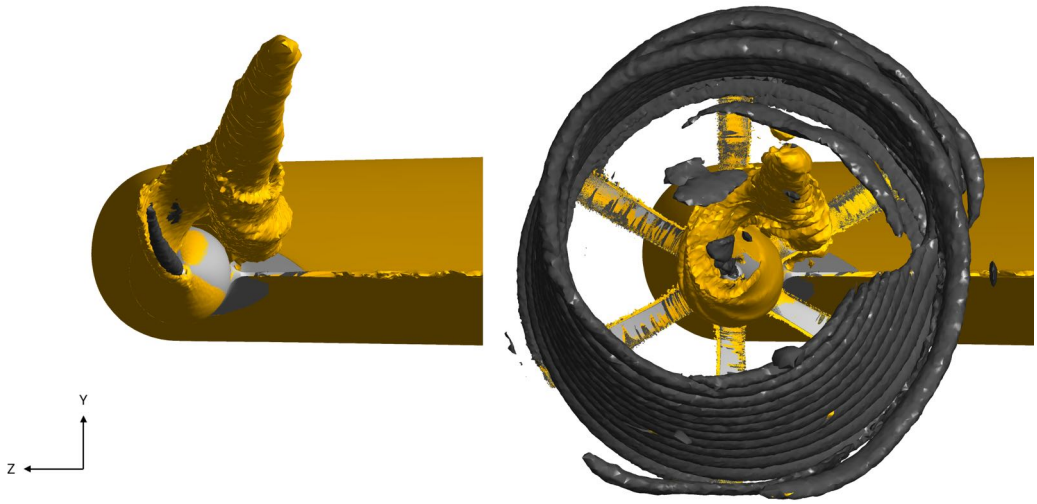

Figure 10.5: Rear view of vortex structure. Comparison of vorticity in tangential direction (in-plane of propeller axis), for both the wing (orange) and propeller vortex system (black). Left view is the isolated wing, right-hand view depicts wing with installed propeller. Identical isosurfaces are shown.

11

Conclusions and recommendations

The aim of this research was to perform aerodynamic analysis and optimisation of wingtip-mounted pusher propellers. At the start of this research two main research questions were constructed:

1. *What are the possible gains in propulsive efficiency by installing wingtip mounted pusher propellers?*
2. *What is the implication of this non-uniform inflow field for the propeller optimum design?*

In addition several sub-question were stated, listed in section 1.3. First conclusions that can be drawn from this research are presented in section 11.1. These will answer all main- and sub questions constructed at the start of this research. Finally recommendations for to improve upon the current and further research are presented in section 11.2.

11.1. Conclusions

Two major conclusions can be drawn from this research. First, installing a wingtip-mounted pusher propeller yields significant propulsive efficiency increases - more than 12% over the entire propeller thrust regime evaluated. Secondly, the built lower-order tool proved to be accurate and successful in fast design and optimisation of propeller geometry for flow fields with large tangential components, such as the wingtip flow field. This is of great use in the exploration of propeller designs for propellers with non-uniform and tangential inflow such as a wingtip flow field. In the following these conclusions and answers to the stated research questions will be further elaborated upon.

Wingtip flow field characteristics

The flow field behind the wingtip was shown to be highly complex of nature, but could be accurately represented using the validated CFD simulation described. At 0.1c aft of the wing, outboard and above of the wingtip negative tangential velocities with magnitudes up to $0.4V_\infty$ are found. Just inboard and over the wing a positive tangential flow is present ($0.25V_\infty$). The majority of this tangential flow field is captured within the radius of the installed XPROP propeller. Axial differences in the flow velocities are limited to a small region just above the wing.

Propulsive efficiency increases of wingtip-mounted pusher propeller

The propulsive efficiency increase achieved by installing the XPROP propeller is found to be at least P/P_{iso} = 12% when compared to the XPROP propeller in isolated conditions. At T_{des} = 175 N a 11% reduction in

required power is achieved due to installation. The Tecnam wing induced drag is estimated to be $D_i = 240$ N with $V_\infty = 80$ m/s, $\alpha = 3°$ and a wing lift coefficient of $C_L = 0.345$. Put in perspective, power reductions found in the experimental work done by Patterson [47] (described in section 1.2) at similar lift coefficients were found to be 14%.

The relative power reduction achieved due to installation of the propeller is nearly constant for all considered thrust levels. The absolute power decrease due to installation and optimisation increases with increasing thrust and is independent of the number of propeller blades. Physically, the amount of energy that can be extracted from the wingtip vortex is limited and thus the absolute power decrease should stabilise at very high propeller thrust levels. It is concluded that within the considered thrust range ($50 < T_{des} < 350$ N) a higher thrust level indeed yields a larger power reduction. The maximum achievable thrust of the XPROP propeller in the considered flow field was limiting in this research.

Influence of propeller design parameters on overall performance

No significant difference in performance is found when comparing both optimised propellers in installed conditions - the ISO-XPROP (installed) and INS-XPROP (installed). The ISO-XPROP and INS-XPROP propellers are optimised XPROP geometries for their respective flow fields: isolated and installed conditions. Note that the airfoil geometry is not optimised. From this it is concluded that the propeller geometry is essentially optimised for the desired thrust level and not the non-uniform inflow profile, within the considered range of thrust levels. However, in the optimisation of a constant airfoil propeller (CA-XPROP) there is an extra power reduction when comparing the ISO-XPROP and CA-INS-XPROP (optimised constant-airfoil propeller for installed conditions) in installed conditions. Thus, it is concluded the airfoil geometries of the XPROP propeller are a limiting factor in capturing the benefits of the present tangential flow and allow further power reductions when optimising the installed propeller.

With increasing propeller radius a slight increase in power reduction due to installation and optimisation is observed. At radii larger than $1.15R$ the power reduction remains constant with increasing blade radius. It is concluded the chosen XPROP propeller as baseline propeller geometry is suitable for this wingtip flow field, given the fact that a larger geometry does not lead to a significantly larger relative power reduction - within the given design thrust levels. At higher required design thrust levels ($T_{des} > 350$ N) a larger radius *is* expected to deliver larger relative power reduction.

Upstream effects of installing a wingtip-mounted pusher propeller

The upstream effects of installing the propeller are negligible, especially at lower thrust levels $T_{des} < 150$. As reference, the wing induced drag in this case was estimated to be 240 N. A small shift in pressure distribution over the wing is noticed, the net effect on lift- and drag coefficients is near zero. Also, small changes in magnitude and direction of the local flow field are noticed, in the order of $2-5\%$ at the very wing tip. Because of this, the efficiency increase and required power decrease of the combined wing and propeller system is equal to the efficiency increase and required power decrease found for the propeller. It is concluded that no iterative loop in the optimisation of the propeller is required, as the incoming flow field is nearly independent of the propeller thrust. The implemented methodology is thus valid within the considered thrust range. However, there seems to be a very small upward trend in upstream influence with increasing propeller thrust ($T_{des} > D_{i,wing}$). One can conclude that interaction effects between the wing and propeller do become significant at these thrust levels and should thus be accounted for in the methodology used.

Optimal propeller blade geometry and operating conditions

Optimising the propeller for a given design thrust shows that blade loadings shift towards the root. Installing and optimising the propeller geometry for the wingtip flow field leads to a more pronounced inboard shift of blade loadings. Because of the tangential velocity component present the effective blade angle over a large portion of the propeller radius increases and thus the RPM, local blade angle or chord length can be

reduced in order to deliver equal design thrust. Overall it is concluded that a smaller chord length and RPM is preferred given the XPROP propeller geometry, as shown in the optimisation study. Again, the root airfoil geometry of the baseline XPROP propeller is concluded to be a limiting factor in further optimisation of the blade geometry.

Validity of using the lower-order *PROPR* tool

The incoming flow field imposed on the propeller is circumferentially averaged, as this is required when using XRotor. Next to that a time averaging of the incoming flow field is done, as this field is obtained from a steady CFD simulation. Because of the small wing angle of attack ($\alpha = 3°$) this time averaging is valid. It is concluded that an accurate performance estimate of the propeller is obtained. At advance ratios of $0.8 < J < 1.2$ the found torque-, thrust- and power coefficients in *PROPR* are within 15% deviation from the both wind tunnel results. An overestimation by *PROPR* of $5-7\%$ in total thrust- and torque were found comparing the isolated propeller CFD at $J = 0.75$. Comparison with transient CFD simulations of the combined wing and installed propeller with $T_{des} = 175$ N showed great correspondence with the results found using the lower-order tool *PROPR*. Thrust- and torque values found in *PROPR* are overestimated by 3.5% compared to the mean values found in transient CFD. Maximum torque- and thrust amplitude of the propeller are within $0.7T_{des} < T_{des} < 1.2T_{des}$ over the full blade rotation. The non-uniform inflow, varying blade loading of the propeller with rotation and influence of the wing wake are shown to have limited impact on the values computed in *PROPR*. It is concluded and validated that the lower-order tool *PROPR* provides a fast and accurate method of estimating propeller performance given a non-uniform inflow.

11.2. Recommendations

Although all research questions have been answered, improvements upon the current research can be made. In this section some recommendations for future research are presented.

- As concluded in the previous section the airfoil geometries of the XPROP propeller used seemed to be a limiting factor in further optimisation of the propeller performance. The root section airfoil designs are often not of great interest in propeller research and limited by structural requirements. Considering the non-uniform flow field investigated here, additional research into aerodynamic optimisation of these root sections is desired. In future research optimisation of the airfoil geometries could be included in the optimisation routine, at least those in the root sections of the blade ($r < 0.4R$).
- The XPROP propeller can only deliver a limited thrust level in the considered flow field. Within this thrust range the relative power reduction was found to be independent of thrust level. Higher thrust levels using a different propeller geometry can be explored. Most likely a larger propeller is required, as increasing the number of blades of the XPROP propeller was done in the current research. In doing so the trend of relative power reduction can explored, as it is expected this decreases with increasing propeller power required.
- Similar to the investigation of power reduction trends with a propeller that can deliver higher thrust levels, it can be explored up to what thrust level the upstream flow field remains unaffected by installation of the propeller. Then, the complete range of propeller thrust for which the decoupled *PROPR* methodology is valid can be determined.
- In this research a single propeller location and position with respect to the wing was evaluated. A different downstream location, alignment with the local flow field (i.e. tilting the propeller plane with the wing angle of attack) and upward shift of the propeller location would be good to investigate.
- It would be interesting to evaluate different wing- and nacelle configurations. Ideally, both would be designed to generate a stable and near axisymmetric vortex structure that is aligned with the propeller.

- Instead of using a circumferentially averaged flow field as 'input' for the propeller, in future research an actuator line model to account for the circumferential differences present in the flow field could be implemented.

A

Additional description and results for the isolated wing validation

In this appendix additional background information on the simulation of the isolated wing case as described in chapter 3 is given.

A.1. Flow properties based on experiment

In the experiment by Chow [13] used as validation only the freestream Mach number M_∞, freestream velocity V_∞, turbulence intensity level T_u and the chord-based Reynolds number Re_c are specified [13]. Furthermore the model dimensions are provided and thus the wing chord length is known. In order to determine all required flow properties the (static) temperature or static pressure must be assumed. It is chosen to assume a static temperature $T_{s,\infty}$ equal to that specified in ISA at sea level. An expression for the static pressure is then obtained by substituting the ideal gas law (A.1) into the definition of Reynolds number (A.2). The dynamic viscosity μ is calculated using Sutherland's laws and thus a function of (assumed) temperature.

$$\rho = \frac{P}{RT_{s,\infty}} \tag{A.1}$$

$$Re = \frac{\rho V_\infty c}{\mu} = \frac{P_{s,\infty} V_\infty c}{RT_{s,\infty}\mu} \tag{A.2}$$

In table A.1 the fluid properties set for air in ANSYS are listed. Note that air density ρ is calculated as an ideal gas. Furthermore the viscosity μ is calculated using Sutherland's laws [59], based on the static (freestream) temperature.

Table A.1: Properties of air as defined in ANSYS Fluent

	Symbol	Value	Unit
Density	ρ	set as ideal gas	kg/m^3
Heat capacity	C_p	$1.0047 \cdot 10^3$	m/s
Thermal conductivity	K_t	0.0253	[-]
Molecular weight (air)	M_{air}	28.9644	kg/mol
Reference dynamic viscosity	$\mu_{0,ref}$	$1.78938 \cdot 10^{-5}$	kg/ms
Effective temperature	S	110.4	K

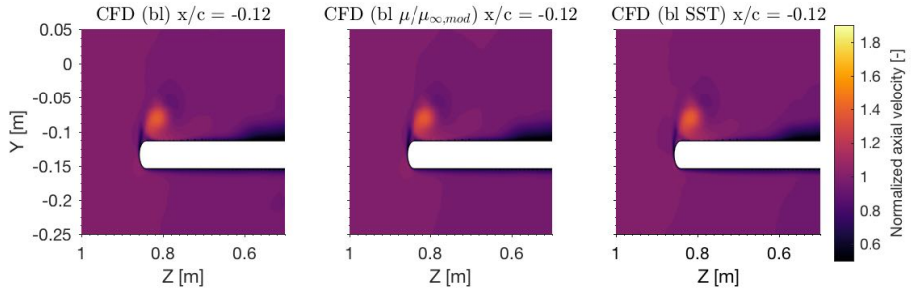

Figure A.1: CFD S-A, $\frac{\mu_t}{\mu}_{mod}$, $SST-\kappa\omega$ compared. Contour plots of the normalized axial velocities $\frac{u}{U_\infty}$ at $x/c=-0.12$

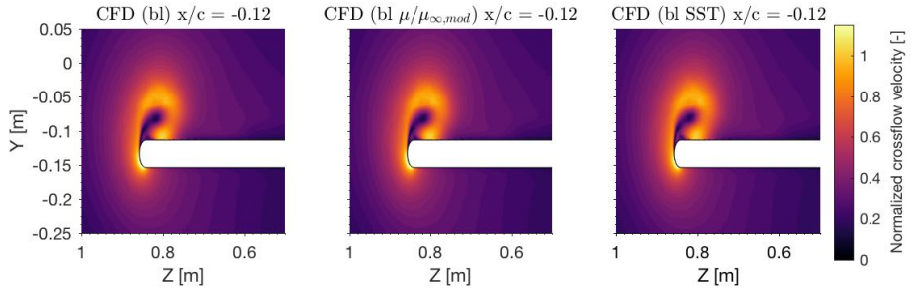

Figure A.2: CFD S-A, $\frac{\mu_t}{\mu}_{mod}$, $SST-\kappa\omega$ compared.Contour plots of the normalized crossflow velocities $\frac{\sqrt{v^2+v^2}}{U_\infty}$ at $x/c=-0.12$

A.2. Additional CFD results - isolated wing

In this section additional results of the isolated wing simulation case can be found. In figures A.1 and A.2 the influence of different freestream settings and a different turbulence model is shown for additional cross-planes. Note that the early formation of the vortex is nearly identical for both the SST-$\kappa\omega$ and S-A turbulence model, only downstream of the wing the difference is noticeable.

B

Baseline wing geometry

The baseline wing and spinner design are based on the Tecnam P2006T aircraft, the aircraft also used as baseline in NASA's SCEPTER programme [48] investigating distributed propulsion. The original design was slightly simplified, omitting the winglets and outboard dihedral. Winglets are used to mitigate the negative effects of wing tip vortices by exploiting and reducing the formed wing tip vortices. This function will now be fulfilled by the wing-tip mounted propeller. Since the goal of this research is to investigate the performance of a wing-tip mounted propeller in a realistic flow field, and not to simulate the Tecnam P2006T, these simplifications are allowed. In table B.1 all properties of the (custom) wing design used throughout this study are listed.

Baseline wing geometry and domain used in CFD

In figure B.1 the domain as used in ANSYS is shown.

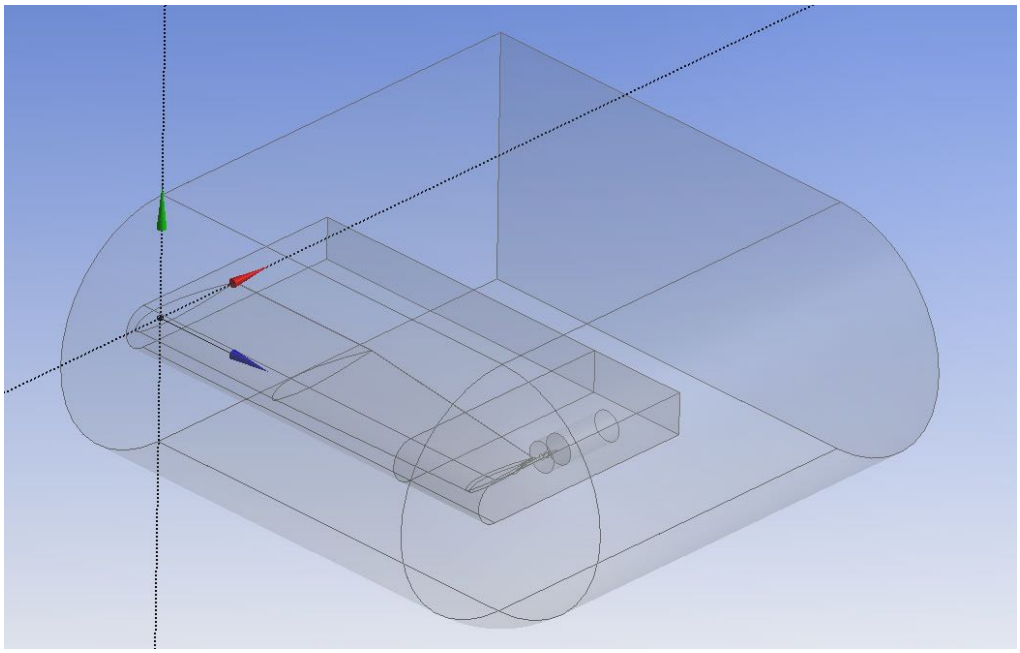

Figure B.1: A schematic overview of the middle domain - containing the wing, propeller and refined inner domain.

Table B.1: Properties of the baseline aircraft wing and spinner, based on the Tecnam P2006T [60]

	Symbol	**Value**	**Unit**
Wing geometry			
Root chord	c_r	2.06	m
Tip chord	c_t	1.383	m
Wing semi-span (w/o winglets)	$b/2$	6.775	m
Kink spanwise position	-	0.4157	m
Taper ratio (inboard)	λ_{ib}	0.00	[-]
Taper ratio (outboard)	λ_{ob}	0.67	[-]
Quarter chord sweep	$\Lambda_{0.25c}$	0.00	deg
Dihedral	Γ	0.00	deg
Root airfoil	-	NACA 23015	-
Kink airfoil	-	NACA 23015	-
Tip airfoil	-	NACA 23012	-
Wing tip shape	-	rounded	[-]
Spinner geometry			
Spinner radius	$r_{spinner}$	0.05	m
Propeller centreline (spanwise)	-	6.775	m/s
Length (aft of TE)	$l_{spinner}$	0.567	m
Propeller rotational plane (aft of wing trailing edge)	PCA_{plane}	0.262	m
Performance			
Cruise speed	V_{cr}	80	m/s
Cruise angle of attack	α_{cr}	3	deg

Bibliography

[1] Nash N Ahmad, Fred H Proctor, and R Brad Perry. Numerical Simulation of the Aircraft Wake Vortex Flowfield. pages 1–10, 2009.

[2] F. Albano and F. De Gregorio. Trailing vortex detection and quantitative evaluation of vortex characteristics by piv technique. *20th International Congress on Instrumentation in Aerospace Simulation Facilities*, 2003.

[3] E A Anderson, C T Wright, and T A Lawton. Experimental Study of the Structure of the Wingtip Vortex 38th Aerospace Sciences Meeting & Exhibit. (c), 2000. doi: 10.2514/6.2000-269.

[4] John D. Anderson. *Introduction to Flight*. McGraw-Hill Education, 7th edition, 2011. ISBN 0073380245.

[5] Nando Van Arnhem. Design and Analysis of an Installed Pusher Propeller with Boundary Layer Inflow.

[6] Christian Bak, Jeppe Johansen, and Peter B Andersen. Three-Dimensional Corrections of Airfoil Characteristics Based on Pressure Distributions. pages 1–10, 2006.

[7] Andre Bakker. Turbulence Models in Computational Fluid Dynamics - Lecture 10, 2010.

[8] A Betz. Airscrews with minimum energy loss. 1919.

[9] D Birch and T Lee. Structure and Induced Drag of a Tip Vortex. 41(5), 2004.

[10] D Birch and T Lee. Tip Vortex Behind a Wing Oscillated with Small Amplitude. *Journal of Aircraft*, 42(5), 2005.

[11] N A Chigier and V R Corsiglia. Tip Vortices Velocity Distribution. Technical report, NASA Ames Research Center, Moffet Field, California, 1971.

[12] J. Chow. A Computational Study of Wingtip Vortex Flowfield. In *AIAA 24th Fluid Dynamics Conference*, Orlando, Florida, 1993.

[13] Jim S Chow, Defense Analyses, and Peter Bradshaw. Mean and Turbulence Measurements in the Near Field of a Wingtip Vortex. 35(10):1561–1567, 1997.

[14] Matthew J Churchfield and Gregory A Blaisdell. Reynolds Stress Relaxation Turbulence Modeling Applied to a Wingtip Vortex Flow. 51(11), 2013. doi: 10.2514/1.J052265.

[15] Jennifer S Dacles-mariani and Gregory Zilliac. Accuracy assessment of a wingtip vortex flowfield in the near-field region. *AIAA 34t Aerospace Sciences Meeting and Exhibit*, (January), 1996.

[16] By James B Delano and John L Crigler. Compressible-Flow Solutions for the Actuator Disk. Technical report, NACA, Langley, 1953.

[17] By William J Devenport and Michael C Rife. The structure and development of a wing-tip vortex. 2016.

[18] Mark Drela. Xrotor user guide. 2003. URL `http://web.mit.edu/drela/Public/web/xrotor/xrotor_doc.txt`.

[19] Karthikeyan Duraisamy. *Studies in Tip Vortex Formation, Evolution and Control*. PhD thesis, 2005.

[20] Luis Eca and Martin Hoekstra. Discretization uncertainty estimation based on a least squares version of the grid convergence index. (January 2006), 2006.

[21] M. S. Francis. An experimental investigation of wing trailing vortex formation. 1976.

[22] S Ginter. *Naval Fighters 21 - Chance Vought V-173 and XF5U-1 Flying Pancakes*. 1992. ISBN 0-942612-21-3.

[23] Michea Giuni. *Formation and early development of wingtip vortices*. PhD thesis, 2013.

[24] S. Goldstein. On the vortex theory of screwpropellers. 1929.

[25] T.L. Grow. The effect of a wing on its tip vortex. *Journal of Aircraft*, (6):37–41, 1969.

[26] O Gur and A Rosen. Comparison between blade-element models of propellers. *The Aeronautical Journal*, 112(1138):689–704, 2008. doi: 10.13140/RG.2.1.3854.5129.

[27] Boone Guyton and Paule Marcus. The ups and downs of the flying pancake. 1951.

[28] J. Bosschers Herman Snel, R. Houwink. Sectional prediction of lift coefficients on rotating wing turbine blades in stall (ECN 93-052). 1994.

[29] ANSYS Inc. ANSYS Fluent Support Manual. 2016.

[30] ANSYS Inc. ANSYS Meshing Support Manual. 2016.

[31] J. L. Van Ingen. Historical review of work at TU Delft. *38th Fluid Dynamics Conference and Exhibit*, (June):1–49, 2008. doi: AIAA2008-3830.

[32] J Mark Janus, Animesh Chatterjee, and Chris Cavef. Computational Analysis of a Wingtip-Mounted Pusher TVirboprop. 33(2):441–444, 1995.

[33] C Karakus, H Akilli, and B Sahin. Formation , structure , and development of near-field wing tip vortices. 222:13–22, 2007. doi: 10.1243/09544100JAERO274.

[34] Sung-eun Kim and SH Rhee. Prediction of tip-vortex flow past a finite wing. *AIAA Paper*, (January):1–10, 2005. doi: 10.2514/6.2005-58.

[35] Sung-eun Kim and Shin Hyung Rhee. Efficient Engineering Prediction of Turbulent Wing Tip Vortex Flows. 62(3):291–309, 2010.

[36] B. M. Kulfan. Universal Parametric Geometry Representation Method. *Journal of Aircraft*, 45(1):142–158, 2008. ISSN 0021-8669. doi: 10.2514/1.29958. URL `http://arc.aiaa.org/doi/10.2514/1.29958`.

[37] E.E Larrabee. Minimum induced loss windmills and propellers. 1983.

[38] Jean-eloi W Lombard, David Moxey, Julien F A Hoessler, Sridar Dhandapani, Mark J Taylor, and Spencer J Sherwin. Implicit large eddy simulation of a wingtip vortex. pages 1–22, 2015.

[39] John L. Loth and Frank Loth. Induced Drag reduction with wing tip mounted propellors. *AIAA 2nd Applied Aerodynamics Conference*, 1984.

[40] B.W. McCormick. Aerodynamics of V/STOL Flight. 1967.

[41] F. R. Menter. Two-equation eddy-viscosity turbulence models for engineering applications. *AIAA Journal*, 32(8):1598–1605, 1994. doi: 10.2514/3.12149.

[42] L R Miranda and J E Brennan. Aerodynamic effects of wing-tip mounted propellers and turbines. *American Institute of Aeronautics and Astronautics*, 86-1802:221–228, 1986. doi: DOI:10.2514/6.1986-1802.

[43] F. Moens and P. Gardarein. Numerical simulation of the propeller/wing interaction for transport aircraft. *AIAA Paper 2001-2404*, 2001. doi: 10.2514/6.2001-2404.

[44] James C. Patterson and Glynn R Bartlett. Evaluation of installed performance of a wing-tip-mounted pusher turboprop on a semispan wing. *NASA Technical paper*, (August), 1987. ISSN 01488341.

[45] J.C. Patterson. Lift Induced Wing-tip Vortex Attenuation. In *AIAA 12th Aerospace Sciences Meeting*, 1974. doi: 10.2514/6.1974-38.

[46] J.C. Patterson. United States Patent: Wingtip Vortex Turbine. 1990.

[47] J.C. Patterson and Glynn R Bartlett. Effect of a wing-tip mounted pusher turboprop on the aerodynamic characteristics of a semi-span wing. In *AIAA 84*, Monterey, California, 1985.

[48] Michael D Patterson and Matthew J Daskilewicz. Conceptual Design of Electric Aircraft with Distributed Propellers : Multidisciplinary Analysis Needs and Aerodynamic Modeling Development. (January):1–18, 2014. doi: 10.2514/6.2014-0534.

[49] Micheál S O Regan, Philip C Griffin, Gary Mcnicholas, and Trevor M Young. Experimental / Numerical Investigation of a Wingtip Vortex. (June):1–8, 2012. doi: 10.2514/6.2012-3331.

[50] P J Roache. Perspective : A Method for Uniform Reporting of Grid Refinement Studies. *Journal of Fluids Engineering*, 116(September 1994):405–413, 1994.

[51] G.J.J Ruijgrok. *Elements of airplane performance*. VSSD, 2009. ISBN 9065622322.

[52] Christopher L Rumsey and Philippe R Spalart. Turbulence Model Behavior in Low Reynolds Number Regions of Aerodynamic Flowfields. 47(4), 2009. doi: 10.2514/1.39947.

[53] Thomas Sinnige. The Effects of Pylon Blowing on Pusher Propeller Performance and Noise Emissions. 2013.

[54] Melvin H Snyder. Effects of a wingtip mounted propeller on wing lift, induced drag and shed vortex pattern. *Aeronautical Report 68-5*, 1986.

[55] J N Sørensen, W Z Shen, and Munduate. Analysis of Wake States by a Full-field Actuator Disc Model. 88: 73–88, 1998.

[56] Philippe R Spalart and Christopher L Rumsey. Effective Inflow Conditions for Turbulence Models in Aerodynamic Calculations. 45(10), 2007. doi: 10.2514/1.29373.

[57] Tom C. Stokkermans, Nando v. Arnhem, Tomas Sinnige, and Leo L. Veldhuis. Validation and Comparison of RANS Propeller Modeling Methods for Tip-Mounted Applications. *2018 AIAA Aerospace Sciences Meeting*, (January), 2018. doi: 10.2514/6.2018-0542. URL `https://arc.aiaa.org/doi/10.2514/6.2018-0542`.

[58] Alex M. Stoll, Joeben Bevirt, Mark D. Moore, William J. Fredericks, and Nicholas K. Borer. Drag Reduction Through Distributed Electric Propulsion. *14th AIAA Aviation Technology, Integration, and Operations Conference*, (June):1–10, 2014. doi: 10.2514/6.2014-2851. URL `http://arc.aiaa.org/doi/10.2514/6.2014-2851`.

[59] W Sutherland. The viscosity of gases and molecular force. *Philosophical Magazine, S.*, (5):507–531, 1893.

[60] Tecnam. Tecnam p2012. URL `http://www.tecnam.com/aircraft/p2012-traveller/`.

[61] Theodore Theodorsen. *Theory Of Propellers*. PhD thesis, 1948.

[62] D.H. Thompson. A Flow Visualisation Study of Tip Vortex Formation. Technical report, Department of Defence - Melbourne, Victoria, 1983.

[63] Ali Uzun and M Yousuff Hussaini. Simulations of Vortex Formation Around a Blunt Wing Tip. 48(6), 2010. doi: 10.2514/1.J050147.

[64] Henri Werle. *On the Flow of Fluids Made Visible*. 1975.

[65] G.J.D. Zondervan. *A Review of Propeller Modelling Techniques Based on Euler Methods*. Delft University Press, Delft, 1998.